UNIVERSITY OF CALIFORNIA
RIVERSIDE

Probing the Immunogenicity of and Functionalizing Erythrocyte-Derived Optical Particles

A Dissertation submitted in partial satisfaction
of the requirements for the degree of

Doctor of Philosophy

in

Bioengineering

by

Taylor Marie Hanley

March 2021

Dissertation Committee:
Dr. Bahman Anvari, Chairperson
Dr. Maurizio Pellecchia
Dr. Sihem Cheloufi

The Dissertation of Taylor Marie Hanley is approved:

_____

_____

_____

Committee Chairperson

University of California, Riverside

Acknowledgements

I would like to thank my partner Joe. I would not have been able to make it this far without your unlimited patience, support, and kindness.

To my parents, thank you for all your help and for always being there for me.

I am grateful for all the previous Anvari Lab members including Raviraj Vankayala, Joshua Burns, Jenny Mac, and Jack Tang, as well as the current lab members, Thompson Lu and Chi Hua Lee, for all of their assistance with experiments and their insightful discussions. I would also like to acknowledge members of the Pellecchia lab including Ahmed Farouk Salem, Luca Gambini, Carlo Baggio, and Parima Udompholkul for all of their help with our collaborations.

I would like to thank my committee members, Dr. Maurizio Pellecchia and Dr. Sihem Cheloufi, for their collaborations and teachings throughout my time at UCR.

I would like to thank Hong Xu, Leslie Karpinski, Mary Hamer, Dr. David Carter, Kellie McDonald, and my graduate advisors Dr. Hyle Park and Dr. Joshua Morgan for all of their help over the years.

I am thankful to my co-authors, Dr. David Lo and Dr. Wenbin Tan, for their lessons in experimental design.

Lastly, I would like to thank my advisor, Dr. Bahman Anvari. Thank you for all of your guidance.

The text of this dissertation, in part or in full, has been previously published in the Journal of Biomedical Optics 2019 and Molecular Pharmaceutics 2020.

This work was supported in part by grants from the National Science Foundation (CBET-1509218 to Bahman Anvari), and the National Institute of Arthritis and Musculoskeletal and Skin Diseases (R01-AR068067 to Bahman Anvari and R01-AR073172 to Wenbin Tan). The model of CD47 in Figures 1, 2, 14, and 15 were based off the DNA sequence from protein data base entry 2JJS and were modeled using the Chimera program from the University of California, San Diego.

ABSTRACT OF THE DISSERTATION

Probing the Immunogenicity of and Functionalizing Erythrocyte-Derived Optical Particles

by

Taylor Marie Hanley

Doctor of Philosophy, Graduate Program in Bioengineering
University of California, Riverside, March 2021
Dr. Bahman Anvari, Chairperson

There has been a recent increase in the design of delivery vehicles fabricated from cell membranes in order to equip systems with immune evasion capabilities. The membranes of erythrocytes have been used to camouflage various cargos to reduce their immune system uptake. We have developed erythrocyte-derived optical particles loaded with the FDA-approved near-infrared (NIR) dye, indocyanine green (ICG). We refer to these constructs as **N**IR **e**rythrocyte-derived **t**ransducers (NETs). These NETs can be excited by NIR light, resulting in the generation of heat, fluorescence, and reactive oxygen species (ROS).

We review the current field of light-based erythrocyte-derived particles for imaging and therapeutic applications. Next, we examine the acute innate immune response to micro- and nano-sized NETs (μNETs and nNETs, respectively) by measuring the cytokine production in response to these particles at different doses, and at different times post-injection. We look at the effect of functionalizing the nNETs with clinically

relevant targeting moieties and the effect of a second injection of μNETs or nNETs one week after the first injection. The results show that up to 6 hours post-injection NETs do not induce the production of inflammatory cytokines to the same extent as a positive control injection of lipopolysaccharides. Functionalizing the nNETs was associated with a decrease in the cytokine response, and in general there were no significant differences between a single injection and dual injections of the μNETs or nNETs. These results show the potential for NETs as non-immunogenic delivery vehicles for ICG.

We also investigate the targeting capacity of nano-sized NETs functionalized with the ligand binding domain of erythropoietin-production human hepatocellular receptor (Eph) B1. We show that these functionalized NETs (F-NETs) are able to target cells that over-express ephrin-B2 ligands. F-NETs can therefore be used to target diseased cell states characterized by the over-expression of ephrin-B2 for phototherapy.

Finally, we demonstrate the successful functionalization of nano-sized NETs with a peptide that binds to EphA2, and is co-loaded with the chemotherapeutic Taxol in addition to ICG. Our results show the particles are able to target breast cancer cells expressing the EphA2 receptor, and facilitate receptor degradation upon binding to the cells.

Table of Contents

List of Figures

List of Tables

Chapter 1: Introduction

The site-specific delivery of therapeutic, diagnostic, and imaging agents is one of the major challenges currently faced by the biomedical community. An emerging delivery platform are constructs derived from various cells, including constructs derived from macrophages, lymphocytes, and stem cells.[1] Constructs derived from red blood cells (RBCs) (erythrocytes) are increasing in popularity, and have recently been the subject of a number of reviews.[2–10] RBC-derived constructs have been fabricated using a number of different payloads, and have been developed for a number of different applications, including increasing the circulation of contrast agents for various types of imaging[11,12] and drug delivery for cancer.[13,14]

Indocyanine green (ICG) is a payload of particular interest. As one of the only near infrared (NIR) dyes approved by the U.S. Food and Drug administration (FDA), ICG has been used approved for use in ophthalmic angiography[15] and monitoring liver function.[16] It has also been clinically investigated for use in sentinel lymph node mapping, tumor detection, tissue perfusion, and the detection of vital structures.[17] However, ICG has a very short half-life on the order of 3-5 minutes in healthy individuals,[16] and is quickly removed from the blood by the liver, usually within 10-20 minutes.[16,18] Given its many clinical uses, ICG is a common payload for cell-derived carriers, and has been loaded into numerous RBC-derived constructs since 2015.[19–28]

We have previously reported the first successful fabrication of nano-sized erythrocyte-derived particles loaded with ICG for the imaging and phototherapy of cancerous tissues.[29] We refer to these constructs as NIR erythrocyte-derived transducers

(NETs) because they are capable of transducing absorbed NIR light to emit fluorescence, generate heat, or facilitate the production of reactive oxygen species.[30] NETs can have their diameter tuned from the micro- to the nano-scale (μNETs and nNETs, respectively) for various applications. For instance, μNETs have potential in the phototherapy of vascular malformations, such as Port Wine Stains (PWSs),[31] while nNETs have possible applications in cancer due to the enhanced permeability and retention effect.[32] We have previously shown that both μNETs and nNETs maintain the presence of CD47,[33] a marker of self on the surface of erythrocytes that inhibits phagocytosis,[34] endowing them with innate immune evasion properties. In addition, we have previously demonstrated that nNETs can be functionalized with various moieties for the specific targeting of cancers that express human epidermal growth receptor (HER2) *in vitro*,[33] and for the thrombolysis of blood clots in *in vitro* models.[35] NETs are therefore a promising and versatile light-based RBC-derived construct that have potential for a number of clinical applications.

Chapter 2 reviews the current field of light-based RBC-derived constructs. We broadly categorize these constructs as either platforms that employ RBC-membranes as a coating, or constructs where the RBCs are instead used as a carrier for a payload. The methods for fabricating both types of constructs, as well as the various optical cargos utilized, are detailed and compared. These constructs are developed for a number of applications, including imaging, phototherapy, and drug delivery. These applications are also reviewed, with a focus on their potential clinical uses. Finally, we highlight the

potential directions of this young field, as well as outline some of the challenges that need to be overcome for clinical translation.

In chapter 3 we investigate the acute innate immune response to μNETs and nNETs. We study the effect of particle dose on the blood serum, liver, and spleen interleukin (IL)-6, IL-10, tumor necrosis factor (TNF)-α, and macrophage chemoattractant protein (MCP)-1 cytokine levels 2 hours post-injection. We see that μNETs induced significantly lower levels of all the cytokines compared to a positive control, and that there was no apparent dose response. For the nNETs there were some instances of a dose response, as well as a few organs that had elevated cytokine levels compared to the negative control. We also look at how those cytokine levels change from 2-6 hours after particle injection. In general cytokines in the blood serum either decreased or did not significantly change. In the liver and spleen the cytokines either do not significantly change, or they increase over time in response to μNETs and decrease over time in response to nNETs. In addition, we analyze the effect of functionalizing the nNETs with folate and Herceptin® on those cytokine levels. Functionalizing the nNETs is associated with a general in reduction for IL-6 and MCP-1 in all of the investigated organs, as well as TNF-α in the blood serum. Finally, we measure the effect of repeated doses of μNETs or nNETs spaced one week apart. Overall, repeated injections of μNETs and nNETs does not result in a significant increase in cytokine levels, with the exception of IL-10 in the spleen in response to the nNETs. These results give us one of the first looks into how light-based RBC-derived particles interact with the innate immune system, which is important to understand for clinical translation.

In chapter 4 we demonstrate the successful functionalization of NETs (F-NETs) with the ligand binding domain of erythropoietin-production human hepatocellular (Eph) receptor B1 (EphB1). We see that while functionalization does result in an increase in the hydrodynamic diameter of the NETs, the absorbance and fluorescence emission characteristics of the constructs are not affected. This functionalization endows the NETs with the ability to target cells that over-express ephrin-B2 ligands, which we investigate *in vitro* with human dermal microvascular endothelial cells (hDMVECs) transfected to overexpress ephrin-B2. Using NIR fluorescent imaging we see that F-NETs are able to efficiently target these hDMVECs, and that as the dose of F-NETs increases the NIR signal from the cells increases until the cells are saturated. These F-NETs represent a promising platform for the imaging and potential NIR phototherapy of a number of diseased cell states associated with an over-expression of ephrin-B2 ligands.

Finally, we fabricate NETs loaded with the chemotherapeutic drug paclitaxel and functionalized with a peptide capable of targeting and subsequently degrading EphA2 receptors. We successfully functionalized the NETs with the targeting peptide, 147B5 (147B5-NETs), and a scrambled sequence version of the peptide (Scrambled-NETs) as a control. We verify the functionalization using emission spectra measurements. We see that after incubation with MDA-MD-231 cells the EphA2 receptors are degraded by 147B5-NETs when the 147B5 concentration is 200 nM. In addition, we see that the 147B5-NETs are more readily uptaken by the cells compared to the Scrambled-NETs. The 147B5-NETs are therefore capable of targeted EphA2 receptor degradation, as well as potential NIR imaging and phototherapy for cells that over-express EphA2 receptors.

Chapter 2: Light-Based Theragnostics Using Erythrocyte-Based Particles

2.1 Abstract

There has been a recent increase in the development of cell membrane-derived drug delivery vehicles. Being the most abundant cell type in the human body, many of these constructs have been fabricated from red blood cells (RBCs). There has been a simultaneous increase in the investigation of light for both imaging and therapeutic applications. Combining RBC-derived constructs with light has led to a new sub-field of drug delivery. These constructs are able to take advantage of the immune evasion properties of the RBC, while the addition of an optical cargo allows the particles to be excited by light for a number of promising applications. Here we review the common fabrication methods employed to engineer these different constructs. We also discuss the current light-based and potential clinical applications these particles are being designed for, as well as offer some insight into the current direction of this exciting sub-field.

2.2 Introduction

Over nearly the past three decades, numerous types of constructs have been developed for the delivery of therapeutic and imaging payloads to target sites of interest. The overarching goals of the engineered delivery systems are to protect the payload from non-specific interactions with biomolecules and other molecular entities in the milieu of physiological environments, and escape or minimize clearance by the immune system so that sufficient amounts of the payload can reach the target site to achieve the desired efficacy without inducing non-specific toxicity and reducing harmful off-target side effects.[36]

A contemporary approach in engineering of delivery systems is based on the use of cells or cell-derived constructs to encapsulate the desired payload, or cell membranes to coat the payload. Examples include delivery systems based on macrophages, lymphocytes, neutrophils, and stems cells.[1,37] A fundamental principle underlying the use of cell-based or cell-derived systems is that the built-in mosaic of the cell membrane can provide the camouflaging machinery to protect the payload from recognition by immune cells and increase the bioavailability of the payload.

Red blood cells (RBCs) (erythrocytes) are a particularly promising delivery system due to the presence of membrane proteins including CD47, which prevents phagocytic uptake by macrophages, as well as complement receptor 1 (CR1) and decay-accelerating factor (DAF) (CD55), which can prevent self-recognition by an alternate complement pathway by inhibiting C3 convertases.[9] The presence of these “self-markers” on RBCs has the potential to increase the circulation of a desired payload embedded

within an RBC-based construct as a result of protecting the payload from recognition and subsequent removal or destruction by the immune cells. One of the earliest examples of RBCs being used as carriers is from 1973 when Ihler et al. demonstrated the successful loading of RBCs with various enzymes.[38] There has been a significant increase in RBC-derived constructs in recent years, especially in the field of nanomedicine, and RBCs have reportedly been used as carriers for not only enzymes, but antibiotics, nanoparticles (NPs), and various drugs as well.[10] More recently, RBC-based payload delivery systems have been extensively reviewed,[2,4,5,7,9,10,39,40] and new sub-fields, such as systems designed for the delivery of cancer therapeutics[14] and vascular imaging,[12] are emerging. A particular use of RBC-derived constructs is in relation to loading of optical cargos such as quantum dots (QDs),[41–43] metallic materials,[44–46] and organic molecules,[29,47,48] in order to use the constructs for optical imaging and sensing, and photo-therapeutic applications. This review specifically covers the development of RBC-derived constructs for light-based theranostics and summarizes some of the current potential clinical applications for these constructs.

2.3 Fabrication of RBC-Derived Constructs

2.3.1 *Substrate Coating by RBC Membranes*

A majority of light-based RBC-derived constructs involve using the RBC membrane as a coating for a cargo in order to endow the cargo with the immune evasion properties of a native RBC. RBC coatings have been used for a number of optical cargos such as various metals and semiconductors. For example, Ren et al. coated iron oxide (Fe_3O_4) magnetic

nanoclusters with RBC membranes for photothermal therapy (PTT) [1]. Gold NPs, such as the gold nanorods fabricated by Li et al. have also been coated with RBC membranes for use in PTT.[50] Semiconducting materials, such as the $MoSe_2$ nanosheets designed by He et al. were similarly coated with RBC membranes, again for PTT.[51] NPs made from organic molecules have also been coated with RBC membranes. For example, Ye et al. made spherical NPs from the chemodrug 10-hydroxycamptothecin (HCPT) and the near infrared (NIR) dye indocyanine green (ICG), which they were able to coat with RBC membranes for combined chemotherapy and PTT.[24] While these are all examples of solid optical cargos, optical cargos can also be hollow or mesoporous for the encapsulation of other cargos, such as chemotherapeutic drugs. For instance, Chen et al. prepared hollow mesoporous Prussian blue (PB) NPs that they were able to load with the chemotherapeutic drug doxorubicin (DOX) before coating the particles with RBC membranes, allowing them to combine PTT and chemotherapy.[52]

Another common optical cargo is upconversion nanoparticles (UCNPs). These NPs are usually made from rare-earth elements and are capable of converting longer wavelengths of light, such as NIR wavelengths, into shorter wavelengths, such as visible or UV light.[53] For example, Ding et al. prepared $NaYF_4$:Yb/Er UCNPs coated with merocyanine 540 (MC540).[54] Here the UCNPs excited by 980 nm laser light resulted in luminescence in the 530-550 nm range, which was able to excite the MC540 for photodynamic therapy (PDT).

It is important to note that all of the examples mentioned thus far have involved coating a NP made from a material capable of interacting with light. However, there are

some instances where NPs themselves are loaded with an optical cargo before being coated with an RBC membrane. For example, Yang et al. fabricated triblock copolymer nanoparticles loaded with the dye IR780 for phototherapy and docetaxel (DTX) for chemotherapy.[55] These particles were then coated with RBC membranes for enhanced circulation. In addition, there are some constructs where the RBC membrane is used to coat a non-optical cargo, and the optical cargo is incorporated into the construct using other methods. For example, Su et al. loaded polymeric NPs with paclitaxel for chemotherapy, and then coated the particles with RBC-membranes that had the cyanine dye 1, 1-dioctadecyl-3, 3, 3, 3-tetramethylindotricabocyanine iodide (DiR) inserted into the lipid bilayer for PTT.[56] Here the optical cargo is not in the core of the construct, but is instead in the membrane coating itself.

All of these examples show that there are a large number of constructs that can be coated with RBC membranes. In order to coat a cargo with the RBC membrane, whole blood is first washed with an isotonic buffer such as phosphate buffered saline (PBS) to isolate the RBCs. The RBCs are treated with a hypotonic buffer to deplete hemoglobin from the RBCs, resulting in erythrocyte ghosts (EGs). The EGs must then be scaled from the micro- to the nano-scale. Common methods for size reduction are mechanical extrusion, sonication, or a combination of the two. During mechanical extrusion, EGs are pushed through membranes with pores of a predetermined size, usually on the order of 200-800 nm. This leads to membrane lysis and reformation into smaller vesicles.[57] Sonication, or the application of sound waves with varying frequencies, is another cell disruption method.[58] Sonicating EGs also results in membrane rupture, and the

subsequent reformation of nano-sized membranes.[59] A schematic outlining the main steps for RBC-membrane coating are shown in Figure 1.

Since both sonication and extrusion result in membrane rupture, they can be used not only to reduce the size of EGs to fabricate nano-EGs (nEGs), but also to facilitate coating of an optical cargo. Mixing nEGs with a NP and repeating the sonication and/or extrusion facilitates the coating of the cargo with the RBC membrane, resulting in a construct with a core-shell morphology where the NP is clearly coated by a membrane layer. In general, transmission electron microscope (TEM) images show that the RBC membrane conforms to the shape of the coated substrate. This has been shown in the work done by Rao et al. where coating hexagonal UCNPs with RBC membranes resulted in a hexagonal construct for cancer imaging.[60] Wang et al. have also developed spherical bovine serum albumin (BSA) nanoconstructs that encapsulate ICG and the chemodrug gambogic acid, and when coated in RBC membranes also result in a spherical nanoconstruct for chemotherapy and PTT.[28] These examples show a uniform membrane coating on a NP core. In addition to confirming the membrane coating using imaging, RBC membrane coatings have been confirmed by SDS-PAGE,[60–63] as well as Western blots demonstrating the presence of CD47 on the final construct.[55,64] Constructs that employ RBC membranes as a substrate coating have also been shown to be fairly stable, with many constructs showing minimal changes in size after storage of up to one week.[65,66]

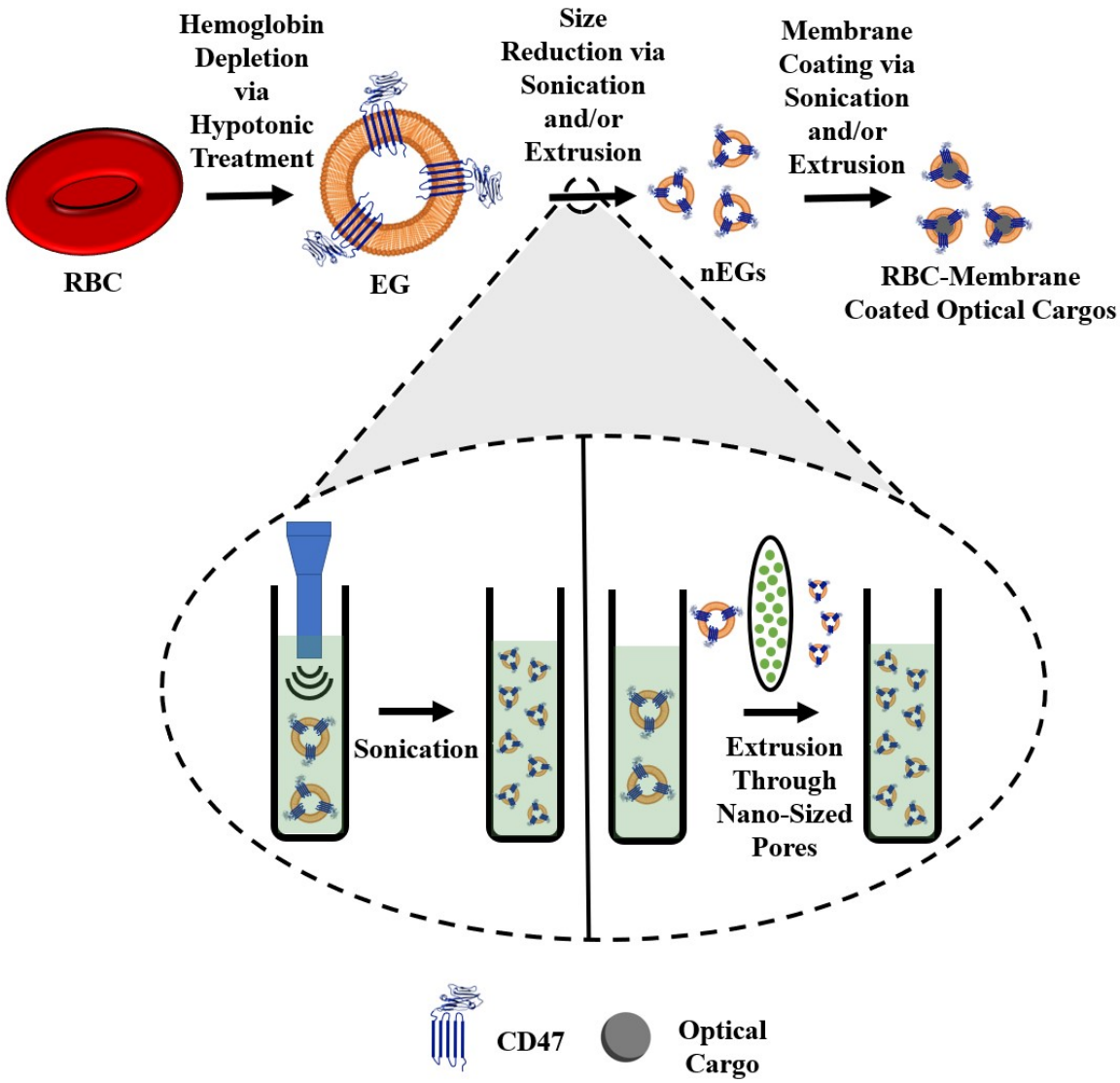

Figure 1. Schematic illustrating RBC-membrane coating. RBCs are depleted of their hemoglobin using a hypotonic treatment to form erythrocyte ghosts (EGs). The EGs then go through a size reduction process using sonication and/or extrusion to form nano-EGs (nEGs). The nEGs are mixed with an optical cargo and the sonication and/or extrusion steps are repeated to facilitate membrane coating. For illustrated purposes CD47 is shown as one of the RBC transmembrane proteins the EGs retain. A representative spherical nanoparticle is shown as the optical cargo. The inset illustrates the sonication and extrusion size reduction methods. During sonication sound waves are applied to EGs, while during extrusion the EGs are pushed through filters with nano-sized pores, both of which result in nEGs.

While most of the previous examples have involved constructs where the RBC membranes coat a single NP, there are exceptions. For instance, Liu et al. encapsulated ICG in anionic BSA nanoclusters which are able to form complexes with the chemotherapeutic 1,2-diaminocyclohexane-platinum (II) (DACHPt).[23] When these nanoclusters were coated with RBC membranes the resulting constructs still showed an outer membrane shell; however, the constructs contained multiple BSA-based nanoclusters inside. In addition, researchers have shown that RBC membrane coatings are not limited to NPs. Gao et al. designed RBC-shaped hemoglobin particles that contain Fe_3O_4 NPs and ICG that are micro-sized, and showed that after coating with RBC membranes the final constructs were still on the micro-scale, and that the membranes had conformed to the RBC-shape of the particles.[67]

2.3.2 *Constructs that Use the RBC as a Carrier*

While most light-based RBC-derived constructs use the RBC membrane as a substrate coating, there are a growing number of constructs that use the RBC as a carrier. Constructs that use the RBC as a carrier can have a variety of optical cargos, including organic molecules[68–70] and NPs made from various metals[44] or semiconductors.[71,72] While constructs that use the RBC membrane as a coating primarily use sonication and/or extrusion to facilitate substrate coating, there are a number of different loading methods for constructs that use the RBC as a carrier. Loading methods can be applied directly to RBCs, as well as EGs and nEGs. However, the vast majority of RBC-derived carriers are

fabricated from RBCs. These methods can be broadly divided into those that load a cargo to the interior of the carrier, and those that load the cargo to the exterior of the construct.

2.3.2.1 *Methods for Interior Loading of an Optical Cargo*

2.3.2.1.1 *Hypotonic Loading*

The most common loading methods for RBC carrier constructs are those that involve hypotonic buffers. When RBCs are placed in a hypotonic buffer they swell, causing the formation of pores for removal of intracellular components, but also allowing the internal loading of the cargo.[68] For example, Wu et al., using a hypotonic treatment, were able to simultaneously load RBCs with DOX, magnetic NPs, and QDs capable of fluorescence emission.[41] We have used a similar method to load EGs with ICG using Sorenson's buffer, resulting in micron-sized light-responsive constructs.[73] We have also applied this method to nEGs, where we first extruded EGs to get nEGs before incubating with Sorenson's buffer and ICG, resulting in the loading of ICG into the nEGs.[73] Therefore, hypotonic loading methods can be applied to RBCs, EGs, and nEGs. RBCs can also be loaded using hypotonic dialysis. Here the RBCs are typically mixed with a cargo in a dialysis bag, which is then exposed to a hypotonic buffer, again leading to the formation of pores through which the cargo can enter the RBCs.[74] Figure 2 shows a schematic illustrating optical cargo loading of RBCs, EGs, and nEGs.

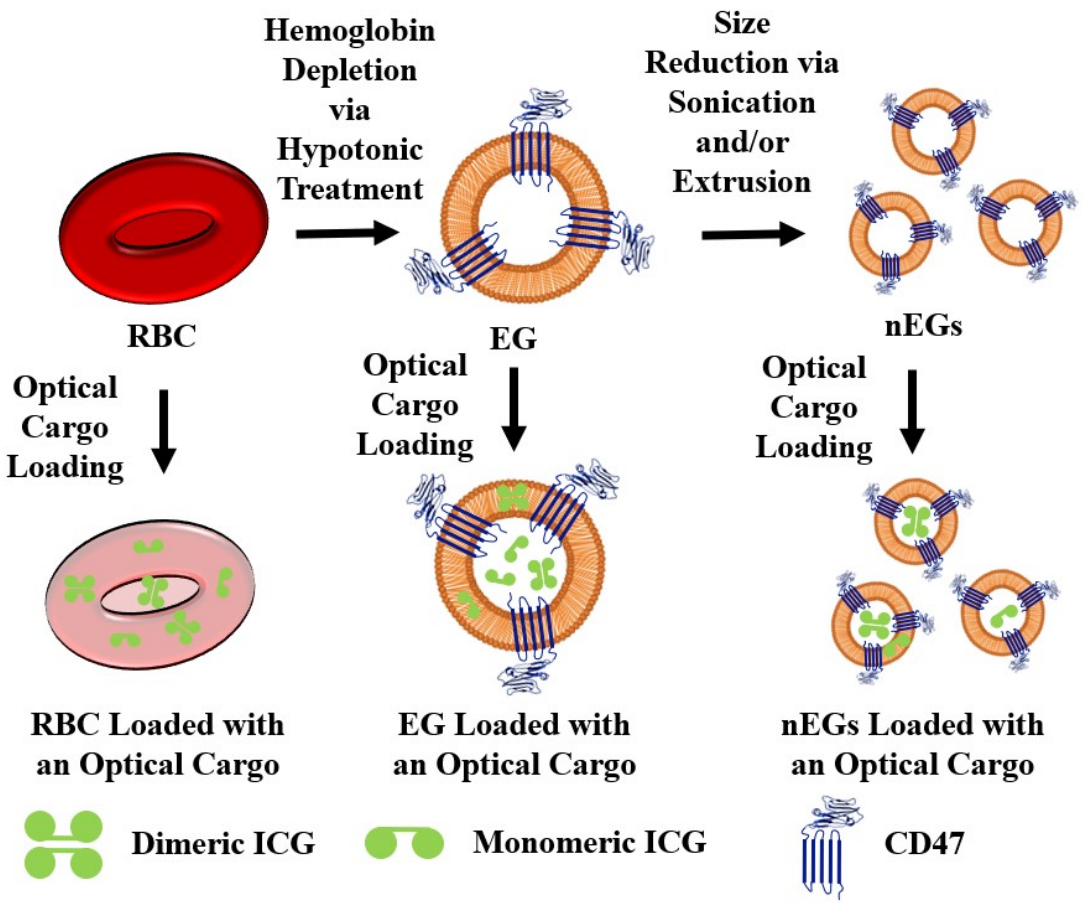

Figure 2. Schematic illustrating RBCs, EGs, and nEGs loaded with an optical cargo to serve as RBC-derived carriers. For illustrated purposes CD47 is shown as one of the RBC transmembrane proteins the EGs retain. As a representative optical cargo, the dye indocyanine green (ICG) is shown in its dimeric and monomeric forms.

It is interesting to note that in some cases loading RBCs with an optical cargo using a hypotonic buffer can preserve the biconcave disk shape and size of native RBCs. For example, Jiang et al. were able to load mouse RBCs with fluorescent silicon NPs hypotonically, resulting in constructs with the biconcave disk morphology ≈ 6 μm in diameter.[71] Here the hypotonic buffer was 0.5xPBS with 2 mM ATP and 3 mM glutathione, and the mixture was incubated for 45 minutes at 4°C. Jiang et al. showed that

after the RBCs were resealed the silicon NPs were clearly visible inside the RBCs.[71] However, hypotonically loading the optical cargo does not always preserve the biconcave morphology of native RBCs, as can be seen by the constructs fabricated by Bustamante López and Meissner.[75] After using a hypotonic lysis buffer to load bovine erythrocytes with fluorescein isothiocyanate (FITC) glycylglycine conjugates, the resulting constructs were significantly smaller and had less hemoglobin compared to native erythrocytes. When analyzed using atomic force microscopy (AFM) the authors also found that the loaded constructs were more rounded and had a rougher surface compared to native erythrocytes. Here the lysis buffer contained $MgCl_2$, EDTA, phosphate buffer, and urea.[75]

As demonstrated by the two previous examples, the buffer choice for hypotonic loading can vary, which may be why hypotonic loading does not always produce constructs that preserve native RBC morphology. A number of different buffers have been used for hypotonic dialysis,[74] but there are no clear trends for hypotonic buffer choice when it comes to loading optical cargos. Another factor potentially affecting the morphology of the construct is the type of blood used. For instance, Jiang et al. used mouse blood for their constructs,[71] while Bustamante López and Meissner used bovine blood.[75] Most constructs are fabricated using mouse blood. This includes the constructs previously mentioned engineered by Marvin et al., which also show that the RBC morphology is preserved after using dialysis to load RBCs using a hypotonic PBS buffer with 6 mM glucose.[76] It is possible that differences between the RBCs, such as membrane composition and size, could have an effect on how the cells react to hypotonic loading methods. It is important to note that for clinical translation the constructs will ultimately

need to be fabricated using human RBCs. It is known that there are a number of structural differences between mouse and human RBCs, such as size and membrane protein composition,[77] so more research is needed to determine if hypotonic loading methods used on human RBCs will still preserve the native RBC morphology. More research is also needed on the effects of using different hypotonic buffers for the loading procedure, as well as the effect of the type of optical cargo being loaded.

Another important factor to consider with hypotonic treatment is the potential for phosphatidylserine (PS) exposure. PS is generally confined to the inner leaflet of erythrocytes,[78] and its exposure leads to macrophage recognition and subsequent clearance of erythrocytes from circulation.[79] Wang et al. have shown that EGs prepared by incubating mouse RBCs in 5 mM NaH_2PO_3/Na_2HPO_3 for 5 minutes at 4 °C have significantly more PS exposure compared to native mouse RBCs.[80] Collaborators Sun et al. showed similar PS exposure results for murine RBC-derived EGs, but showed that RBCs loaded with DOX via hypotonic dialysis did not show elevated PS exposure levels.[81] Again, the choice of hypotonic buffer many play a role in PS exposure during hypotonic treatment. In addition, using a hypotonic buffer for loading may affect the PS exposure differently than using a hypotonic buffer for hemoglobin depletion. For RBC-derived carriers to achieve the similar circulation times as native RBCs the effect of hypotonic loading on PS exposure needs to be more thoroughly understood, particularly for carriers derived from human RBCs.

2.3.2.1.2 *Less Common Methods for Interior Optical Cargo Loading*

Electroporation is a relatively new cargo loading method that involves the application of an electric field to the membranes, which in theory will result in the formation of pores through which materials can cross the membrane.[82] Bustamante Lopéz and Meissner were able to use electroporation to load bovine RBC membranes with a fluorescent dye, resulting in constructs that were 5.32 μm, compared to the 6.2 μm diameter of the native bovine erythrocytes and the 5.0 μm diameter of membranes loaded hypotonically.[75] Compared to loading using a hypotonic buffer, however, RBCs loaded via electroporation had a significantly lower loading efficiency.[75]

Another loading method involves extrusion to load small organic molecules. In this case the RBC membrane does not coat the cargo and is instead used as a nano-sized carrier. For example, we mixed EGs derived from bovine RBCs with ICG-BSA and extruded the solution, resulting in nano-sized constructs capable of being used for cancer cell imaging applications.[83] It is important to note that using extrusion to load organic molecules will result in a nano-sized construct. While these two examples demonstrate that there are potentially RBC interior loading methods that do not use a hypotonic buffer, hypotonic loading mechanisms are significantly more common for loading optical cargos. More research is needed to determine if these alternative loading methods offer a significant advantage over hypotonic loading methods. In addition, both of these examples were conducted with bovine RBCs. Mouse and human RBCs may respond differently to these loading techniques, indicating another area for further research.

2.3.2.1.3 *Optical Cargo Embedding in the Lipid Bilayer*

Some organic molecules are capable of directly interacting with RBC membranes, allowing them to be embedded into the lipid membrane of the RBC. For example, chlorin e6 (Ce6) is a lipophilic molecule capable of interacting with lipid membranes.[84] Both Gao et al. and Sun et al. have demonstrated that Ce6 can be embedded in RBC membranes by mixing.[70,85] Sun et al. used the Ce6-embedded RBC membrane as a coating for PB NPs,[85] suggesting that embedding optical cargos can be combined with using RBC-membranes as a substrate coating. Gao et al. demonstrated that they were able to combine the hypotonic dialysis loading of DOX into RBCs with Ce6 embedding in the RBC lipid bilayer.[70] In addition, Gao et al. were able to show that while DOX was loaded to the interior of the RBCs, Ce6 was localized to the membrane of the RBCs. Not only do these two studies demonstrate that optical cargos have the potential to be loaded into RBCs through simple mixing, but they also demonstrate that multiple loading methods can be used to fabricate a single construct. Another lipophilic dye, DiR, has been used for cell membrane labeling,[86] and is another potential optical cargo that can be directly embedded in RBC-membranes. Su et al. have demonstrated that DiR is capable of being embedded into the lipid membranes of nEGs, which are then used to coat paclitaxel-load polymeric NPs.[56] While this example of an optical cargo being embedded in the lipid bilayer was also ultimately used for substrate coating, it also suggests that lipophilic dyes can be embedded into the lipid membranes of EGs and nEGs, and not just RBCs. However, organic molecules are the only optical cargos that have been embedded into the lipid

bilayer of RBC-derived constructs, so this loading method may have limited applications for other optical cargos, such as metallic NPs.

2.3.2.2 *Methods for Exterior Loading of an Optical Cargo*

While RBC-derived constructs employed as carriers usually involve loading an optical cargo to the interior, or in some cases into the lipid membrane bilayer of the construct, there are some examples of the optical cargo being incorporated onto the surface. For example, some optical cargos are able to adsorb directly to the surface of RBCs. Delcea et al. were able to incorporate gold NPs into their constructs using adsorption, and they suggest that the adsorption is possible due to interactions between the positively charged NPs and the negatively charged glycocalyx on the RBC membrane.[44]

It has also been suggested that organic molecules are capable of adsorbing to RBCs; however, the results have not been as promising. Sun et al. report that they were able to adsorb ICG to the surface of RBCs, but that the ICG was easily washed away in serum-supplemented media.[81] Flower and Kling similarly showed that while ICG is capable of adsorbing to RBCs, the amount of ICG that could be loaded was almost half the amount that could be loaded into RBCs hypotonically.[87] While there is potential for optical cargos to adsorb directly to RBCs, more research needs to be done to determine the types of optical cargos it is appropriate for, as well as determining how the adsorption is accomplished for those appropriate optical cargos.

Another emerging method for attaching an optical cargo to the surface of RBC-derived constructs is functionalization. Here a lipid linker is used to attach the optical

cargo to the surface of the construct. A common lipid linker is 1,2-distearoly-sn-glycero-3-phophoethanolamine-N-[χ(polyethylene glycol)] (DSPE-PEG-χ) where χ can be a number of functional groups. DSPE is able to insert itself into the lipid bilayer of the RBC membranes, similar to the lipid-insertion methods outlined by Fang et al.,[88] resulting in the desired molecule being attached to the surface of the RBC membrane. Wang et al. incubated RBCs with DSPE-PEG-biotin, which enabled them to attach various avidin-functionalized UCNPs to the RBCs.[25,89] This method takes advantage of the strong and highly specific interaction between biotin and avidin,[90] resulting in constructs that preserve the biconcave morphology of native RBCs.[25,89] Other groups have used other lipid linkers to biotinylate RBCs. For example, Tang et al. used biotin-X-NHS, which was able to attach to neutravidin, which was in turn able to bind to their biotinylated ferritin nano-capsules loaded with the optical cargo $ZnF_{16}Pc$.[91] Wang et al. used sulfo-NHS-LC-biotin to biotinylate RBCs, which could then bind to Ce6-coated iron oxide NPs that were conjugated to avidin.[80] While there are only a few examples of functionalizing RBCs with an optical cargo, there are a number of groups looking at functionalizing RBC-derived constructs with other moieties for active targeting, as will be discussed below.

2.4 Potential Clinical Applications

2.4.1 *Imaging Applications*

2.4.1.1 *Fluorescence Imaging*

RBC-derived constructs have been developed for a number of light-based applications; however, all of the applications require an optical cargo of some sort. How the optical cargo interacts with light will determine which light-based applications the RBC-derived construct is suitable for. If light excitation results in the optical cargo generating fluorescence emission, it can be used for various imaging applications. For example, Guo et al. developed constructs made from hydrophobic QDs coated in membrane lipids extracted from RBCs.[42] The constructs are able to fuse with the cell membrane, allowing the QDs to be embedded in the membrane for imaging applications as well as tracking cell movement.

In addition to tracking cell movement using fluorescence imaging, RBC-derived constructs can be designed for cancer imaging. For example, Li et al. prepared NPs from gold nanoclusters and pea protein isolate that were coated with RBC-membranes, resulting in nano-constructs suitable for NIR fluorescence imaging *in vivo.*[92] The RBC-membrane coating resulted in increased tumor accumulation of the NPs compared to bare NPs. Another imaging construct developed for cancer imaging is one we have developed which involves loading nEGs with ICG-BSA for imaging tumor cells.[83] We found that SKOV3 ovarian cancer cells had a higher uptake efficiency of these constructs compared to free ICG-BSA.

ICG has also been used in constructs developed for vascular fluorescence imaging. In 2008 Flower et al. developed the first light-based RBC-derived construct when they hypotonically loaded RBCs with ICG. These constructs can be used to monitor blood flow in the retinal capillaries and choriocapillaris[68] and characterizing microvascular vasomotion in the human eye and skin.[87] These constructs are fairly simple since they do not involve sonication/extrusion, and they only incorporate one optical cargo. They can therefore be prepared in about 70 minutes under sterile conditions,[87] which has allowed for them to be used in one of the only human studies involving light-based RBC-derived constructs. The only other human study to date, conducted by Wang et al., focused on combining the constructs developed by Flower et al. with a Monte Carlo method in order to automate the velocity estimation of erythrocytes in retinal arterioles and venules in humans.[93]

In addition to vasculature imaging, optical cargos that are organic molecules combined with RBC-based platforms can also be used for blood analyte sensing. Milanick, Ritter, and Meissner have developed constructs they refer to as erythrosensors for the *in vivo* monitoring of blood plasma parameters.[47,69] These constructs are loaded with glycylglycine conjugated to FITC, a pH sensitive dye. They found that the erythrosensors were able to respond to changes in extracellular pH as shown by changes in the measured fluorescence intensity of the constructs.[69] Theoretically, these erythrosensors could circulate throughout the body over time and monitor the blood pH of a patient any time the particles are exposed to an excitation light source. While this is not a direct imaging application, they also show that the resulting constructs are still

visible in epifluorescence micrographs, and they rely on fluorescence emission for their application. In theory, other dyes that are sensitive to specific blood analyte levels, such as glucose levels, could also be loaded into RBCs and used as blood analyte sensors over time.[69]

2.4.1.2 *Upconversion Luminescence Imaging*

If an optical cargo is able to take low energy photons and convert them into higher energy photons it can be used for upconversion luminescence imaging (UCL).[53,94] UCNPs are a promising optical cargo due to their low photobleaching and the potential for low autofluorescence of biological samples.[94] Multiple groups have investigated combining UCNPs with RBC-based delivery constructs, particularly for cancer imaging. For example, Li et al. prepared $NaGdF_4$:Yb, Tm UCNPs that were then coated with RBC-membranes.[65] The resulting constructs showed increased tumor uptake compared to bare UCNPS, and could be used for UCL, as well as magnetic resonance imaging (MRI) and positron emission tomography (PET) imaging.[65] Similarly, Rao et al. prepared β-$NaYF_4$:Er^{3+}, Yb^{3+} UCNPs coated with RBC-membranes and saw increased tumor uptake of the resulting constructs compared to bare UCNPs.[60] These examples show that combining UCNPs with RBC-based constructs have strong potential for use in cancer imaging and detection. When combined with other treatment modalities, as will be discussed below, UCNPs represent a promising new optical cargo.

2.4.2 *Phototherapy*

2.4.2.1 *Photothermal Therapy*

When light absorption of an optical cargo results in a temperature increase, the optical cargo can be used for PTT. Heat generated during PTT can damage and/or destroy the surrounding cells and has potential applications in the treatment of thrombi,[95] Port Wine Stains (PWSs),[31] and cancers.[96] For example, Li et al. developed gold nanorods coated in RBC-membranes that are capable of extremely efficient PTT of human lung carcinoma cells *in vitro* after 808 nm laser irradiation.[97] Piao et al. also used a gold-based optical cargo when they prepared gold nanocages and coated them with RBC-membranes.[98] These constructs were also capable of PTT *in vitro*, but also demonstrated strong tumor PTT *in vivo*.

Magnetic materials, especially those made from iron oxide, are another promising PTT agent[99] commonly used in RBC-derived constructs. It is important to note that since iron oxide NPs are approved for use as MRI contrast agents in humans,[99] many of these constructs are developed for PTT in combination with MRI. For instance, Rao et al. coated Fe_3O_4 magnetic NPs with RBC-membranes and demonstrated their efficient MRI and PTT capabilities for tumors *in vivo*.[100] Similarly, Ren et al. prepared their own Fe_3O_4 magnetic nanoclusters coated with RBC-membranes and found that their constructs demonstrated excellent tumor PTT *in vivo*.[49]

While light-based RBC-derived constructs designed for PTT are mostly being investigated for cancer applications, there are other potential uses that are starting to be explored. We recently developed a model to investigate the treatment of PWSs using EGs

and nEGs loaded with ICG for PTT of the affected blood vessels.[31] The model demonstrated that these RBC-derived constructs in combination with 755 nm laser irradiation had higher PTT efficiency compared to just 585 nm laser irradiation,[31] which is currently one of the more common PWS laser treatment wavelengths.[101]

The potential applications for light-based RBC-derived constructs that use PTT as a therapeutic mechanism increase when multiple light-based mechanisms are combined, as will be discussed below.

2.4.2.2 *Photodynamic Therapy*

Optical cargos can be used for PDT when its light absorption generates reactive oxygen species (ROS) in the presence of adequate oxygen levels.[96] Common PDT agents include tetrapyrrole organic molecules, such as Ce6, synthetic dyes such as methylene blue (MB) and Rose bengal (RB), as well as various NPs including QDs and UCNPs.[102] A vast majority of light-based RBC-derived constructs fabricated for PDT are developed for cancer applications, which has its own specific challenges researchers must address when designing their constructs. For instance, many cancers result in hypoxic tumors.[103] Since one of the main mechanisms of PDT is dependent on converting O_2 into ROS, the lack of oxygen in tumors is a major hurdle to effective PDT.[104] In order to enhance PDT for cancer treatment, a number of groups have investigated incorporating oxygen delivery in addition to optical cargos in RBC-derived platforms. Two common methods are to use hemoglobin or perfluorocarbons (PFC) as oxygen carriers.[104] For example, Liu et al. loaded RBC membranes with complexes made from hemoglobin as an oxygen carrier,

polydopamine to protect the hemoglobin from oxidation, and MB as an optical cargo.[105] Here laser irradiation at 660 nm excites the MB, which has shown great promise as a PDT agent,[106] while the hemoglobin and polydopamine ensure there are adequate oxygen levels at the treatment site.[105] Another example is the construct fabricated by Tang et al., where RBCs are functionalized with ferritin nanocages loaded with the photosensitizer $ZnF_{16}Pc$.[91] The photosensitizer is excited by 671 nm laser irradiation and then the hemoglobin inside the RBCs provides an oxygen source. These constructs demonstrated efficient PDT in an *in vivo* hypoxic tumor model.[91]

In addition to usually being hypoxic, many tumors produce large amounts of hydrogen peroxide (H_2O_2), which may play a role in tumor metastasis and cell proliferation.[107,108] In normal cells, catalase is present to decompose H_2O_2 into O_2 and water, but many cancer cells also appear to have a catalase deficiency.[108,109] RBCs naturally contain catalase, and Du et al. have already shown that RBC-derived particles can be developed for catalase delivery in conjunction with a sonosensitizer to enhance sonodynamic therapy in a hypoxic environment.[110] Therefore, there is potential for combining catalase and an optical cargo in an RBC-derived platform for enhanced PDT in a hypoxic tumor environment. However, researchers have also been able to design optical cargos that take advantage of the high H_2O_2 levels in tumors. Zhao et al. designed a metal-organic framework (MOF) consisting of FeTCPP/Fe_2O_3 that is capable of decomposing H_2O_2 and promoting the formation of singlet oxygen as well as hydroxyl radicals.[111] When these MOFs are coated with RBC-membranes they exhibit strong *in vivo* PDT after 660 nm laser irradiation. This example demonstrates that by carefully

designing the optical cargo, RBC-based constructs can overcome the unique challenges presented by the tumor environment.

2.4.2.3 *Combined Phototherapies*

In order to increase therapeutic efficacy, many researchers have tried to design RBC-based constructs that are capable of both PTT and PDT, particularly for cancer applications. One method to enable both PTT and PDT capabilities to use multiple optical cargos. For example, Sun et al. embedded Ce6 in RBC-membranes which were used to coat PB NPs.[85] Laser irradiation at 660 nm resulted in Ce6-mediated PDT as well as membrane rupture, while laser irradiation at 808 nm led to PTT from the PB NPs. *In vivo* results show these constructs, in conjunction with dual laser irradiation, have excellent tumor growth inhibition abilities.[85] Another example is the construct designed by Li and Zhang where gold nanorods and TiO_2 NPs are co-coated in RBC-membranes.[112] In combination with both UV and NIR light irradiation, the constructs are able to be used for PTT as well as PDT, and have shown promising results for cancer cell destruction *in vitro*.

While incorporating multiple optical cargos does allow for these constructs to be used for both PTT and PDT, it is important to note that many optical cargos are capable of being used for more than one therapeutic effect. For example, Liu et al. have shown that $Cu_{2-x}Se$ NPs coated with RBC-membranes can be used for both PDT and PTT in the treatment of tumors after laser irradiation at 1064 nm.[46]

By carefully selecting the optical cargo used, researchers can achieve multifunctionality of RBC-derived constructs without the need for multiple optical cargos, and limit the need for more than one laser. Simplifying the designed platforms in this way may ease the process for clinical translation, while still allowing for PTT and PDT to potentially be performed simultaneously.

2.4.3 *Drug Delivery*

While a majority of light-based RBC-derived constructs are designed for imaging and phototherapy applications, there is a small subset of constructs that are being designed specifically for light-based drug delivery. Hughes et al. conjugated various bioactives including colchicine, paclitaxel, and methotrexate, to cobalamin.[113] These compounds were hypotonically loaded into RBCs, and after being illuminated at 525 nm the Co-C bond between the bioactive and the cobalamin was cleaved, resulting in the drug being released from the interior of the erythrocytes. Hughes et al. also demonstrated that the wavelength the bond between the bioactives and cobalamin was cleaved at could be tuned by conjugating fluorophores, such as Cy5, to the compounds.[113] This finding suggests that the compounds could be tailored for different light sources; however, most light-based RBC-derived constructs that are engineered for drug delivery are also designed for other applications that will be discussed below.

2.4.4 *Combining Applications*

2.4.4.1 *Imaging and Phototherapy*

While there are a number of light-based RBC-derived constructs that are formulated to be used for only one application (i.e., imaging, drug delivery, or phototherapy), it is far more common for these constructs to be designed for multiple applications. One of the more common application combinations is imaging and phototherapy. Similar to how multiple optical cargos can be incorporated into a construct in order to allow the final product to be used for both PTT and PDT, using multiple optical cargos can also achieve multifunctionality with imaging and phototherapy. For example, Wang et al. have developed RBC-derived theranostic probes that involve ICG-BSA, RB, and UCNPs.[25] The ICG-BSA is hypotonically loaded into RBCs and is excited by 808 nm laser irradiation for imaging and heat generation that causes the release of oxygen from the RBCs. The UCNPs are then excited by 980 nm laser irradiation resulting in 550 nm light that excites the RB for PDT using the released oxygen as a source for generating ROS.

Again, it is important to note that many optical cargos are capable of being used for more than one therapeutic effect. For instance, we have shown that NPs fabricated from nEGs hypotonically loaded with just ICG were able to be used for imaging as well as PTT and PDT for tumor treatment.[30] These constructs are capable of generating ROS *in vitro.* After treatment *in vivo,* extracted tumors showed higher levels of photo-induced activation of Capase-3,[30] which has been linked to PDT-induced apoptosis.[114–117] It is interesting to note that in this case the PDT was performed in a hypoxic environment without extra catalase or oxygen delivery. This could be due to the combined effects of

PTT with PDT. There have been recent investigations towards using PTT to increase tumor blood flow and O_2 levels, both of which would increase the efficacy of PDT in hypoxic environments.[104]

In addition, by decreasing the number of optical cargos, researchers can potentially include additional cargos for other functionalities. Wang et al. designed Fe_3O_4 magnetic nanoclusters that were loaded with cypate before being coated with RBC-membranes.[63] Here, 808 nm laser irradiation of the cypate is used for *in vivo* fluorescence imaging and PTT, while the Fe_3O_4 magnetic nanoclusters allow the constructs to be used for MRI. There are a large number of potential optical cargos that can be used to give RBC-based constructs both imaging and phototherapeutic abilities. By combining them with other cargos researchers can continue to develop more constructs that can be tailored to specific disease states.

2.4.4.2 *Imaging and Drug Delivery*

A less common combination of applications is imaging and drug delivery. In some cases, the optical cargo is used not only as an imaging agent, but also as a catalyst for drug release. For instance, Marvin et al. designed a light-response vitamin drug conjugate composed of Cy5, vitamin B12, and the chemotherapeutic drug taxane.[118] Once the conjugates are loaded into RBCs, the membrane impermeable B12 ensures the drug remains inside the carrier until it has reached its target. Then Cy5 is able to be excited by 650 nm wavelength light, cleaving the bond between taxane and B12, resulting in taxane

being able to leave the RBC carrier.[118] Not only were the constructs able to be used for site-specific drug release, but they were also used for imaging *in vivo.*

Another example of an RBC-derived construct that combines drug delivery and imaging capabilities is the construct fabricated by Liu et al. Zinc gallogermanate nanostructures are coated with mesoporous silica and then loaded with DOX before being coated with RBC-membranes.[119] The constructs had an NIR signal due to the zinc gallogermanate nanostructures that was visible *in vivo* for up to 48 hours, and the anti-tumor activity of the constructs outperformed a control injection of just DOX.

While both of the previous examples are specifically for cancer imaging and treatment, there is a clear potential for therapeutic imaging and drug delivery to be applied to vascular targets. As a prospective RBC-based thrombus therapy, we have developed nano-sized constructs of ICG loaded nEGs functionalized with tissue plasminogen activator (tPA).[35] The tPA allows the constructs to target the fibrin in the clot, while the ICG loaded into the nEGs allows for NIR fluorescence imaging of the clot. We showed that these constructs were able to induce lysis of blood clot models.[35] Overall, it is clear that RBC-derived constructs have demonstrated their efficient imaging and drug delivery capabilities; however, there are more common application combinations that are just as promising.

2.4.4.3 *Phototherapy and Drug Delivery*

Combining PTT and/or PDT with drug delivery is very common for light-based RBC-derived constructs, a majority of which are developed for cancer applications. For

example, Pei et al. developed RBC-membrane camouflaged NPs with a polymeric core containing dimers of the chemotherapy drug paclitaxel as well as 5,10,15,20-tetraphenylchlorin (TPC) as an optical cargo for PDT.[120] On the other hand, Wang et al. recently reported the design of RBC-membrane coated BSA nano-constructs loaded with ICG for PTT, and gambogic acid as a chemotherapeutic.[28] With a large number of potential optical cargos and chemotherapeutics available, the possible combinations could result in many different RBC-derived particle formulations. By continuing to investigate different optical cargo and drug combinations, it is possible that multiple therapies will be developed and can be tailored to the treatment of specific cancers. However, the most common drug investigated for use in RBC-derived constructs is DOX. DOX is currently used to treat various cancers including breast, ovarian, bladder, and lung cancers.[121]

Chen et al. fabricated DOX-based constructs by loading hollow mesoporous PB NPs with DOX and then coating them in RBC membranes, and demonstrated their strong PTT and anti-tumor effect *in vivo* after NIR laser irradiation.[52] Another DOX example was designed by Hui et al. and involves loading DOX and ICG in upper critical solution temperature (UCST) polymer micelles that are then coated with RBC membranes.[20] These particles were also capable of efficient PTT, and their cytotoxicity *in vitro* was increased after NIR laser irradiation.

The previous examples combine drug delivery with either PTT or PDT, but not both. However, it is possible to design constructs are capable of drug delivery, PTT, and PDT simultaneously. This can be achieved by using an optical cargo capable of both PTT and PDT, such as ICG. For instance, Luo et al. loaded graphene oxide QDs with ICG and

DOX which were then loaded into nEGs.[26] The constructs showed strong PTT and PDT effects *in vitro*, and in combination with the drug delivery and 808 nm laser irradiation had an impressive anti-tumor effect *in vivo*. Another example that incorporates ICG are the previously mentioned NPs made by Liu et al. RBC-membranes are used to coat nanocomplexes containing BSA, ICG, and DACHPt as a chemotherapeutic.[23] The particles were capable of *in vitro* hyperthermia and ROS generation after NIR laser irradiation, and demonstrated efficient anti-tumor and anti-metastatic abilities *in vivo.* The authors note that the drug release was enhanced by the NIR laser irradiation, which suggests that the drug release mechanism is mediated by the PTT and PDT effects of the construct.[23]

All of these examples illustrate the powerful cancer applications light-based RBC-derived constructs are capable of when they are designed to combine phototherapy and drug delivery. However, there are also examples of phototherapy and drug delivery constructs being used for other potential clinical applications. Shao et al. have developed Janus-type polymeric micromotors coated with RBC membranes that are capable of being directed to thrombus sites using NIR light irradiation.[122] Here, the core of the construct is a capsule made of heparin and chitosan that is partially coated in gold before encapsulation in nEGs. NIR laser irradiation of the gold coating led to a temperature gradient around the construct, enabling its directed motion using a thermophoretic effect.[122] In addition to using NIR light to induce directed movement of the constructs, the NIR light was able to induce photothermal destruction of thrombus models. The generated heat also mediated the release of heparin from the constructs to aid in

thrombolysis. This example demonstrates that in addition to having great promise in the realm of cancer treatments, light-based RBC-derived constructs can be designed for phototherapy and drug delivery for vascular applications.

2.4.4.4 *Imaging, Phototherapy, and Drug Delivery*

As previously mentioned, a common method for increasing the number of applications a construct can be used for includes using optical cargos capable of more than one application. By carefully choosing an optical cargo that can be used for imaging and phototherapy and combining it with a drug, some light-based RBC-derived constructs can be used for imaging, phototherapy, and drug delivery simultaneously. Here it is very common to choose an organic molecule as the optical cargo. As previously mentioned, Ye et al. engineered constructs where the chemo-drug HCPT and ICG co-assembled NPs are coated with RBC-membranes. Here, ICG is able to be used for fluorescent imaging after NIR laser irradiation, as well as PTT. The generated heat disrupts the construct's membrane, causing the release of the HCPT.[24] Similarly, Su et al. developed mesoporous silica NPs co-loaded with DOX and the NIR dye Ce6 that are coated with RBC-membranes.[123] After laser irradiation, Ce6 was not only able to serve as a fluorescent probe, but also resulted in the generation of ROS. The authors hypothesize the ROS generation could not only destroy tumor cell membranes, but the EG membranes as well, leading to the release of DOX from the construct.

PB NPs are another common optical cargo for constructs that can be used for imaging, phototherapy, and drug delivery. Liu et al. have demonstrated that hollow mesoporous PB NPs can be loaded with the chemotherapeutic gamabufotalin before

being encapsulated in RBC-membranes.[124] After 808 nm laser irradiation the constructs were capable of being used for NIR fluorescence imaging as well as displaying effective anti-tumor activity from the PTT and drug delivery.[124]

It is important to note that since many optical cargos are capable of being used for more than one light-based application, it is possible that some constructs are capable of being used for imaging, phototherapy, and drug delivery, despite only being designed for one or two of those applications. For instance, since ICG has been used for imaging, PTT, and PDT,[125] constructs fabricated with ICG can potentially be used for all three applications even if they were only initially designed for one. Therefore, many light-based RBC-derived constructs are inherently endowed with multifunctionality, representing a promising treatment platform that has been particularly studied for cancer applications.

2.4.5 *Specific Considerations for Targeting Cancer Cells*

PDT and PTT are two of the more common treatment modalities RBC-derived particles have been developed to utilize. Both PDT and PTT are being heavily investigated for their use in the treatment of cancer,[126] so it follows that a large number of light-based RBC-derived platforms are designed specifically for applications in the treatment of various cancers. There is a recent review by Sun et al. that covers a number of different RBC-derived formulations explicitly fabricated for the treatment of cancer,[14] with a focus on platforms that involve the various functionalization methods for conferring NPs with targeting capabilities. In addition, RBC-derived constructs have also been extensively

reviewed for their drug delivery abilities,[2,4,7,9,10] including their utility in drug delivery for anti-tumor applications.[13] It is therefore no surprise that the vast majority of light-based RBC-derived constructs are developed for cancer treatment.

In order for RBC-derived constructs to have any anti-cancer efficacy they need to be able to reach their target efficiently. Targeting various types of cancer cells can be accomplished using multiple techniques during the design phase for the RBC-derived particles. For instance, a majority of these formulations are on the nano-scale, meaning they are capable of passively targeting cancer cells via the enhanced permeability and retention (EPR) effect.[127] Tumor vasculature is abnormal and hyperpermeable,[128] which enables NPs to more readily accumulate in tumors compared to healthy tissues. While many constructs rely only on the EPR effect in order to ensure cancer targeting, the EPR effect has been shown to be heterogeneous in humans.[129] Researchers have therefore started to employ various functionalization methods to bestow their constructs with more active targeting capabilities, bypassing the need for passive targeting via the EPR effect. Based on our review of the literature, the most common method for functionalizing RBC membranes involves DSPE-PEG-χ lipid insertion. As previously mentioned, DSPE is able to insert itself into the lipid bilayer of the RBC membranes, resulting in the desired functional group, χ, being attached to the surface of the RBC membranes. Common functional groups include FA, which is able to target folate receptors overexpressed on a number of different cancer cells;[130,131] as well as various formulations of RGD peptides, which are able to selectively bind to $\alpha_V\beta_3$ integrins,[132] which are also expressed on some

tumor cells.[133] Examples of light-based RBC-derived constructs that are functionalized via DSPE lipid insertion are listed in Table 1.

While there are relatively few functionalized RBC-derived constructs that utilize light that have been developed, almost all of them have been designed for cancer applications. For example, Luo et al. designed RBC-derived ICG and DOX-containing NPs for the chemo-PPT of cervical cancer.[26] After functionalizing the NPs with FA, the researchers saw a significant improvement in the tumor accumulation of their constructs.

Table 1. Examples of RBC-derived Constructs with an Optical Cargo Functionalized Using DPSE Lipid Insertion.

Optical Cargo	Targeting Moiety	Target	Reference
Upconversion nanoparticles (UCNPs)	Folate	Folate receptors	65
UCNPs	Folate	Folate receptors	54
UCNPs	Triphenylphosphonium cation	Mitochondria	54
Black Phosphorus Nanoparticles (NPs)	YSA peptide	Ephrin-A2 receptors	134
Indocyanine Green (ICG)	Angiopep-2 peptide	Lipoprotein receptor-related proteins receptors	27
ICG	cRGD pentapeptide	$\alpha_v\beta_3$ integrin	23
ICG	Folic acid	Folate receptors	26
Spheric and Cubic Hollow Mesopores Prussian Blue (PB) NPs	Folic acid	Folate receptors	135
PB NPs	Hyaluronic acid	CD44 receptors	124
ICG-Bovine Serum Albumin (BSA), UCNPs, Rose Bengal (RB)	RGD peptide functionalized UCNPs	$\alpha_v\beta_3$ integrin	25
ICG-BSA	RGD peptide	$\alpha_v\beta_3$ integrin	19

Gold Nanocages	anti-epithelial cell adhesion molecule (EpCam) antibodies	EpCam	[61]

Other groups have also been able to use functionalization to improve the targeting ability of micro-sized constructs that would not be able to rely on the EPR effect for tumor accumulation. Wang et al. functionalized RBCs with UCNPs coated in RGD peptides and saw that the RGD peptides supplied their constructs with tumor targeting abilities *in vivo*.[25]

In addition to functionalization, other targeting methods include the application of various stimuli, including magnetic and acoustic fields. For instance, Gao et al. showed that RBC membrane wrapped particles containing Fe_3O_4 NPs and ICG could be propelled using an acoustic field and that the direction of these particles could be controlled using a magnetic field for the targeted delivery of ICG for PDT.[67] Other groups have shown that loading RBC-membrane derived particles with magnetic mesoporous silica NPs,[136] Fe_3O_4@$Cu_{2-x}S$ NPs,[137] and Fe_3O_4 NPs[48] increased the tumor uptake of the particles when combined with the application of a magnetic field.

Another recently developed targeting method is combining the RBC membranes with the membranes of other cells to create hybrid membrane coatings. Liu et al. combined RBC membranes and platelet membranes and showed that constructs derived from those hybrid membranes had more tumor accumulation compared to constructs fabricated from just RBC membranes or platelet membranes.[138] The platelet membranes give the constructs the ability to target microthrombi, which are created when NIR light is applied to the tumor, resulting in the enhanced tumor accumulation. A collaborating

group, Jiang et al., has also had success in enhancing tumor targeting by combining RBC membranes with MCF-7 cancer membranes to coat melanin NPs.[139] They showed that the cancer membranes were able to be used for the homotypic targeting of MCF-7 cancer cells and saw enhanced tumor PTT when the RBC:MCF-7 membrane ratio was 1:1. Wang et al. also used cancer membranes to make hybrid membranes when they fused RBC membranes with melanoma B16-F10 cell membranes to coat copper sulfide (CuS) NPs.[45] They saw that the combination of the two cell membranes allowed for greater tumor accumulation of the CuS NPs compared to NPs coated with just one type of membrane. Overall, there are a number of different promising methods for endowing RBC-derived light-based constructs with the ability to target cancer cells. Since the field is still fairly young more targeting methods will undoubtably arise as researchers continue to push the boundaries of the field.

2.5 Trends in Biocompatibility and Toxicology

Overall, the *in vitro* results for studies with RBC-derived constructs that utilize light have been very promising. However, *in vivo* results will ultimately be more important for clinical translation and will be the focus of our discussion. There are a number of different experiments researchers have been conducting in order to determine not only the efficacy of RBC-derived constructs, but also their biocompatibility. For instance, Wan et al. saw that after a series of injections of their RBC-derived constructs there was no significant change in the mouse body weight, and there was no visible damage in the mouse organs as shown by histology.[22] Monitoring the mouse body weight and examining the organ histology are only two of the methods researchers commonly use to

determine the biocompatibility of drug delivery vehicles. Researchers also look at a number of blood parameters, such as white and red blood cell counts, mean corpuscular volume, hemoglobin, hematocrit, and platelet counts. We recently demonstrated that injection of our micro- and nano-sized RBC-derived constructs did not result in any of the mentioned blood parameters being outside the normal range.[73] In addition, we saw that our RBC-derived particles had minimal effects on hepatic (alanine aminotransferase (ALT), aspartate aminotransferase (AST), and alkaline phosphatase (ALP)) and renal (urea nitrogen and creatinine) function assays.

While many of these tests are conducted in healthy mice, they can also be done in disease models, such as cancer, to demonstrate the effectiveness of the RBC-derived constructs for their designed application. For instance, Liu et al. showed that tumor bearing mice showed no organ damage after injections of their RBC-derived constructs with and without laser irradiation, but also showed that the damage to tumor tissue increased when the particles were combined with laser irradiation, as shown by histology.[46] Another example is the work done by Pei et al. where they showed that in tumor bearing mice their RBC-derived constructs combined with laser irradiation led to no significant changes in mouse body weight, as well as no damage to organs, and no change in ALT, AST, uric acid, urea, and creatinine serum levels.[120] However, they did see damage to the tumor when their constructs were used in conjunction with laser irradiation. In addition, the RBC-membrane coating led to a decrease in liver accumulation, but an increase of their constructs in the tumor.

A majority of the *in vivo* results are similarly effective, but they focus on the biodistribution of the RBC-derived particles, as well as looking for any obvious signs of toxicity. However, very few RBC-derived particles have had their immune system interactions assessed. One example is the work done by He et al. where they looked at the serum levels of cytokines interleukin (IL)-6, IL-12, and tumor necrosis factor (TNF)-α 24-72 hours after injection of their RBC-derived particles. They saw that the RBC coated constructs did not induce elevated levels of the investigated cytokines compared to a control injection at any of the time points.[51] Sun et al. also showed that injections of their RBC-derived constructs did not induce elevated blood serum levels of TNF-α for up to 7 days post-injection compared to a control.[85]

However, these studies do not look at the immediate immune responses, nor do they look at the effect of multiple injections of RBC-derived platforms. Rao et al. looked at the IgM and IgG levels in blood samples of mice that had received two injections of their NPs, and saw that there were no differences in the IgM and IgG levels compared to mice that had received one injection of the NPs, suggesting that the adaptive immune system had not been activated.[140] We have also recently investigated the acute innate immune response in mice and found that micro- and nano-sized RBC-derived constructs do elevate the blood serum, liver, and spleen levels of cytokines IL-6, TNF-α, and monocyte chemoattractant protein (MCP)-1 compared to a negative control (while still being lower than the levels induced by a lipopolysaccharide positive control) within 6 hours of injection.[141] We also show that a second injection of these particles does not induce significantly elevated levels of the mentioned cytokines, which further suggests

that RBC-derived particles do not activate the adaptive immune system. There is a clear need for more research into the immunogenicity of RBC-derived particles, particularly when looking at the effect of multiple injections of the particles.

2.6 Outlook

Combining RBC delivery systems with light-based treatment modalities is an exciting field that is still being developed. Constructs are able to be designed in a number of different ways, allowing for them to be tailored to specific targets for seemingly endless applications. We have broadly divided light-based RBC-derived constructs into two main categories: constructs that use an RBC-membrane as a coating, and constructs that use the RBC, EG, or nEG as a carrier. Deriving the constructs from RBCs endows their cargos with immune-escaping capabilities, as well as the potential for increased circulation time. In addition, numerous methods have been employed to give RBC-derived constructs targeting capabilities. These methods include functionalizing the constructs with a targeting moiety; using cargos that can have their motion directed using light, magnetic fields, or acoustic fields; and combing RBC membranes with other cell membranes capable of specific interactions with the target.

Many of the studies discussed above have demonstrated that RBC-derived constructs are very effective for light-based theranostics, particularly for cancer imaging, phototherapy, and drug delivery. However, we have also highlighted the potential for light-based RBC-derived constructs to be used in vascular applications as well. In addition, a majority of the studies suggest that these constructs have excellent

biocompatibility as well as low toxicity. However, the field is still fairly young, and before many of these constructs can be used in a clinical setting, there is still a large amount of work to be done. For example, researchers are just beginning to probe the potential immune interactions of these constructs. While results are promising, understanding the potential immune response to any of these constructs is necessary before clinical translation can be realized.

Using materials that are already approved for human use by the U.S. Food and Drug administration, such as ICG and MB,[17] may help accelerate approval for human studies. Other potential hurdles to clinical translation are recently reviewed by Singh et al. and include difficulties with scaling production from a small academic lab to an industrial scale, and thoroughly understanding the potential dangers of a construct, including its cyto-, immuno-, and geno-toxicity.[142] In addition, the constructs need to be fabricated in sterile environments using only materials approved for human use (i.e., materials that are not labeled "For Research Use Only"). Researchers in the U.S. will also have to work with Institutional Review Boards for approval for any human studies.

Many of the light-based RBC-derived constructs highlighted here have been fabricated within the past 10 years. These constructs have frequently only been used in one animal study that demonstrates the effectiveness of the constructs for light-based applications. In addition, only some of these studies touch on the biodistribution of the construct. Therefore, there is a large need for more research into the biological interactions of the constructs once they are used *in vivo*. In addition, more effort needs to be given to standardizing the methods for fabricating these constructs, which will ease

production scaling difficulties. Overall, despite the urgent need for more research, the field of light-based RBC-derived constructs is very promising. New constructs are constantly being developed, increasing the potential for new therapeutics for ultimate clinical translation.

Chapter 3: The Acute Immune Response of Micro- and Nano-sized Erythrocyte-Derived Optical Particles in Healthy Mice

3.1 Abstract

Erythrocyte-derived particles activated by near-infrared (NIR) light present a platform for various photo-theranostic applications. We have engineered such a platform with indocyanine green (ICG) as the NIR-activated agent. A particular feature of these particles is that their diameters can be tuned from micro- to nano-scale, providing a potential capability for broad clinical utility ranging from vascular to cancer-related applications. An important issue related to clinical translation of these particles is their immunogenic effects. Herein, we have evaluated the early-induced innate immune response of these particles in healthy Swiss Webster (SW) mice following tail vein injection by measurements of specific cytokines in blood serum, liver, and spleen following euthanasia. In particular, we have investigated the effects of particles size and relative dose, time-dependent cytokines response for up to 6 hours post-injection, functionalization of the nano-sized particles with folate or Herceptin®, and dual injections of the particles one week apart. Mean concentrations of Interleukin (IL)-6, IL-10, tumor necrosis factor (TNF)-α, and monocyte chemoattractant protein (MCP)-1 in

response to injection of micro-sized particles at the investigated relative doses were significantly lower than the corresponding mean concentrations induced by lipopolysaccharide (positive control) at 2 hours. All investigated doses of the nano-sized particles induced significantly higher concentrations of MCP-1 in liver and spleen as compared to phosphate buffer saline (PBS) (negative control) at 2 hours. In response to micro- and nano-sized particles at the highest investigated dose, there were significantly higher levels of TNF-α in blood serum at 2 and 6 hours post-injection as compared to the levels associated with PBS treatment at these times. Whereas the mean concentration of TNF-α in liver significantly increased when comparing the levels 2 and 6 hours post-injection in response to the injection of the micro-sized particles, it was significantly reduced when comparing 2 and 6 hours following the injection of the nano-sized particles. In general, functionalization of the nano-sized particles was associated with a reduction of IL-6 and MCP-1 in blood serum, liver, and spleen, and TNF-α in blood serum. With the exception of IL-10 in the spleen in response to nano-sized particles, the second injection of micro- or nano-sized particles did not lead to significantly higher concentrations of other cytokines at the investigated dose as compared to a single injection.

3.2 Introduction

Use of near-infrared (NIR) light provides a capability for relatively deep biomedical optical imaging and phototherapy on the order of a few centimeters.[143,144] This increased depth of optical penetration results from minimal absorption and scattering by biological components over the NIR spectral band (≈ 700-2,500 nm).[143,145] When combined with exogenous use of NIR fluorochromes, improved image contrast can be achieved as a result of reduced autofluorescence. To-date, indocyanine green (ICG) remains as the only NIR fluorochrome approved for use in humans by the United States Food and Drug Administration for specific clinical applications including retinal angiography[15] and assessment of liver function.[16]

Despite ICG's usage in both clinical procedures and investigational research,[146,147] ICG has a short half-life in plasma following intravascular administration (on the order of 3-4 minutes) with nearly exclusive uptake by hepatocytes and elimination from the body by hepatobiliary mechanism.[18,148] Given the long circulation time of erythrocytes (on the order of 3-4 months) and their potential biocompatibility, they present an attractive platform for encapsulation of various cargos including ICG.[1,2,4,39,149] We reported the first results to encapsulate ICG into nano-sized constructs derived from erythrocytes.[150] We refer to these constructs as NIR erythrocyte-derived transducers (NETs) since they can transduce the absorbed NIR light to emit fluorescence, generate heat, or mediate the production of reactive oxygen species.[30,151] We have also demonstrated that NETs can be functionalized with appropriate antibodies for targeted imaging of specific cell

receptors.[33,152] Other investigators have also reported the use of erythrocyte-encapsulating ICG nanoparticles for light-mediated therapeutic applications. [153–156]

One feature of NETs is that their diameters can be tuned from micro- to nano-sized via sonication or mechanical extrusion,[157] thereby providing a capability to develop a versatile platform for broad biomedical and clinical applications. Nano-sized NETs (nNETs) (diameter < 200 nm) have relevance to tumor imaging and phototherapy via the enhanced permeability and retention (EPR) effect.[32] Micro-sized NETs (μNETs) (diameter > 1 μm) have the potential for vascular imaging and photo-thermal treatment of cutaneous capillary malformations known as port wine stains (PWSs).[31,151]

An important issue related to the use of NETs, as well as other erythrocyte-based delivery systems in clinical applications, is their potential immunogenic effects. Herein, we evaluate the early-induced innate immune response to μNETs and nNETs in healthy Swiss Webster (SW) mice following tail vein injection by measurements of specific cytokines in blood serum, liver, and spleen after euthanasia. In particular, during this acute-phase, we investigate the effects of the particles' relative dose (relative number concentration), and time-dependent changes in the cytokines concentrations at 2, 4, and 6 hours post-injection of the particles. We also evaluate the acute-phase immunogenicity of nNETs functionalized with folate or Herceptin® as clinically-relevant molecules that respectively target the folate receptor-α and human epidermal growth factor-2 (HER-2) on specific tumor types.[130,131,158–161] Finally, we investigate the immunogenic effects of dual injections administered one week apart.

3.3 Materials and Methods

3.3.1 *Fabrication of NETs*

Whole blood was drawn from healthy female SW mice using syringes coated in 2 mg/ml lithium heparin in nanopure water and stored in a flask containing ≈ 100 µl lithium heparin solution per 1 ml of mouse blood. Blood from ≈ 20 mice was drawn and pooled together to get a total volume of 20 ml of whole blood. Erythrocytes were separated from whole blood via centrifugation (≈ 2,800x *g* for 10 minutes at 4°C). The plasma and buffy coat were removed, and erythrocytes were washed in ≈ 320 mOsm phosphate buffered saline (PBS) (defined as 1xPBS) (Fisher Scientific). Erythrocytes were spun down (≈ 2,800x *g* for 10 minutes at 4°C), the supernatant was removed, and the 1xPBS wash was repeated.

The intracellular hemoglobin of the erythrocytes was removed by hypotonic treatment. Specifically, erythrocytes were suspended in 0.25xPBS (≈ 80 mOsm) for ≈ 10 minutes at 4°C and then centrifuged (≈ 31,000x *g* for 20 minutes at 4°C). After centrifugation the hemoglobin-containing supernatant was discarded, and the erythrocytes were re-suspended in 0.25xPBS. Hemoglobin depletion steps were repeated until the erythrocyte pellet was opaque, indicating the formation of erythrocyte ghosts (EGs). The pellet was then re-suspended in 1xPBS.

To load ICG (MP Biomedicals) into EGs, 1 ml of EGs in 1xPBS was suspended in 1 ml of 0.1 M Sorenson's buffer (Na_2HPO_4/NaH_2PO_4, 140 mOsm, pH ≈ 8), and 1 ml of 75 µM ICG in nanopure water. The final concentration of ICG in the loading solution was 25 µM. The samples were allowed to incubate for ≈ 10 minutes at 4°C, then centrifuged (≈ 56,000-70,000x *g* for 1 hour at 4°C), and the supernatant removed. The pellet was re-

suspended in 1xPBS and centrifuged again (≈ 56,000x *g* for 1 hour at 4°C). The supernatant was removed a final time, resulting in a μNETs pellet, which was then resuspended in ≈ 1-1.5 ml of 1xPBS. We refer to this dose of μNETs solution as 1x μNETs. To reduce the dose, 1x μNETs were diluted 1:1 with 1xPBS resulting in 0.5x μNETs. Similarly, the 0.5x μNETs were diluted 1:1 with 1xPBS to get 0.25x μNETs. We note that since the lower doses of μNETs were diluted from the same solution of 1x μNETs, the relative protein and ICG content as well as the number of particles would be scaled accordingly.

To fabricate nNETs, EGs were formed as described above, and then diluted 1:10 in 1xPBS prior to an extrusion procedure. The diluted EGs were then extruded 3 times through 800 nm polycarbonate porous filters (Whatman) using a 10 ml automatic extruder (LIPEX Extruder, Evonik Canada Inc.). The resulting nano-sized EGs (nEGs) were then centrifuged (≈ 70,000x *g* for 1 hour at 4°C), and the supernatant was removed. The nEGs were resuspended in a volume of 1xPBS that was 10% of the volume of the supernatant removed, resulting in a 10:1 concentration ratio. The nEGs were then hypotonically loaded with ICG by adding 1 ml of nEGs suspension in 1xPBS to 1 ml 0.1 M Sorenson's buffer, and 1 ml 75 μM ICG in nanopure water as described above. The solution was then centrifuged and washed as described above, resulting in a nNETs pellet, which was then resuspended in ≈ 1-1.5 ml of 1xPBS. We refer to this dose of nNETs solution as 1x nNETs. To reduce the dose, 1x nNETs were diluted 1:1 with 1xPBS resulting in 0.5x nNETs. Similarly, the 0.5x nNETs were diluted 1:1 with 1xPBS to get 0.25x nNETs. Similar to the μNETs, the relative protein and ICG content as well as

the number of particles would be scaled accordingly by diluting the 1x solution of nNETs.

3.3.2 *Fabrication of Folate-Functionalized nNETs (FF-nNETs) and Herceptin®-Functionalized nNETs (HF-nNETs)*

To fabricate FF-nNETs, EGs were first prepared as described above. We then prepared a 5 mg/ml solution of 1,2-distearoyl-sn-glycero-3-phosphoethanolamine-N-[folate(polyethylene glycol)] (DSPE-PEG-FOL) (2 kDa PEG, Nanosoft Polymers) in ≈ 100°C nanopure water. The nanopure water was heated to fully dissolve the DPSE-PEG-FOL. We then incubated ≈ 200 µl of the DSPE-PEG-FOL solution with 1 ml of the EGs suspension in 1xPBS for 30 minutes at room temperature, allowing the insertion of the DPSE component into the membrane of the EGs. This lipid-insertion method has also been reported for the functionalization of erythrocyte membrane-cloaked nanoparticles.[88] The DSPE-PEG-FOL bearing EGs were then diluted 1:10 in 1xPBS and extruded as described above, resulting in DSPE-PEG-FOL bearing nEGs. The DSPE-PEG-FOL bearing nEGs were centrifuged (≈ 70,000x *g* for 1 hour at 4°C), and the supernatant containing any excess DSPE-PEG-FOL was removed. The DSPE-PEG-FOL bearing nEGs were then re-suspended in a volume of 1xPBS equal to 10% the volume of the supernatant removed, resulting in a 10:1 concentration of the DSEP-PEG-FOL bearing nEGs. The DSPE-PEG-FOL bearing nEGs were then hypotonically loaded with ICG by adding 1 ml suspension of these particles in 1xPBS to 1 ml of 0.1 M Sorenson's buffer, and 1 ml of 75 µM ICG in nanopure water as described above. The particles were then centrifuged and washed, as

described above. The resulting FF-nNETs pellet was re-suspended in ≈ 1-1.5 ml 1xPBS. We refer to this dose of particles as 1x FF-nNETs.

To fabricate HF-nNETs, we used a methodology similar to our previous report in functionalizing nNETs with HER2 antibodies.[33] We first prepared a 1 mg/100 µl Herceptin® (gifted by Genentech) solution in nanopure water. Herceptin® was oxidized by mixing 30 µl of the Herceptin® solution with 20 µl of 100 mM sodium periodate ($NaIO_4$) (Acros Organics) in nanopure water and 50 µl 1xPBS. The solution was incubated at room temperature in the dark for 30 minutes. Excess oxidizing agent was removed by filtering the oxidized Herceptin® through 100 kDa centrifugation filter tubes (Millipore Amicon) via centrifugation (≈ 3,000x *g* for 5 minutes at room temperature). The oxidized Herceptin® was re-suspended in 1xPBS and the filtration step was repeated for a total of three spins. The oxidized Herceptin® was then re-suspended in 100 µl of 1xPBS.

To covalently attach the oxidized Herceptin® to the surface of NETs, we used DSPE-PEG-amine (DSPE-PEG-NH_2) (2 kDa PEG, Nanocs Inc.) as a linker molecule. EGs in 1xPBS were prepared as described above, and then incubated with 1 mg/ml of the DSPE-PEG-NH_2 lipid linker at room temperature for 30 minutes, resulting in lipid insertion of the DSPE component of the linker. The resulting DSPE-PEG-NH_2 bearing EGs were then diluted 1:10 in 1xPBS and extruded as described above. The resulting nano-sized constructs were then hypotonically loaded with ICG by adding 1 ml suspension of these particles in 1xPBS to 1 ml of 0.1 M Sorenson's buffer, and 1 ml of 75 µM ICG in nanopure water as described above. The particles were then centrifuged as described above, and then re-suspended in ≈ 150 µl of 1xPBS, resulting in DSPE-PEG-NH_2 bearing nNETs. The 100

µl of oxidized Herceptin® was then added to the ≈ 150 µl of DSPE-PEG-NH_2 bearing nNETs and allowed to incubate for 5 minutes at room temperature. The solution was then incubated with 10 µl of 20 mM sodium dithionite, as the reducing agent, for 1 hour at 4°C in the dark, resulting in covalent-coupling between the amine on the PEG lipid linker and the aldehyde on the oxidized Herceptin® via reductive amination. The resulting HF-nNETs were washed in 1xPBS as described above, and then re-suspended in ≈ 1-1.5 ml 1xPBS to produce 1x HF-nNETs.

In order to confirm functionalization with Herceptin®, an aliquot of the HF-nNETs were also incubated with Goat Anti-Human IgG FITC-labeled antibody (Southern Biotech) for 1 hour at 4°C in the dark, and washed with 1xPBS as described above. The resulting solution was characterized as described below.

3.3.3 *Characterization of Particles*

We used dynamic light scattering (DLS) (Zetasizer Nanoseries, NanoZS90, Malvern Instruments) to estimate the hydrodynamic diameters of all particles suspended in 1xPBS. For µNETs measurements, we used a 1:20 dilution in 1xPBS of the 1x solution. For all other particles, we used a 1:40 dilution in 1xPBS of the 1x solutions to perform the DLS measurements. All measurements were made with the particle suspensions in polystyrene cuvettes with a 1 cm pathlength. Measurements were collected three times for each sample, and used to determine the mean diameter and standard deviation (SD) for each sample population. For all other characterization measurements (i.e., zeta-potentials and

fluorescence spectra) we used a 1:80 dilution in 1xPBS of the 1x particle solutions unless otherwise noted.

We measured the zeta-potentials (Zetasizer Nanoseries, NanoZS90, Malvern Instruments) of the particles suspended in 1xPBS using folded capillary cells. Measurements were collected five times for each sample, and used to determine the mean zeta potential and SD for each sample population.

We acquired the fluorescence spectra of all types of particles in response to photo-excitation at 720 ± 2.5 nm filtered from a 450W xenon lamp using a fluorometer (Fluorolog-3 spectrofluorometer, Edison). We obtained the normalized wavelength (λ)-dependent fluorescence emission $\chi(\lambda)$ as follows:

$$\chi(\lambda) = \frac{F(\lambda)}{1-10^{-A(\lambda_{ex})}} \qquad (1)$$

where F is the fluorescence emission intensity in response to the excitation wavelength (λ_{ex}), and $A(\lambda_{ex})$ is the absorbance of the sample at λ_{ex}.

In order to confirm functionalization of the Herceptin®, an aliquot of the 1x HF-nNETs was diluted 1:20 in 1xPBS, resulting in 0.05x HF-nNETs. Herceptin® functionalization was confirmed by taking the fluorescence of 0.05x dose of the particles that were incubated with the FITC-labeled antibody in response to photo-excitation at 488 ± 2.5 nm, and comparing it to the fluorescence of a 0.05x concentration of HF-nNETs not incubated with the antibody. The emission of both sets of particles was collected over the 508-750 nm spectral band.

Further physical and optical characterization of nNETs and μNETs has been reported in our previous study,[157] and are not repeated here. These characterizations included ICG loading efficiency, excitation-emission maps, relative fluorescence quantum yield as functions of ICG concentration, and the photostability of NETs. We have previously provided the respective transmission and scanning electron microscopy images of non-functionalized nNETs, and nNETs functionalized with HER-2 antibodies.[33,150]

3.3.4 *Endotoxin Assessment*

To quantify the levels of endotoxin associated with μNETs and nNETs, we used the ToxinSensor™ Chromogenic Limulus Amebocyte Lysate (LAL) Endotoxin Assay Kit (GenScript). μNETs and nNETs were prepared as described above. To ensure that there was no endotoxin contribution from the solvent (PBS), particles were suspended in LAL grade water after the last centrifugation. To retain the same relative amount of RBC membranes in μNETs and nNETs, we diluted the respective particles by ≈ 30 and 12.5 times in LAL grade water so that the particles had similar absorbance values at 280 nm. Finally, μNETs and nNETs were diluted by 100 times in LAL grade water.

Once the μNETs and nNETs were prepared, we used the kit according to the instructions provided in the manufacturer's manual for endotoxin assessment. Using a spectrophotometer (Jasco-V670), we obtained the 545 nm absorbance values for three standard samples consisting of LAL grade water containing different known levels of endotoxin units (EU/ml), a blank LAL water grade standard without any endotoxin, the particles (μNETs and nNETs), and 0.5 mg/ml lipopolysaccharides (LPS) as the positive

control. Absorbance of the blank sample at 545 nm was subtracted from the absorbance values of all other samples. Using the blank-subtracted absorbance values of the standards, we then generated a calibration curve relating the endotoxin levels to 545 nm absorbance values. Endotoxin level of the μNETs and nNETs samples were subsequently determined from this calibration curve. The absorbance values of LPS were beyond the linear range of the kit due to their high endotoxin content.

3.3.5 *Animal Studies*

6-9 weeks old healthy female Swiss-Webster mice (Taconic Biosciences) were used in all studies under a protocol approved by the University of California, Riverside Institutional Animal Care and Use Committee (protocol A-20170038). Animals were anesthetized by the inhalation of 2% isoflurane gas in oxygen. All animals received via tail vein a 100 μl injection of either 1xPBS (negative control), 0.5 mg/ml LPS (Sigma-Aldrich) in nanopure water (positive control), and various types of NET particles. The LPS had a manufacturer-reported potency of ≥ 500,000 EU/mg, which corresponds to ≥ 25,000 EU per mouse injection.

In Table 2, we provide a description of the various immunogenicity studies aimed at investigating the effects of particle dose (relative number concentration), time-dependent cytokines response at various times post-injection, functionalization, and dual injections set one week apart. Upon termination of a given study, mice were euthanized by inhalation of CO_2. The number of animals in each group for all studies was four. Following euthanasia, we collected the blood by cardiac puncture and extracted the liver and spleen, two organs

associated with the reticuloendothelial system, for cytokines profiling. Blood was placed in BD Microtainer® separator tubes (Becton, Dickinson and Company) and allowed to incubate on ice for 30-60 minutes before being centrifuged at ≈ 3,400x *g* for 15 minutes at 4°C. The supernatant was collected and stored at -80 °C. The livers and spleens were flash frozen in liquid nitrogen and then stored at -80 °C.

For the organ analysis, all samples were thawed on ice at room temperature. Organs were weighed, and then suspended in a volume of lysis buffer in µl equal to five times the organ weight in mg, following a modified version of the protocol by Amsen et al.[162] The lysis buffer was composed of 150 mM sodium chloride (NaCl), 1% Triton X-100, 5 mM ethylenediaminetetraacetic acid (EDTA), 50 mM Tris·HCl, and ≈ 3.3 µl of Halt™ Protease Inhibitor Cocktail (Fisher Scientific Company) per ml of lysis buffer. Following incubation in the lysis buffer for 5-20 minutes at room temperature, organs were homogenized using a tissue homogenizer (Omni TH 115, Omni International). The resulting solutions were placed on ice for at least an hour before being centrifuged at ≈ 3,000x *g* for 15 minutes at room temperature and the supernatants were collected. Blood serum supernatants were allowed to thaw on ice at room temperature. The resulting supernatants for the organs and serum were then used for the analysis of various cytokines.

Table 2. **Description of the acute immunogenicity studies.**

Immunogenicity Study	Administered Particle	Particle Relative Dose (Relative Number Concentration)	Euthanasia Timepoint After Particle Injection	Statistics
Effect of Particle Size and Dose	µNETs, nNETs	1x, 0.5x, 0.25x	2 hours	• Brown-Forsythe one-way ANOVA, and Welch one-way ANOVA followed by unpaired Welch's t-tests (two-tailed unless otherwise noted) • One-tailed unpaired Welch's t-test for comparisons to LPS, and comparisons between doses of the same construct
Time-Dependent Cytokine Response	µNETs, nNETs	1x	2, 4, 6 hours	• Brown-Forsythe one-way ANOVA, and Welch one-way ANOVA followed by unpaired Welch's t-tests (two-tailed unless otherwise noted) • One-tailed unpaired Welch's t-test for comparisons to LPS (except comparisons between LPS at different time points)
Effects of nNETs Functionalization with Folate or Herceptin®	FF-nNETs, HF-nNETs	1x	4 hours	• Brown-Forsythe one-way ANOVA and Welch one-way ANOVA followed by unpaired two-tailed Welch's t-tests
Effects of Dual Injections of NETs One Week Apart	µNETs, nNETs	0.5x	2 hours after second injection	• Unpaired two-tailed Welch's t-tests

3.3.6 *Cytokines Assessment*

A Mouse Inflammation BD™ Cytometric Bead Array (CBA) Kit (BD, Biosciences) was used to determine the cytokine concentrations in blood serum and homogenized organs. The kit was run according to the instructions in the manufacturer's manual. Briefly, we first prepared a standard solution containing 5,000 pg/ml each of interleukin (IL)-6, IL-10, tumor necrosis factor (TNF)-α, monocyte chemoattractant protein (MCP)-1, interferon-gamma (IFN-γ), and IL-12p70 by dissolving lyophilized standards provided by the kit in 2 ml of the assay diluent made of a buffered protein solution, according to the kit's manual. We chose to assay for these cytokines as they play important roles in inflammation.[163–165] The standard solution was serially diluted with the assay diluent to get standards with 2,500, 1,250, 625, 312, 156, 80, 40, and 20 pg/ml of each cytokine. The assay diluent was considered to be a standard without any cytokines. In each assay tube, we added 50 µl of assay Capture Beads (containing equal amounts of Capture Beads for IL-6, IL-10, TNF-α, MCP-1, IFN-γ, and IL-12p70), which would bind to the designated cytokine via specific capture antibodies for each cytokine. To each tube containing assay Capture Beads, we added 50 µl of either a cytokine standard, a blood serum sample, or a homogenized organ sample. Finally, we added 50 µl of Mouse Inflammation Phycoerythrin (PE) Detection Reagent, which contains PE-conjugated anti-mouse antibodies for each of the cytokines, to all of the assay tubes. The PE served as the reporter molecule during the subsequent flow cytometry measurements. Solutions were allowed to incubate for 2 hours at room temperature in the dark, during which time the Capture Beads and PE-conjugated anti-mouse antibodies would both bind to cytokines present in the sample. At the end of the

incubation, 1 ml of Wash Buffer was added to each assay tube, followed by centrifugation for 5 minutes at 200x *g* at 4°C. We removed the supernatant, and added 300 µl of Wash Buffer to each assay tube to re-suspend the resulting pellet. The solution was then transferred to a flow cytometer tube.

Samples were analyzed using a BD LSR II flow cytometer equipped with 488 nm and 640 nm lasers. The instrument was set up according to BD's "Guide to Using BD FACSDiva Software with BD Cytometric Bead Array (CBA) Kits," and data were collected using the "Digital Instrument CBA Template" for BD FACSDiva software. Briefly, the voltages for forward scatter (FSC), side scatter (SSC), PE, and allophycocyanin (APC) fluorescence, were set to 465-475 V, 190-200 V, 445-466 V, and 365-378 V, respectively. The exact voltages were determined using cytometer setup beads from the Mouse Inflammation BD CBA kit on the day of the assay. Once the voltages were set, data were recorded for each of the cytokine standards, followed by each of the samples.

Data were exported and analyzed using FCAP Array according to BD Bioscience's "FCAP Array™ Software Version 3.0 User's Guide." Briefly, the flow cytometry data were filtered of debris, and clustered to form six distinct populations using histograms of the APC fluorescent signals, one for each of the beads that correspond to the six cytokines measured (Figure 3). The mean fluorescence intensity (MFI) of the PE fluorescent signal was measured for each population. The results from the standards for each experiment were fitted with a 5-parameter logistic curve, and the curve was used to correlate the MFI for each measurement to a concentration for the selected cytokine (Figure 4). This curve allowed us to extrapolate concentration values below the limit of detection of each cytokine,

as well as values above the maximum standard concentration of 5,000 pg/ml. It is important to note, however, that MFI values above a certain value will correlate to the upper concentration limit of the 5-parameter logistic curve, resulting in some organ populations having the same concentration value for all four measurements. Populations with all the MFI values mapped to the same concentration value were handled as discussed below.

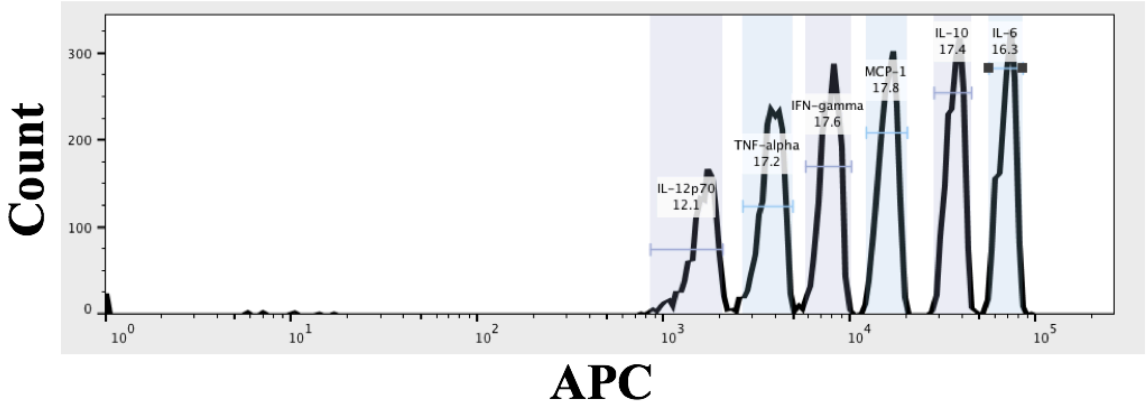

Figure 3. Representative bead clustering based on APC fluorescence emission for six separate bead populations corresponding to IL-12p70, TNF-α, IFN-γ, MCP-1, IL-10, and IL-6. Horizontal bars indicate the range of APC fluorescence intensities associated with each cytokine bead population.

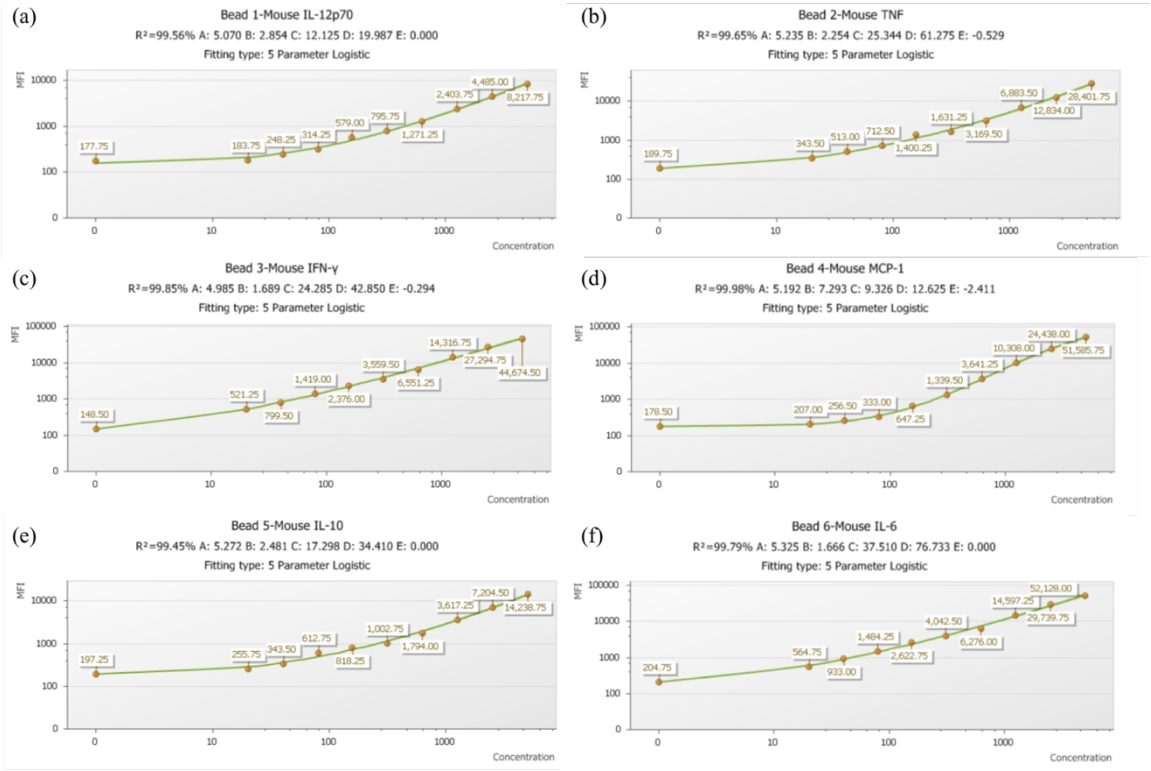

Figure 4. Representative 5-Parameter Logistic fits for (a) IL-12p70, (b) TNF-α, (c) IFN-γ, (d) MCP-1, (e) IL-10, and (f) IL-6.

3.3.7 *Data Analysis*

Concentrations for each flow cytometer measurement were analyzed using GraphPad Prism. Briefly, all of the results for one experiment were grouped together. Outliers were detected using a Grubbs' test ($\alpha = 0.05$) and removed, resulting in some of the populations having n = 3 cytokine concentrations. The concentrations were then analyzed using Brown-Forsythe and Welch ANOVA tests. We used unpaired t-tests with Welch's correction to compare the mean of one population with the means of all other populations in that group. For populations where all of the MFI values were mapped to the same concentration value, the Welch ANOVA test could not be performed. Instead we compared the mean of the

population with other population means of interest using an unpaired t-test with Welch's correction. Unless otherwise noted, all of the unpaired t-tests with Welch's correction were two-tailed (see Table 2). In order to display the cytokine concentrations on a Log 10 scale, concentration values equal to 0 were set to 0.05 pg/ml for graphical purposes. Statistical testing was done on the populations with the original 0 pg/ml concentration measurements. Finally, we used a F-test to compare the variances of two populations of interest if needed. Statistical methods associated with each immunogenicity study are summarized in Table 2.

3.4 Results

3.4.1 *Characterization of NETs*

As determined by fitting Lognormal distributions to the dynamic light scattering-based estimates of hydrodynamic diameters, the mean peak diameters (± standard deviation (SD)) of the various types of NETs were as follows: 2,738 ± 26 nm for μNETs, 109.26 ± 0.592 nm for nNETs, 91.376 ± 0.879 nm for FF-nNETs, and 106.81 ± 0.93 nm for HF-nNETs (Figures 5a, b). The mean ± SD values of zeta potentials for the particles were as follows: -14.72 ± 1.32 mV for μNETs, -14.16 ± 0.77 mV for nNETs, -11.86 ± 0.56 mV for FF-nNETs, and -15.08 ± 0.59 mV for HF-nNETs (Figure 5c). FF-nNETs had a significantly higher zeta potential than all the other particles ($p < 0.01$ for all comparisons), and nNETs had a significantly higher zeta potential than HF-nNETs ($p < 0.05$).

In response to photo-excitation at 720 ± 2.5 nm, all particle types produced similar fluorescence emission spectra (Figure 5d). The peak normalized fluorescence emission

intensity at ≈ 800 nm is associated with the monomer form of ICG. These results suggest that the diameter and the functionalization agent did not affect the fluorescence of the particles. After incubation with the Goat Anti-Human IgG FITC-labeled antibody, the HF-nNETs showed an emission peak at ≈ 525 nm (Figure 5e) in response to photo-excitation at 488 ± 2.5 nm, confirming the conjugation of Herceptin® onto NETs.

3.4.2 *Effects of Particle Size and Dose*

The respective mean concentration values of IL-6 and TNF-α in blood serum at two hours post-injection of 50 μg LPS were 20.37 and 2.86 ng/ml, respectively (Figures 6a,g). These values are comparable to the reported respective values of ≈ 12 ng/ml for IL-6 in blood serum at three hours, and ≈ 13 ng/ml for TNF-α at one hour post-injection of 50 μg LPS in C57B1/6/129-Ola mice by Berg et al.[166] As another example of validation, our estimated respective mean concentrations of 4.05 and 4.90 pg/ml for IL-6 in liver and spleen in response to PBS injection are also comparable to the reported mean baseline values of ≈ 18 pg/ml in liver and ≈ 20 pg/ml in spleen of C57BL/6 mice.[167]

Mean concentrations of IL-6, IL-10, TNF-α, and MCP-1 in response to μNETs were significantly lower than the mean concentration of these cytokines in response to LPS, regardless of μNETs dose or the site of cytokine (blood serum, liver, spleen) (Figures 6a-c, 6d-f, 6g-i, and 6j-l, respectively). Levels of both IFN-γ and IL-12p70 induced by all doses of μNETs were not significantly different from the levels induced by PBS in blood serum, liver, and spleen (data not shown). While some of the μNETs doses did lead to significantly higher levels of the cytokines compared to the levels induced by PBS, there

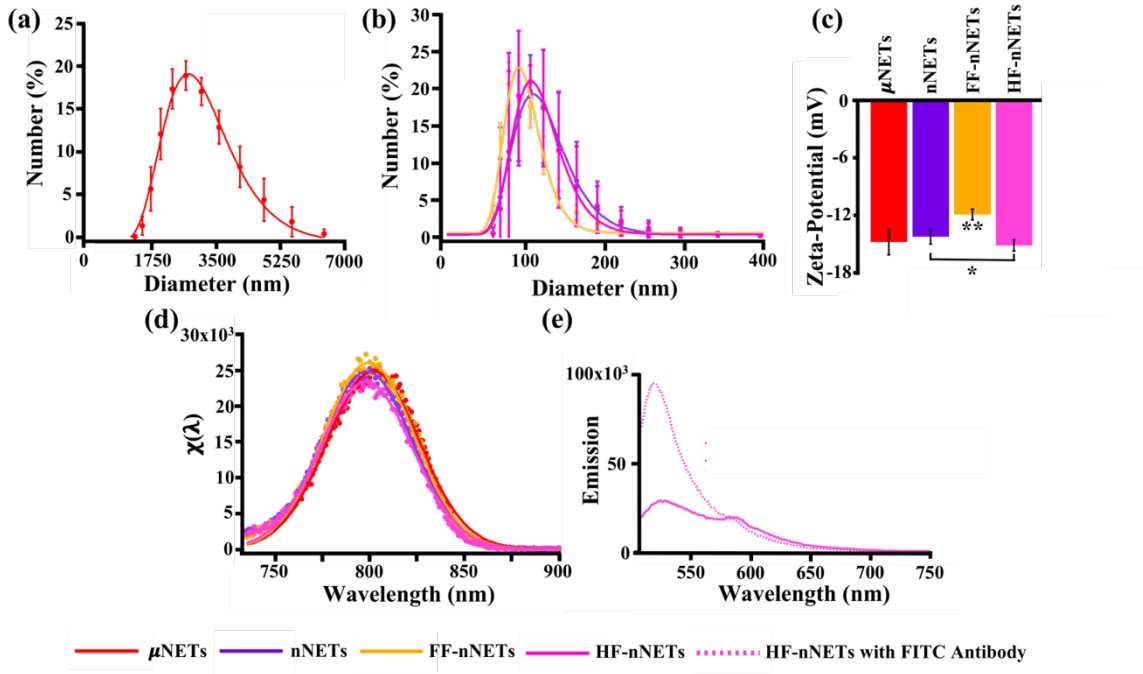

Figure 5. Characterization of the various types of NETs. Hydrodynamic diameters of (a) μNETs and (b) nNETs, FF-nNETs, and HF-nNETs as measured by dynamic light scattering. We present the average (circles) of three measurements made on each sample. Error bars are standard deviations from the average values. LogNormal fits to the measured data are shown as solid traces. (c) Zeta potentials for all particle types in 1xPBS (≈ 320 mOsm phosphate buffer saline). Average of five measurements (bars) with standard deviation (error bars) for each sample are presented. Statistical significance of * ($p < 0.05$), and **($p < 0.01$) are indicated. Significance markings directly above FF-nNETs indicates that the zeta potential for FF-nNETs is significantly different from those associated with the other particles at the indicated significance level. Bracket indicates that the zeta potential for nNETs and HF-nNETs are different from each other at the indicated significance level. (d) Normalized emission spectra (see equation 1 in manuscript) in response to photo-excitation at 720 ± 2.5 nm for all particles in 1xPBS. Data points (circles) with Gaussian fits (solid traces) are shown. (e) Raw emission spectra in response to photo-excitation at 488 ± 2.5 nm of HF-nNETs with and without incubation with FITC-labeled secondary antibody.

were no clear trends between the μNETs dose and the significantly elevated cytokine levels. In addition, there were no significant differences between the induced cytokine levels for different μNETs doses in the blood serum, liver, and spleen. Overall, these results show

that while there were some increases in the mean concentrations of IL-6, IL-10, TNF-α, and MCP-1 relative to those induced by PBS, in general they did not appear to correlate with the investigated μNETs doses, and are possibly due to variations among the response of the animals.

The levels of IL-12p70 induced by all investigated doses of nNETs were not significantly different from the levels induced by PBS in blood serum, liver, and spleen (data not shown). For IFN-γ, the levels induced by all doses of nNETs were not significantly different from those induced by PBS in blood serum and liver. In the spleen, only the 0.5x nNETs induced a level of IFN-γ that was significantly higher than that induced by PBS. However, the [IFN-γ] induced by the 0.5x nNETs was still significantly lower than that induced by LPS, and the population mean concentration of IFN-γ induced by the 0.5x nNETs was only ≈ 3 pg/ml higher than that of PBS.

The induced IL-10 mean concentration levels in response to all nNETs doses were significantly lower than those associated with LPS in the blood serum and spleen (Figures 7d,f); however, only the 1x dose of nNETs induced a significantly lower level of IL-10 in the liver compared to the levels induced by LPS (Figure 7e). In addition, there were no significant differences between the levels of IL-10 induced by PBS and any of the nNETs doses in blood serum (Figure 7d). Only the 0.5x nNETs dose resulted in significantly higher levels of IL-10 in the liver and spleen compared to PBS (Figures 7e,f). However, since there were no significant differences between the IL-10 levels induced by any of the

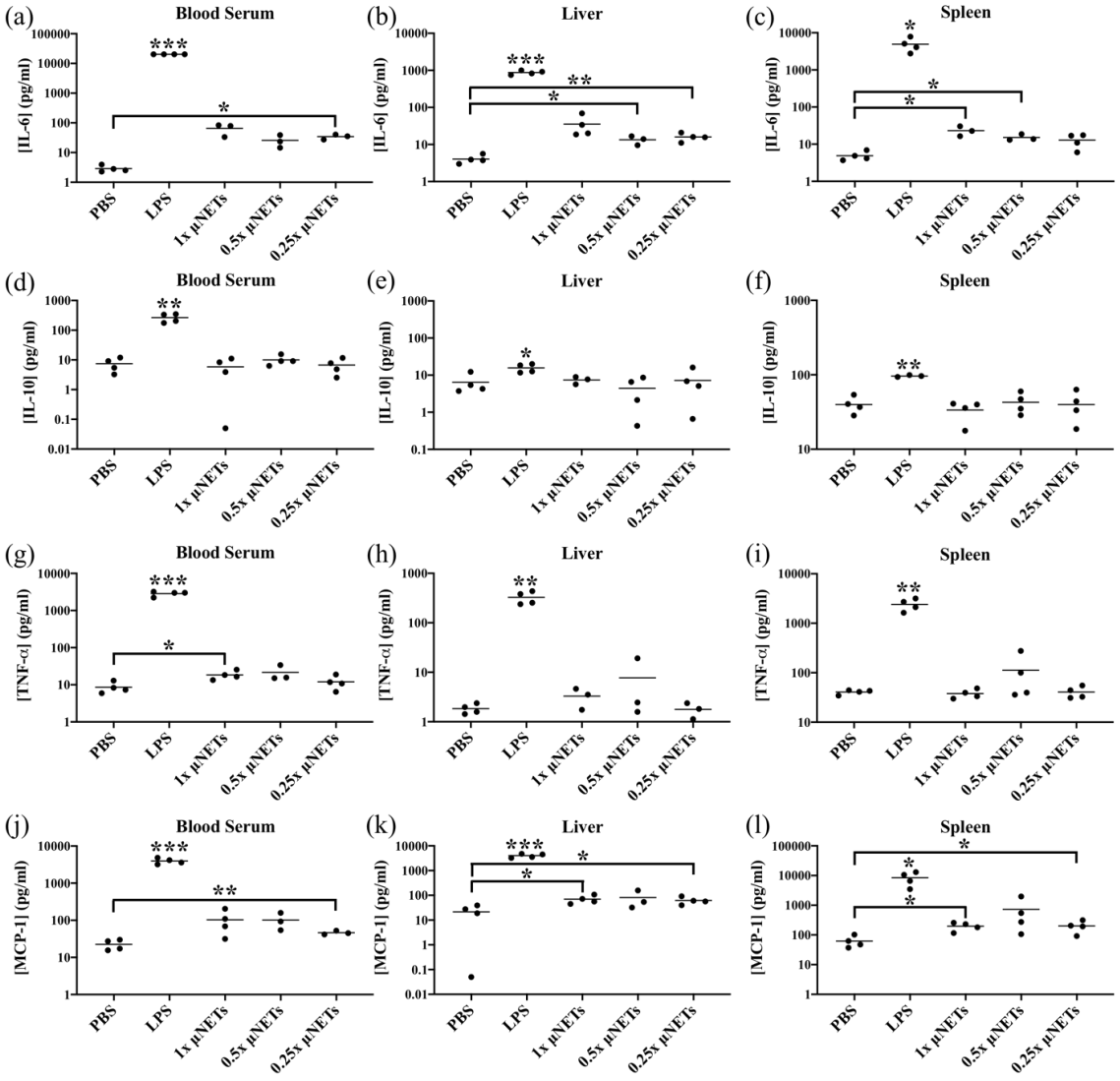

Figure 6. Effects of μNETs dose on cytokines production at two hours post tail vein injection. Concentration measurements (as represented by dots) for (a-c) IL-6, (d-f) IL-10, (g-i) TNF-α, and (j-l) MCP-1 in the blood serum, liver, and spleen, respectively, are shown with the population mean (horizontal bars). PBS and LPS correspond to negative and positive controls, respectively. Statistical significance of * ($p < 0.05$), ** ($p < 0.01$), and ***($p < 0.001$) are indicated. Significance markings directly above LPS indicate that the measured cytokines in response to LPS injection are significantly different with respect to the values for other injected agents at the indicated significance level. Brackets with asterisks above them indicate statistically significance between the shown pairs.

other nNETs doses, these results may be due to variability among the animals response rather than suggesting a dose-dependent IL-10 response.

Although all doses of nNETs induced significantly lower mean values of TNF-α compared to LPS in blood serum, liver, and spleen, there did appear to be some dose sensitivity (Figures 7g-i). Specifically, the 1x nNETs induced significantly higher mean concentration of TNF-α as compared to 0.5x nNETs, 0.25x nNETs, and PBS injections in blood serum, liver, and spleen. In addition, the 0.5x nNETs also induced a higher mean concentration of TNF-α than PBS in blood serum, liver, and spleen, while the 0.25x dose did not. These results suggest that higher doses of nNETs lead to higher concentrations of TNF-α; however, even the highest investigated dose of nNETs did not induce a TNF-α response comparable to that of LPS.

While the 1x nNETs did not induce a significantly lower mean concentration of MCP-1 in blood serum compared to LPS, it neither induced a significantly higher level compared to PBS (Figure 7j). Based on the results of the F-tests, the variances in MCP-1 induced concentrations in response to injection of LPS and all doses of nNETs were significantly higher as compared to the variance associated with PBS injection in blood serum, liver, and spleen ($p < 0.05$). The variance in MCP-1 concentrations for the 1x nNETs in the blood serum was also significantly higher than the variances associated with injection of the other doses of nNETs ($p < 0.05$).

All doses of nNETs induced significantly higher mean concentrations of MCP-1 as compared to PBS in liver and spleen. However, those levels were still significantly lower than the corresponding levels in response to LPS injection (Figures 7k, l). There was a

dose-dependency effect where 1x nNETs injection resulted in a significantly higher mean concentration level of MCP-1 in liver as compared to the 0.5x and 0.25x nNETs injections (Figure 7k), and the 1x and 0.5x nNETs resulting in higher MCP-1 concentrations in spleen as compared to 0.25x nNETs (Figure 7l).

3.4.3 *Time-Dependency of Cytokines Response*

We used the 1x dose of μNETs and nNETs to investigate the dynamics of the induced concentration levels of IL-6, IL-10, TNF-α, and MCP-1 over a six-hour time interval following injection. We chose the 1x dose of NETs for this study since in general it resulted in the greatest levels of the cytokines at 2 hours post-injection for both μNETs and nNETs. IL-12p70 and IFN-γ were not investigated further since, for the most part, none of the investigated doses of μNETs and nNETs investigated resulted in significantly elevated concentrations of these two cytokines (data not shown).

For μNETs, the induced mean concentrations of IL-6, IL-10, TNF-α, and MCP-1 in blood serum did not significantly change over the time course of 2-6 hours post-injection (Figure 8). When compared to the cytokine levels produced in response to PBS injection, only the TNF-α mean concentration levels induced by the μNETs were significantly higher at 2 and 6 hours after injection (Figure 8c).

The response to the nNETs injection was more varied among the animals. The only significant difference in the induced cytokine response was for TNF-α whose mean concentration was significantly higher at 2 hours compared to 6 hours post-injection ($p < 0.01$) (Figure 8c). Similar to the μNETs, the mean induced concentration of TNF-α in

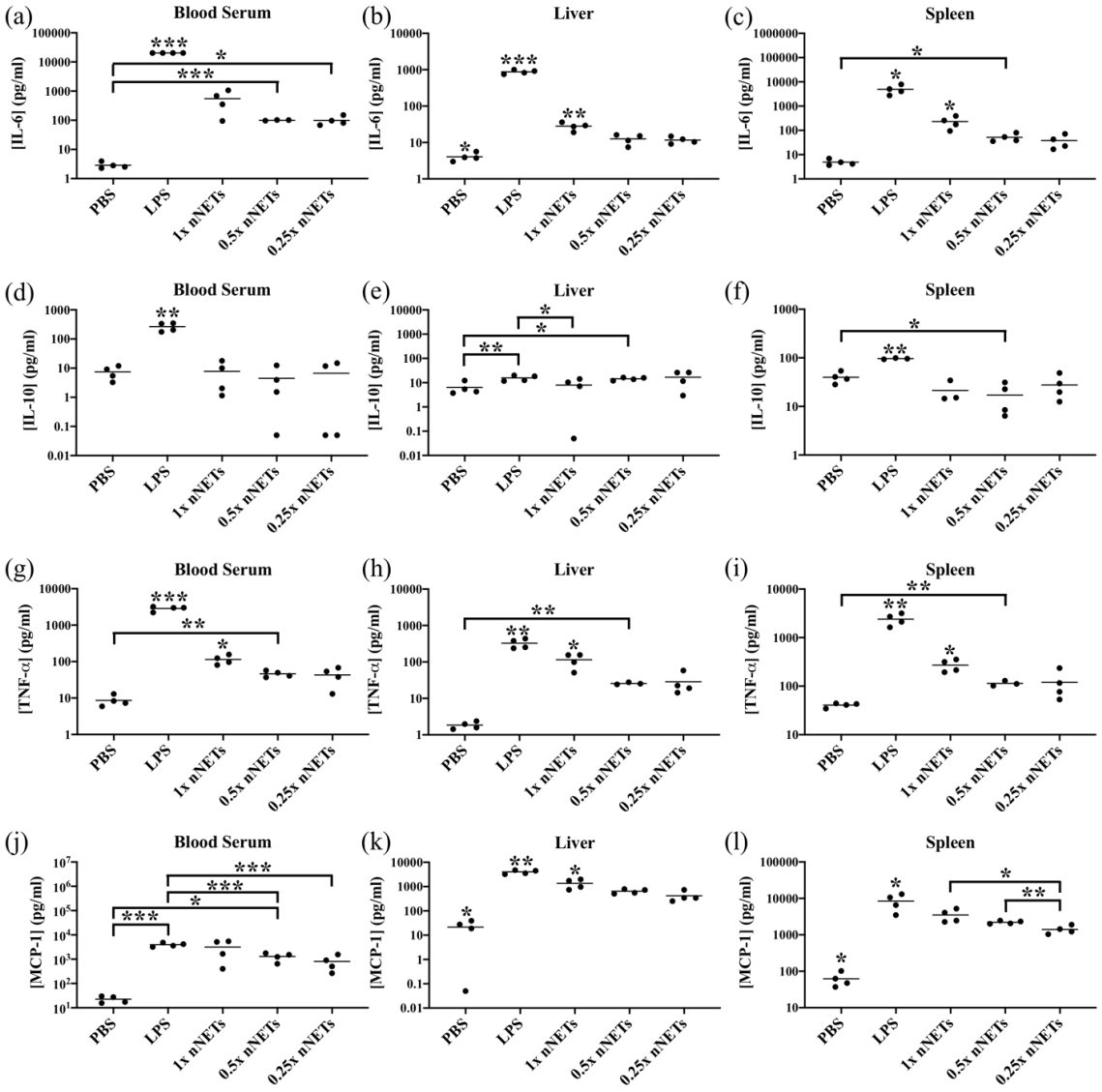

Figure 7. Effects of nNETs dose on cytokines production at two hours post tail vein injection. Cytokine concentration measurements (as represented by dots) for (a-c) IL-6, (d-f) IL-10, (g-i) TNF-α, and (j-l) MCP-1 in the blood serum, liver, and spleen, respectively, are shown with the population mean (horizontal bars). PBS and LPS correspond to negative and positive controls, respectively. Statistical significance of * ($p < 0.05$), ** ($p < 0.01$), and ***($p < 0.001$) are indicated. Significance markings directly above a given agent indicate that the mean value for that agent is significantly different from all other agents at the indicated significance level. Brackets with asterisks above them indicate statistically significance between the shown pairs.

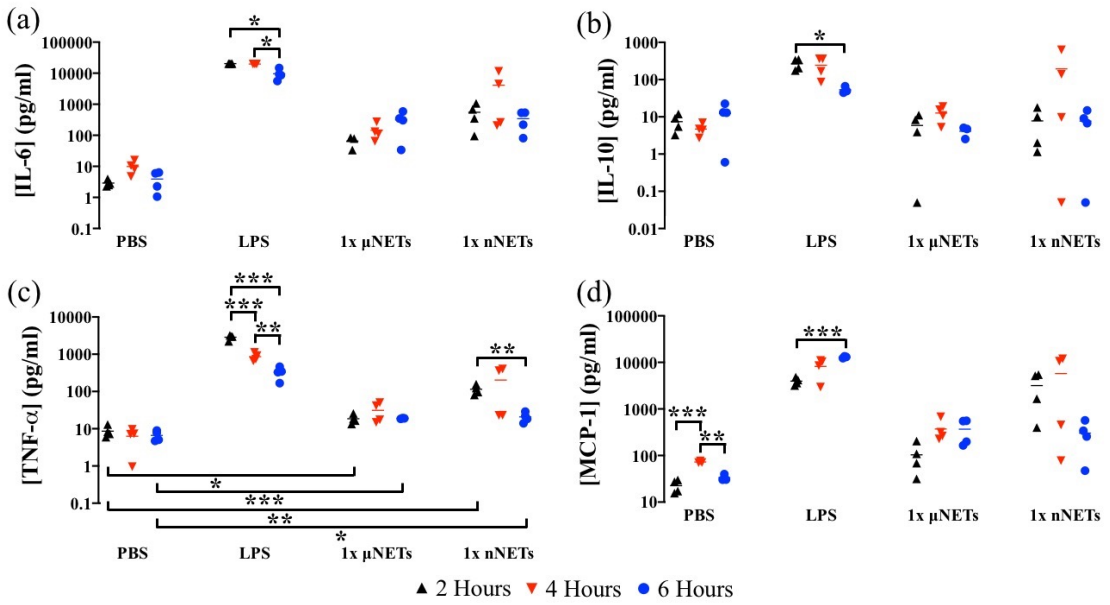

Figure 8. Concentration of cytokines in blood serum at 2, 4, and 6 hours post-injection of PBS, LPS, 1x µNETs, and 1x nNETs. Concentration measurements (as represented by symbols) for (a) IL-6, (b) IL-10, (c) TNF-α, and (d) MCP-1 are shown with the population mean (horizontal bars). Statistical significance of * ($p < 0.05$), ** ($p < 0.01$), and ***($p < 0.001$) are indicated. Brackets with asterisks above them indicate statistically significant differences between the shown pairs.

response to nNETs at 2 and 6 hours post-injection were higher as compared to the levels induced by PBS injection (Figure 8c). None of the other cytokines had induced mean concentration levels that were significantly different from those of PBS at any of the investigated time points.

Mean values of µNETs-induced concentrations of IL-6 and IL-10 in liver at 2, 4, and 6 hours post-injection were not significantly different from each other (Figures 9a, b). Although, the µNETs-induced levels of IL-6 were only significantly higher than those in response to PBS at 4 and 6 hours post-injection, IL-10 induced levels were not significantly different from PBS at any of the time points.

Induced mean concentrations of TNF-α at 4 and 6 hours post-injection of μNETs, while not significantly different from each other, were significantly greater than the value at 2 hours ($p < 0.05$) (Figure 9c). At 2 and 6 hours post-injection, there were no significant differences between the mean concentration of TNF-α induced by the μNETs and the concentration induced by PBS, but at 4 hours post-injection, the μNETs induced levels of TNF-α were significantly higher than the level induced by PBS. We observed a similar trend for the μNETs-induced concentrations of MCP-1, where the mean values of the induced concentrations at 4 and 6 hours were significantly higher than the mean concentration at 2 hours ($p < 0.05$) (Figure 9d). In addition, while the MCP-1 concentration induced by the μNETs was significantly higher than the concentration induced by PBS for all three time points, they were still significantly lower than the concentrations induced by LPS for all three time points.

For the nNETs, we observed a similar trend for the induced cytokine dynamics in the liver. Specifically, there were no statistically significant differences between the concentrations of IL-6 and IL-10 induced by the various doses of nNETs at any of the time points (Figures 9a, b). Although, the mean concentration of nNETs-induced IL-6 concentration at 4 hours did not have a statistically significant higher value than those at 2 and 6 hours, there was also a significantly higher variance in the measured concentration at 4 hours as compared to those at 2 and 6 hours ($p < 0.05$). The nNETs induced levels of IL-6 were only significantly higher than those induced by PBS 2 and 6 hours post-injection. However, there were no significant differences between the nNETs and PBS induced IL-10 levels at any of the time points.

Similar to the results shown in Figure 8, the wide range in IL-6, TNF-α, and MCP-1 concentration in liver at 4 hours is possibly due to the variability in response to nNETs injection among the animals (Figures 9a, c, d). Mean concentrations of TNF-α and MCP-1 in liver at 2 hours were significantly higher than the corresponding concentrations at 6 hours post-injection (Figures 9c, d). However, the mean concentrations of these two cytokines at 4 hours were not significantly different from those at 2 and 6 hours. In addition, nNETs-induced mean concentration of TNF-α and MCP-1 were only significantly higher than those in response to PBS at the 2 hours post-injection timepoint.

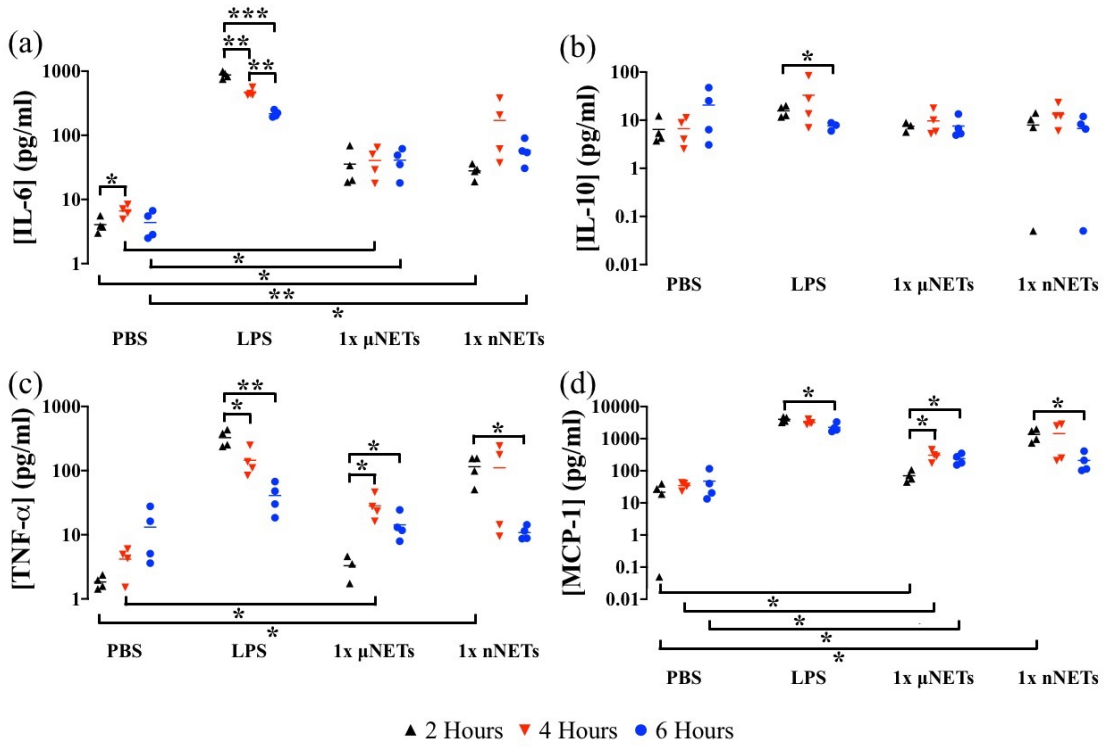

Figure 9. Concentration of cytokines in liver at 2, 4, and 6 hours post-injection of PBS, LPS, 1x µNETs, and 1x nNETs. Concentration measurements (as represented by symbols) for (a) IL-6, (b) IL-10, (c) TNF-α, and (d) MCP-1 are shown with the population mean (horizontal bars). Statistical significance of * ($p < 0.05$), ** ($p < 0.01$), and ***($p < 0.001$) are indicated. Brackets with asterisks above them indicate statistically significant differences between the shown pairs.

In response to injection of 1x μNETs and 1x nNETs, there were no statistically significant changes in the induced concentrations of IL-6 and IL-10 in spleen at 2, 4, and 6 hours ($p > 0.05$) (Figures 10a, b). While there were no significant differences between the IL-10 levels induced by the μNETs and PBS at any of the time points, there were significantly higher levels of IL-6 at 2 and 6 hours post-injection of μNETs as compared to PBS. There were no significant differences at 4 hours post-injection between the IL-6 levels induced by PBS and the μNETs. Furthermore, the μNETs induced levels of IL-6 were significantly lower than the levels induced by LPS for all three time points.

For 1x μNETs, there were no significant differences in the mean concentration of TNF-α in spleen at 2, 4, and 6 hours ($p > 0.05$) (Figure 10c). In addition, there were no statistically significant differences between the TNF-α induced concentrations by PBS and the μNETs at any of the time points. The 1x μNETs-induced mean concentrations of MCP-1 in spleen at 4 and 6 hours were significantly higher than the mean concentration at 2 hours ($p < 0.05$) (Figure 10d). Additionally, the MCP-1 concentrations induced by the μNETs were significantly higher than those by PBS for all three time points. However, the 1x μNETs-induced mean concentrations of TNF-α and MCP-1 still remained significantly lower than the LPS-induced concentrations at all three measurement time points (Figures 10c, d).

Mean values of IL-6 and TNF-α concentrations in response to nNETs were only significantly higher at 2 hours post-injection as compared to the respective values induced by PBS (Figures 10a, c). There were no statistically significant differences in the mean

values of IL-10 in response to nNETs at any of the time points as compared to those in response to PBS (Figure 10b). Mean MCP-1 concentrations induced by the nNETs were significantly higher than those associated with PBS at 2 and 6 hours post-injection, but not at 4 hours post-injection (Figure 10d), possibly due to the variability of response among the animals injected with nNETs. Both TNF-α and MCP-1 mean concentration levels in spleen at 6 hours were significantly lower than their respective concentrations at 2 hours (Figures 10c, d). However, the mean concentrations of these two cytokines at 4 hours were not significantly different from their respective concentrations at 2 and 6 hours.

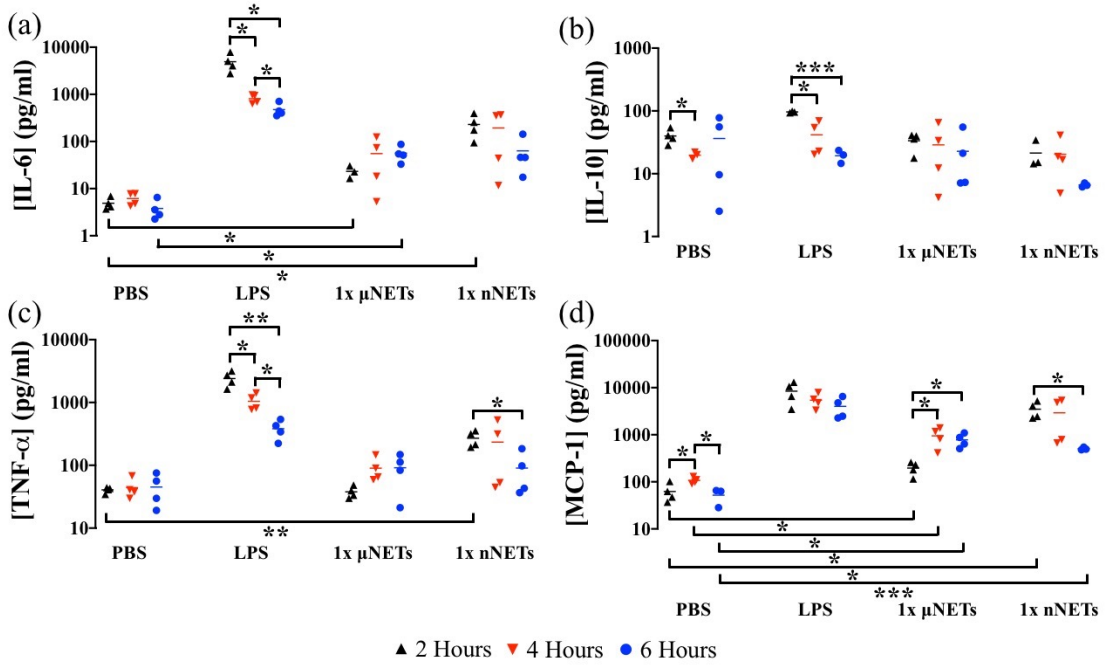

Figure 10. Concentration of cytokines in spleen at 2, 4, and 6 hours post-injection of PBS, LPS, 1x µNETs, and 1x nNETs. Concentration measurements (as represented by symbols) of (a) IL-6, (b) IL-10, (c) TNF-α, and (d) MCP-1 are shown with the population mean (horizontal bars). Statistical significance of * ($p < 0.05$), ** ($p < 0.01$), and ***($p < 0.001$) are indicated. Brackets with asterisks above them indicate statistically significant differences between the shown pairs.

3.4.4 *Effects of nNETs Functionalization with Folate or Herceptin®*

We chose to investigate the effects of functionalization on the acute-phase response at 4 hours post-injection of functionalized nNETs since at the 6-hour time point, concentrations of TNF-α (Figures 8c, 9c, 10c) had significantly decreased as compared to the 2-hour time points. Based on the amounts of folate or Herceptin® used in this study, there was a general trend in reduction of the induced IL-6 (Figures 11a-c) and MCP-1 (Figures 11j-l) concentrations in blood serum, liver, and spleen in response to injection of 1x FF-nNETs or 1x HF-nNETs as compared to the levels resulting from the injection of 1x nNETs. There was also a similar trend for IL-10 (Figure 11d) and TNF-α (Figure 11g) concentrations in blood serum following the injection of 1x FF-nNETs or 1x HF-nNETs.

3.4.5 *Effect of Dual Injections of NETs One Week Apart*

Since the single 1x dose of the nNETs resulted in elevated levels of some of the investigated cytokines at 2 hours post-injection, we aimed to investigate the effects of a dual injection of a lower dose (0.5x), which we had found to be less immunogenic (e.g., Figure 7l) when administered at a single dose. Overall there were no statistically significant differences between the induced cytokine levels in response to either a single injection or dual injections one week apart to either 0.5x μNETs or 0.5x nNETs (Figure 12). The only exception was that there was a significantly higher concentration of IL-10 in the spleen after the second injection of the 0.5x nNETs (Figure 12f). We summarize our key findings associated with each of the immunogenic studies in Table 3.

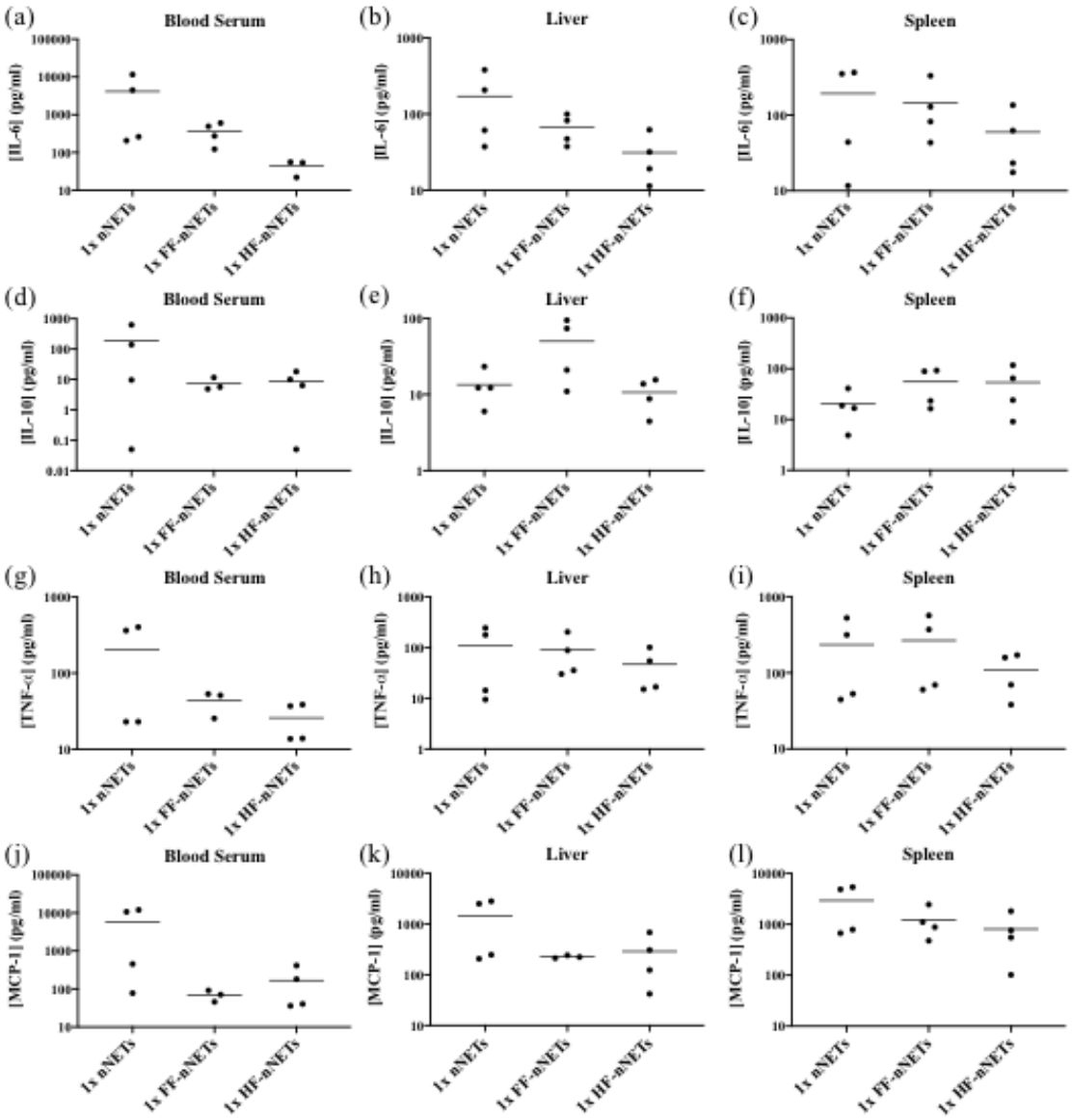

Figure 11. Concentration of cytokines at 4 hours post-injection of 1x nNETs, 1x FF-nNETs, and 1x HF-nNETs. Concentration measurements (represented as dots) for (a-c) IL-6, (d-f) IL-10, (g-i) TNF-α, and (j-l) MCP-1 in the blood serum, liver, and spleen, respectively, are presented. Horizontal bars represent the mean values associated with a given cytokine concentration.

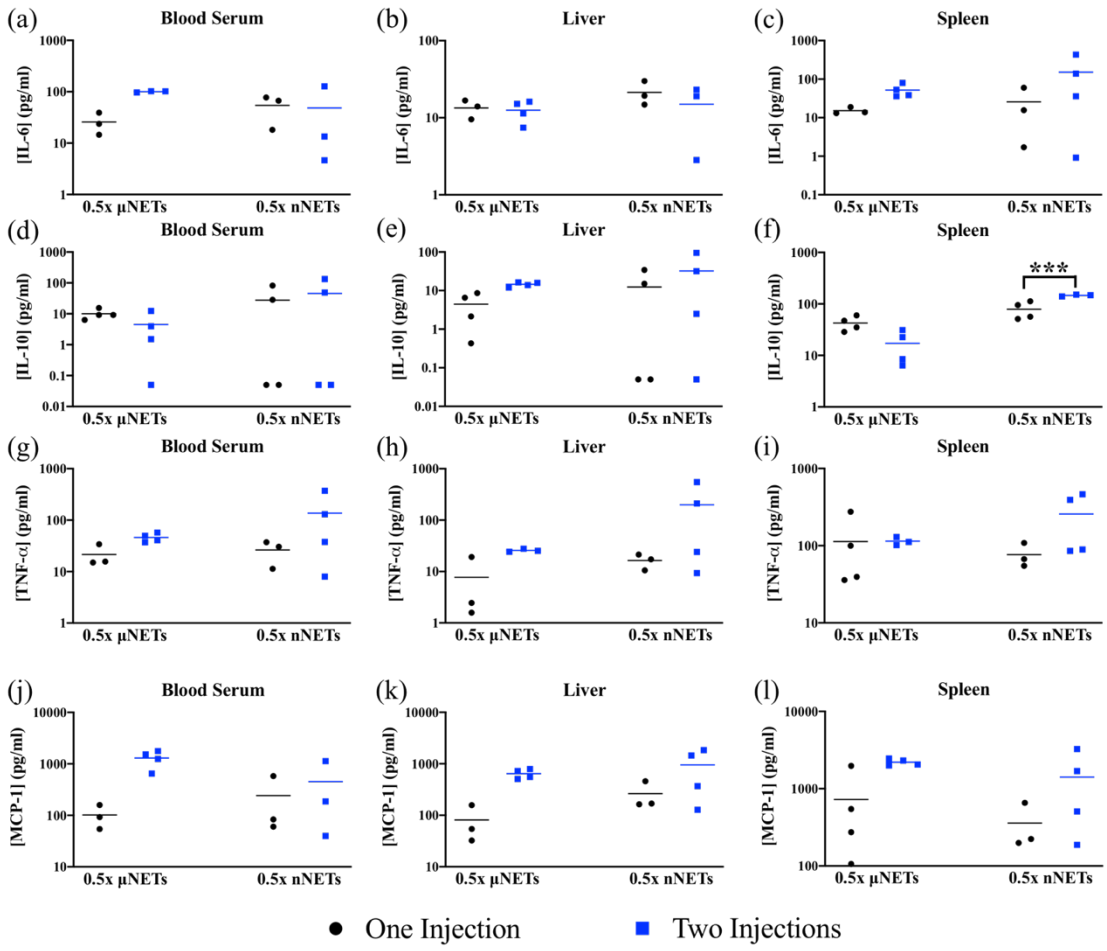

Figure 12. Effect of dual injections of 0.5x µNETs and 0.5x nNETs one week apart. Cytokine measurements were made using samples collected two hours post the second injection. Concentration measurements (represented as symbols) for (a-c) IL-6, (d-f) IL-10, (g-i) TNF-α, and (j-l) MCP-1 in the blood serum, liver, and spleen, respectively, are presented. Horizontal bars represent the mean values associated with a given cytokine concentration. Bracket with *** asterisks above it indicates statistically significant differences between the shown pairs ($p < 0.001$). None of the other t-tests resulted in statistically significant p-values. Therefore, statistical significances of $p < 0.05$ and $p < 0.01$ are not indicated.

Table 3. Key findings associated with the acute immunogenicity studies.

Immunogenicity Study	Key Findings
Effect of Particle Size and Dose	• Mean concentrations of IL-6, IL-10, TNF-α , and MCP-1 in blood serum, liver, and spleen were significantly lower than the corresponding LPS-induced concentrations at all investigated µNETs relative doses. • Although there were some increases in the mean concentrations of IL-6, IL-10, TNF-α , and MCP-1 relative to those induced by PBS, in general they did not appear to correlate with the investigated µNETs doses, possibly due to the variabilities in response among animals. • Mean concentrations of IL-6 in blood serum, liver, and spleen in response to the investigated nNETs doses were significantly below LPS-induced concentrations. • 1x nNETs induced significantly higher concentrations of TNF-α as compared to 0.5x nNETs and 0.25x nNETs in blood serum, liver, and spleen. • All investigated nNETs doses induced significantly higher concentrations of MCP-1 in liver and spleen as compared to PBS.
Time-Dependent Cytokine Response	• Mean concentrations of IL-6 and IL-10 in blood serum, liver, and spleen did not significantly change at 2, 4, and 6 hours post-injection of either 1x µNETs or 1x nNETs. • Mean concentrations of TNF-α and MCP-1 in blood serum did not significantly change at 2, 4, and 6 hours post-injection of 1x µNETs. • Mean concentrations of TNF-α and MCP-1 in liver were significantly higher at 4 and 6 hours post-injection of 1x µNETs as compared to their corresponding values at 2 hours. • Mean concentration of MCP-1 in spleen at 4 and 6 hours post-injection of 1x µNETs was significantly higher than its respective concentration at 2 hours, and at all three time points the 1x µNETs induced significantly higher levels of MCP-1 as compared to PBS. • Mean concentrations of TNF-α in blood serum, liver, and spleen at 6 hours post-injection of 1x nNETs were significantly lower than their respective concentrations at 2 hours. • Mean concentrations of MCP-1 in liver and spleen at 6 hours post-injection of 1x nNETs were significantly lower than their respective concentrations at 2 hours, but not significantly different from PBS-induced MCP-1 concentration in liver at 6 hours.
Effects of nNETs Functionalization with Folate or Herceptin®	• Functionalization of nNETs was associated with a general trend in reduction of IL-6 and MCP-1 concentrations in blood serum, liver, and spleen, and TNF-α and IL-10 concentration reduction in blood serum.
Effects of Dual Injections One Week Apart	• With the exception of IL-10 in spleen in response to nNETs, the second injection of 0.5x µNETs or 0.5x nNETs did not result in statistically significant changes in concentrations of other cytokines as compared to a single injection.

3.5 Discussion

We have focused our studies to the acute-phase of the innate immune response. For the effects of particle size and dose experiments, we chose to investigate the cytokine concentrations at 2 hours post-injection since we were interested to know if the acute response could be elicited within a relatively short time period (e.g., 2 hours). Cytokines (e.g., IL-6, TNF-α) expressions in response to LPS have been shown to peak in blood serum between 1 and 3 hours.[166] We note that the initial phase of the innate response (prior to the acute-phase) is primarily due to the complement system of plasma proteins that act immediately to target the foreign materials (e.g., micro-and nano-particles in blood) for direct lysis, or facilitating their phagocytosis or an inflammatory response by the sensor cells of the innate immune system.[168] Our findings that there were some cytokines activity suggests the continued innate response, requiring the involvement of cytokines to augment the actions of the complement system. Other examples of the interplay between the complement system activation and cytokines activity include C5a and C3a-mediated production of TNF-α by macrophages,[169,170] and the reciprocal action of pro-inflammatory cytokines in amplification of complement system activity.[171]

Macrophages and neutrophils are major inflammatory sensor cells equipped with innate pattern recognition receptors that stimulate phagocytic responses to engulf and destroy foreign materials. Whereas neutrophils extravasate out of the blood vessels to enter an inflamed tissue, macrophages reside in almost all tissues, and are particularly found in key filtration organs, such as the liver, spleen, and the lungs, where they perform phagocytic functions.[172] In our previous study, we found that about 20%, and 5% of

administered μNETs were found in the spleen and liver of healthy SW mice at 6 hours post tail vein injection, respectively.[73] For nNETs, the respective percentages in spleen and liver were about 25% and 13% at 6 hours post tail-vein injection. Spleen is the filtration organ involved in removal of senescent or damaged red blood cells (RBCs) from circulation by red pulp resident macrophages.[173] Hence, in this study, we particularly assayed for the presence of cytokines in spleen and liver.

Phagocytic sensor cells can also secrete cytokines, small proteins (about 25 kDa), to mediate an inflammatory response. Cytokines can either act as synergists or antagonists with one another,[174–176] and are considered as some of the biomarkers in assessing the immunogenicity of various nanoparticles.[174] They can act as pro-inflammatory cytokines, which lead to an immune response, or anti-inflammatory cytokines, which serve to counteract and control inflammation responses.[176,177]

IL-6 is a pleiotropic cytokine with both pro- and anti-inflammatory roles, promptly produced by various cells such as endothelial cells, monocytes, mesenchymal cells as well as immune cells including macrophages.[176,178] In the initial stages of an inflammatory response, it moves from the bloodstream to the liver where it acts on hepatocytes to synthesize and secrete acute-phase proteins with broad specificity for pathogen-associated molecular patterns into blood.[179] Our results show that as early as two hours post-tail vein injection of μNETs and nNETs, IL-6 levels in general were elevated, and in some cases significantly higher than the levels induced by PBS injection (although still at significantly lower levels than those induced by LPS) (Figures 6a-c, 7a-c). Elevated levels of IL-6 in blood serum may have been due to production by monocytes.[178] Mean concentrations of

IL-6 in blood serum, liver, and spleen at 6 hours were not significantly different than those at 2 hours post-injection of either 1x μNETs or 1x nNETs (Figures 8a, 9a, 10a).

TNF-α is a pro-inflammatory cytokine produced by activated macrophages.[175,180] It has a range of biological activities, and is also involved in the initiation of the acute-phase response. TNF-α is a potent activator of endothelial cells, causing expression of blood clotting proteins, and increased vascular permeability. There was a dose-dependency effect where 1x nNETs induced a significantly higher concentration of TNF-α as compared to 0.5x nNETs and 0.25x nNETs in blood serum, liver, and spleen at two hours post-injection (Figures 7g-i). At 6 hours post-injection of 1x nNETs, mean concentrations of TNF-α became significantly lower in blood serum, liver, and spleen as compared to the respective mean concentrations at 2 hours (Figures 8c, 9c, 10c).

IL-10 is a potent anti-inflammatory cytokine that can be produced by various cell types including monocytes, macrophages, and dendritic cells (DCs).[175,176,181] Its main effects are to suppress macrophage and DC functions by deactivating their cytokine synthesis.[176,181–183] In general, the μNETs- and nNETs-induced levels of IL-10 were not significantly different from those induced by PBS in blood serum, liver, and spleen (Figures 6d-f, 7d-f, respectively). In addition, mean concentrations of IL-10 in blood serum, liver, and spleen did not change significantly when comparing any of the time points post-injection of either 1x μNETs or 1x nNETs (Figures 8b, 9b, 10b).

Chemokines are chemoattractant cytokines released during the earliest phases of infection, inducing directed chemotaxis of neutrophils, monocytes, and other effector cells of innate immunity from blood into sites of infection.[184] MCP-1 (also designated as CCL2)

is a member of the CC group of chemokines produced by a variety of cell types including fibroblasts and endothelial cells, but with monocytes and macrophages as the primary sources.[163,185] It is a potent attractant of monocytes, inducing their migration from the bloodstream to become tissue macrophages.[163,186] There was a general trend that injection of μNETs and nNETs at 1x dose led to elevated levels of MCP-1 as early as two hours post-tail vein injection (Figures 6j-l, 7j-l). Additionally, all investigated doses of nNETs induced significantly higher concentrations of MCP-1 in liver, and spleen as compared to PBS (Figures 7k,l). While the mean concentration of MCP-1 in spleen at 6 hours post-injection of 1x μNETs was significantly higher than its respective concentrations at 2 hours, the trend was reversed in response to injection of 1x nNETs (Figure 10d).

Overall, it appears that nano-sized NETs were associated with higher induced concentrations of IL-6, TNF-α, and MCP-1 (Figures 6,7) as compared to those induced by micro-sized NETs. Since μNETs and nNETs had similar zeta potentials, it is unlikely that the zeta potential had a major role in modulating the immune response to μNETs and nNETs. It has been suggested that the toxicity of nanoparticles can result from their increased surface-to-volume ratio, giving rise to a greater proportion of reactive surface molecules to be displayed on the surface compared to interior molecules.[187] Consistent with this explanation, nNETs would present a larger fraction of potentially immunogenic surface molecules that can be recognized by the inflammatory sensor cells. In addition, conformational changes to some of the immunomodulatory surface proteins during the fabrication process of nNETs (e.g., formed by extrusion of micro-sized EGs) may result in our observed cytokine levels. For example, CD47, a transmembrane glycoprotein on RBCs

impedes phagocytosis through an inhibitory interaction with the signal-regulatory protein-alpha (SIRP-α) expressed on macrophages of the reticuloendothelial system.[34,188] However, conformational changes in CD47 can switch its role from an inhibitory to an activating molecule, leading to phagocytosis of RBCs.[189] It is possible that mechanically-induced conformation changes to CD47 (e.g., through mechanical extrusion of EGs) would lead to a more efficient phagocytosis of nNETs and possibly enhanced secretion of specific cytokines by phagocytic sensor cells.

There was a general trend in reduction of IL-6, TNF-α, and MCP-1 by functionalizing the nNETs with folate or Herceptin® (Figure 11). Our functionalization method involved the use of a DSPE-PEG linker inserted into the lipid phase of the particles. Abrams et al reported that several cytokines including IL-6 and TNF-α were released into the plasma of mice in which lipid nanoparticles were administered.[190] It is possible that functionalization of nNETs based on DSPE-PEG lipid insertion was effective in camouflaging the lipid phase of the particles from recognition by the inflammatory sensor cells to ultimately reduce the released levels of IL-6, TNF-α, and MCP-1. It is also possible that the detection capability of the inflammatory sensor cells were reduced due to induced steric hindrance effects resulting from the presence of folate or Herceptin® conjugated onto nNETs.

The second injection of either μNETs or nNETs at 0.5x, one week after their respective first injection, in some cases resulted in elevation of some of the cytokines, although the differences were not statistically significant ($p > 0.05$) (Figure 12) (with the exception of IL-10 in the spleen after the second injection of 0.5x nNETs). Despite this

finding, the role of the adaptive immune system in generating immunological memory needs to be further investigated.

Other researchers have also investigated the immunogenicity of erythrocyte-based constructs. For example, Luk et al have reported that injection of RBC-cloaked nanoparticles loaded with doxorubicin in C57BL/6 mice did not result in a significant increase in levels of IL-6 in blood serum 6 hours post-injection.[191] He el al show that injection of 2D $MoSe_2$ nanosheets camouflaged with RBC membranes did not induce elevated levels of IL-6, IL-12, or TNF-α in the serum of SD mice 24-72 hours post injection compared to mice injected with saline.[51] Similarly, Sun et al report that Chlorin e6 imbedded erythrocyte membrane vesicles containing Prussian blue nanoparticles did not induce elevated levels of TNF-α in the blood serum of KM mice 1-7 days post-injection as compared to PBS control group.[85] While our results indicate some elevated levels of inflammatory cytokines during the acute-phase (studies over 2-6 hours), these other studies suggest that any cytokine elevation due to RBC derived constructs would return to baseline levels within 24 hours, and remain stable for up to 7 days post-injection.

Since our endotoxin assessment of μNETs and nNETs showed some endotoxic activity above those for the standard samples (Figure 13), it is possible that the elevations in some of the cytokine level measurements may have a component due to endotoxins, possibly introduced during the fabrication process. If this is the case, then some of the measured cytokine levels may actually over-estimate the acute-phase response. In some cases, the mean cytokine (TNF-α) levels due to 0.5x and 0.25x μNETs (Figure 6g) and 0.25x nNETs (Figure 7g) were not significantly different than that induced by PBS, and

comparable to the reported value of ≈ 68 pg/ml reported by Sun et al.,[85] indicating the absence of an immune response due to NETs-based endotoxicity. Nevertheless, it is important that for ultimate clinical translation, the processes for particles fabrication and quality control are made in compliance with good manufacturing practice (GMP) guidelines.

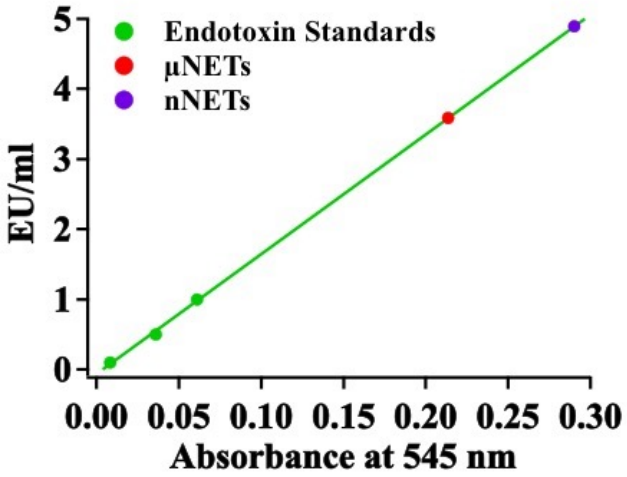

Figure 13. Endotoxin levels for three standard samples, μNETs, and nNETs. The straight line is the calibration curve fitting the standard measurements. Samples of μNETs and nNETs were diluted 1:100 prior to the measurements.

While cytokines are important biomarkers in evaluating the immunogenicity of particle-based delivery systems such as NETs, additional biomarkers for comprehensive immunotoxicity evaluation include blood chemistry, hematology, and histology.[192] Our results from a previous study show that the levels of biomarker enzymes alanine aminotransferase and aspartate aminotransferase, associated with liver, and creatinine and urea nitrogen, associated with kidney functions were not altered in a statistically significant manner at 24 hours post injection of μNETs or nNETs in healthy SW mice.[73] Values of

RBC count, mean corpuscular volume, hemoglobin, and % hematocrit were not altered in response to injection of μNETs or nNETs. Similarly, histological sections of liver, spleen, lung, heart, and kidney did not show any pathological alterations. These results are consistent with those reported by Luk et al where RBC count, platelet count, hemoglobin, and % hematocrit were not significantly different from those of mice injected with a sucrose solution,[191] as well as those by Rao et al where the nanoparticles did not induce hepatic or renal toxicity.[140] While in this study, we have focused on the acute-phase of the innate immune response, understanding of the complete immune response including the roles of the complement system as well as the adaptive immune response in generating long-term immunological memory associated with repeated administration of these particles, and the interplay between innate and adaptive immunity are needed.

3.6 Conclusions

We have evaluated the acute-phase of the innate immune response to NETs in healthy Swiss Webster (SW) mice following tail vein injection. In particular, we found that both 1x μNETs and 1x nNETs resulted in statistically significant higher levels of TNF-α in blood serum at 2 and 6 hours post-injection as compared to the levels associated with PBS treatment at these times. Cytokines response to 1x nNETs at 2 hours also included significantly higher levels of IL-6 in liver and spleen, TNF-α in blood serum, liver, and spleen, and MCP-1 in liver and spleen as compared to PBS-induced levels. Functionalization of nNETs with folate or Herceptin® was associated with a general trend in reduction of IL-6 and MCP-1 concentrations in blood serum, liver, and spleen, and TNF-

α and IL-10 concentration reduction in blood serum. With the exception of IL-10 in spleen in response to nNETs, the second injection of μNETs and nNETs at 0.5x did not lead to significantly higher concentrations of other cytokines as compared to a single injection. Future studies are needed to evaluate the roles of the complement system and adaptive immunity in response to these particles.

Chapter 4: Functionalized Erythrocyte-Derived Optical Nanoparticles to Target Ephrin-B2 Ligands

4.1 Abstract

Over- or under-expression of Erythropoietin-production human hepatocellular receptors (Eph) and their ligands are associated with various diseases. Therefore, these molecular biomarkers can potentially be used as binding targets for the delivery of therapeutic and/or imaging agents to cells characterized by such irregular expressions. We have engineered nanoparticles, derived from erythrocytes and doped with the near infrared (NIR) FDA-approved dye, indocyanine green (ICG). We refer to these nanoparticles as NIR erythrocyte-derived transducers (NETs). Herein, we functionalized the NETs with the ligand binding domain of a particular Eph receptor, EphB1, to target the genetically modified human dermal microvascular endothelial cells (hDMVECs) with co-expression of EphB1 receptor and its ligand ephrin-B2. This cell model mimics the pathological phenotypes of lesional endothelial cells (ECs) in Port Wine Stains (PWSs). Our quantitative fluorescence imaging results demonstrate that such functionalized NETs bind to the ephrin-B2 ligands on these hDMVECs in a dose-dependent manner that varies sigmoidally with the number density of the particles. These nanoparticles may potentially serve as agents to target PWS lesional ECs and other diseases characterized with over-expression of Eph receptors or their associated ligands to mediate phototherapy.

4.2 Introduction

Erythropoietin-production human hepatocellular (Eph) receptors are the most abundant subgroup of receptor tyrosine kinases, with at least sixteen different receptors being expressed in humans.[193] These receptors are divided into two subclasses based largely on their binding affinities for the two subclasses of ephrin ligands (ephrin-A or ephrin-B), and are referred to as EphA or EphB receptors.[193–197] EphA receptors tend to bind ephrin-A ligands; while EphB receptors preferentially bind to ephrin-B ligands.[193–197] These receptors and ligands are involved in a number of physiological processes involving the development of the nervous system, angiogenesis, and cell migration.[195,196,198,199]

Over- or under-expression of Eph receptors and their ligands have been associated with lung, breast, and prostate cancers, as well as melanomas and leukemia.[200] Some Eph receptors and ephrins have also been reported to play a role in bone homeostasis, and implicated in myeloma bone disease, osteolytic bone disease associated with breast cancer metastasis,[201] and skeletal deformities including cleft palates and craniosynostosis.[202] Deregulation of Eph receptor and ephrin ligand signaling has also been implicated in aberrant synaptic functions associated with neurodegenerative diseases such as Alzheimer's disease.[203] Recently, we found that EphB1 receptors and ephrin-B2 ligands are co-expressed on the lesional endothelial cells (ECs) of in individuals with port wine stains (PWSs).[204]

Due to their abundance on a variety of cell types, Eph receptors and their ligands have become viable targets for therapeutic agents that can be conjugated to various targeting moieties including peptides, antibodies, and the ephrins themselves.[205–212] For

example, Blevins et al. conjugated a peptide that targets EphA2 and EphA4 to a PEG linker and a polymer for the delivery of therapeutic plasmids to the pancreas.[207] Targeting the Eph/ephrin system has also been done by attaching the targeting agent to a variety of nanoparticles. For example, various targeting agents have been conjugated to hollow gold nanospheres, gold-coated silica nanoshells, biosynthesized magnetite nanoparticles, liposomal nanoparticles, and gold nanorods.[206,208–211] In addition to delivering therapeutics, some nanoparticles can deliver imaging and photodynamic therapy agents to specific cells.[205,206,212]

Recently, use of cells such as erythrocytes, or nanoparticles coated with cell membranes as therapeutic or imaging platforms has drawn increased attention.[3,33,35,119,150,213–218] A particular feature of erythrocytes that distinguishes them from other cell types is their naturally long circulation time (≈90-120 days) attributed to the presence of "self-marker" proteins on their surface to inhibit the immune response.[1,4] One putative self-marker is CD47 glycoprotein, which impedes phagocytosis through signaling with phagocytes receptor, SIRPα.[34,219–221] Hence, constructs derived from erythrocytes may provide their cargo available in circulation for prolonged times.[8] For example, Hu et al., reported that polymeric nano-constructs coated with erythrocyte-derived membranes were retained in mouse blood for three days with a circulation half-life of ≈ 8 hours.[213] As constructs that can be engineered autologously (or from similar blood types), erythrocyte-derived particles also present a potentially non-toxic, and biocompatible agent delivery platform.

We provided the first report of erythrocyte-derived nanoparticles doped with the FDA-approved near infrared dye, indocyanine green (ICG).[150] We refer to these constructs as NIR erythrocyte-derived transducers (NETs) since once photo-excited by an appropriate NIR wavelength, ICG can transduce the absorbed light energy to emit fluorescence, generate heat, or mediate the production of reactive oxygen species.[30] We have previously demonstrated the effectiveness of antibody-functionalized NETs in targeted imaging of ovarian cancer cells, as well as NETs functionalized with tissue plasminogen activator as a theranostic agent for NIR fluorescence imaging and thrombolysis of blood clots *in vitro*.[33,35]

Herein we report for the first time the engineering of NETs functionalized with the ligand binding domain (LBD) of the EphB1 receptor (Figure 14). We chose the LBD of the EphB1 receptor as the targeting agent since it has a strong binding affinity for the ephrin-B2 ligand.[195] We demonstrate the effectiveness of such functionalized NETs (F-NETs) in targeting endothelial cells that over-express the ephrin-B2 ligand by fluorescence imaging. These optical constructs can potentially be useful to target the ephrin-B2 ligand on a variety of diseases ranging from cancer cells to PWS ECs.

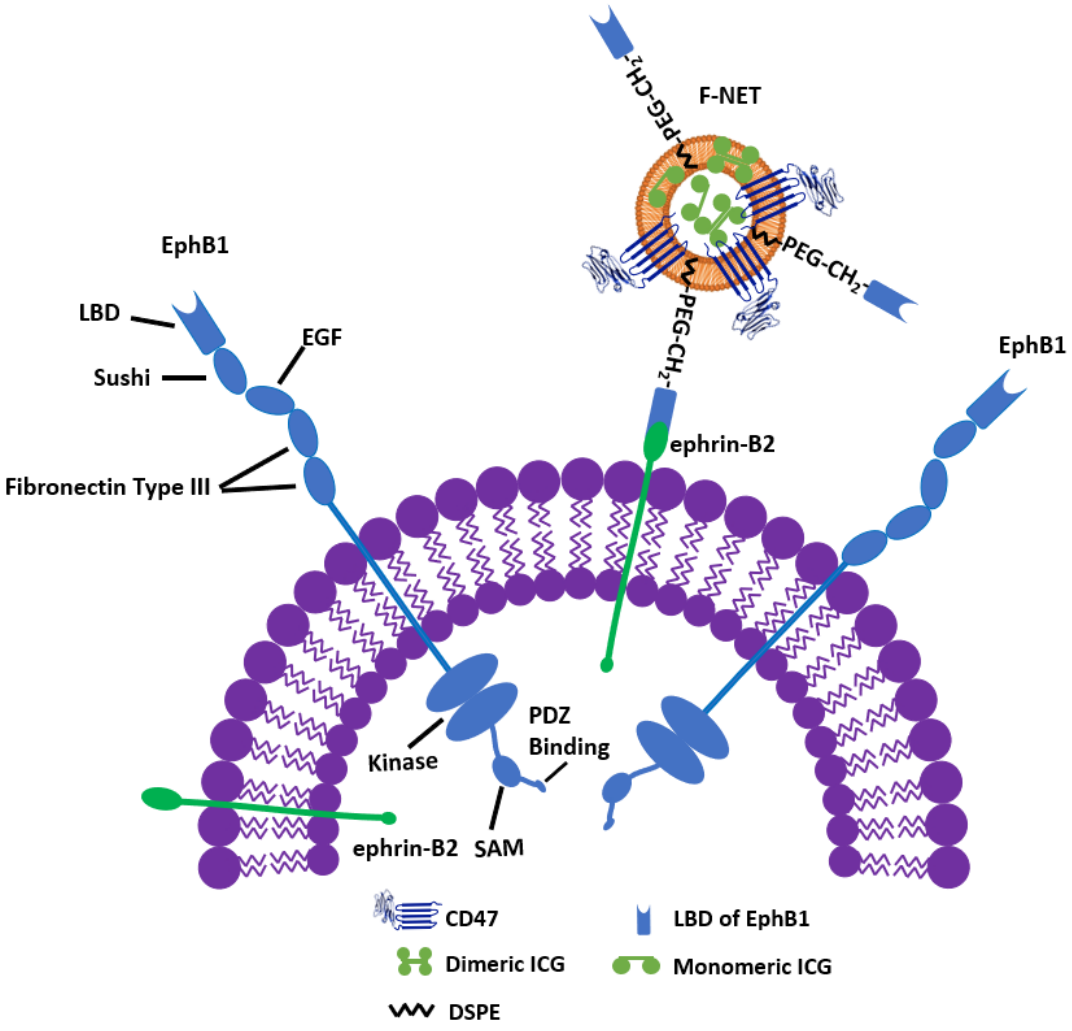

Figure 14. Schematic of a PWS EC that co-expresses the EphB1 receptor and ephrin-B2 ligand. F-NETs are functionalized with the LBD of EphB1 to selectively bind to ephrin-B2.

4.3 Materials and Methods

4.3.1 *Fabrication of NETs and F-NETs*

Erythrocytes were isolated from either bovine or human whole blood (Rockland Immunochemicals, Inc. and Innovative Research, Inc. respectively) via centrifugation

(1000 x g for 5-10 minutes at 4°C). The plasma and buffy coat were removed, and the erythrocyte pellet was re-suspended in ≈ 320 mOsm phosphate buffered saline (PBS) (defined as 1xPBS). Erythrocytes were centrifuged (1000 x g for 5-10 minutes at 4°C) and washed with 1xPBS three times with the supernatant discarded after each wash. The erythrocyte pellet was then subjected to hypotonic treatment by re-suspension in 0.25xPBS (≈ 80 mOsm) for ≈10 minutes followed by centrifugation (20,000 x g for 20 minutes at 4°C). The supernatant containing hemoglobin was discarded, and the hypotonic treatment was repeated until the erythrocyte pellet was opaque, indicating the formation of erythrocyte ghosts (EGs).

To form non-functionalized NETs, EGs were extruded sequentially through 400 nm and 200 nm polycarbonate porous membranes (VWR, Inc.) using an Avanti mini extruder (Avanti Polar Lipids, Inc.), resulting in nano-sized EGs (nEGs). These nEGs were then suspended in a solution made of equal volumes of 1xPBS, 0.1 M Sϕrenson's buffer (Na_2HPO_4/NaH_2PO_4, 140 mOsm, pH ≈ 8), and ICG solution (Fisher Scientific Company). Concentration of ICG in the loading buffer solution was either 25 μM or 33.33 μM, depending on the experiment. The solution was then centrifuged (≈ 56, 000 x g for 1 hour at 4°C) and the supernatant was removed. The pellet, comprised of NETs, was then re-suspended in 1xPBS, centrifuged, and washed two times. NETs were re-suspended in 1xPBS for experiments.

To fabricate F-NETs, we proceeded as follows. EGs (as prepared above) were centrifuged (20,000 x g for 15 minutes at 4°C) and the supernatant was discarded (Figure

15). We made a solution consisting of 5 mg of a linker, 1,2-distearoyl-sn-glycero-3-phosphoethanolamine-polyethylene glycol-aldehyde (DSPE-PEG-CHO) (2000 Da PEG) (Nanocs, Inc.) dissolved in 1 ml nanopure water. We added 20 μl of this lipid linker solution to 1 ml of EGs in nanopore water and let the solution incubate (30 minutes at room temperature). The resulting lipid-inserted EGs were then filtered through 50k Amicon Ultra-4 centrifuge filter units (Millipore) via centrifugation (≈ 1,700 x g for 10-15 minutes at room temperature) to remove excess linker. As excess lipid-linker and nanopore water were removed through the filter units, the lipid-inserted EGs remained suspended in solution by replenishing with 1xPBS. Lipid-inserted EGs were then extruded, and then loaded with either 25 μM or 33.33 μM ICG in the loading buffer (as described above). The resulting NETs with lipid-inserted linker were re-suspended in 1xPBS and incubated with 10 μg/ml Recombinant Rat EphB1 Fc Chimera Protein, Cf (R&D Systems, Inc.) (hereafter referred to as the EphB1 LBD) for five minutes at room temperature in the dark. This chimera protein is composed of the extracellular LBD of rat EphB1, a short polypeptide sequence, and human IgG_1. We added 5 μl of 20 mM sodium dithionite, as the reducing agent, to the solution containing the NETs with lipid-inserted linkers, and incubated for one hour at 4 °C in the dark. The amine group on the C-terminus end of the EphB1 LBD protein serves as the site for covalent coupling with the aldehyde group on the end of the lipid linker, induced by reductive amination reaction. During this reaction, the Schiff base formed at the site of covalent coupling is reduced by the sodium dithionite, irreversibly converting the imine to a more stable amine. This reaction results in covalent attachment of the EphB1 LBD to NETs. The resulting pellet, comprised of F-NETs, was then washed

in 1xPBS and centrifuged as described above before being re-suspended in 1xPBS (Figure 15).

4.3.2 *Dynamic light scattering-based measurements of particle diameters*

Hydrodynamic diameters of NETs and F-NETs suspended in 1xPBS were measured by dynamic light scattering (DLS) (Zetasizer Nanoseries, NanoZS90, Malvern Instruments). All measurements were made with the particle suspensions in polystyrene cuvettes with a 1 cm pathlength. Measurements were collected three times for each sample, and averaged to calculate the mean diameter and standard deviation (SD) for each population sample. The percentage of each sample's population associated with a given diameter was plotted, and data were fit with a Lognormal function using Igor.

4.3.3 *Absorption and fluorescence spectra of NETs and F-NETs*

Absorption spectra of NETs and F-NETs suspended in 1xPBS were recorded in the 280-1000 nm spectral range using a UV Visible spectrophotometer (Cary 50 UV-Vis spectrophotometer, Agilent Technologies) with an optical path length of 1 cm. Both NETs and F-NETs were fabricated using 25 μM ICG in the loading buffer. Suspensions of NETs or F-NETs, diluted to have absorbance values of one at 800 nm, were designated to have the relative number density (N^*) of 1x when suspended in 1xPBS. To obtain solutions with a lower N^*, the nanoparticle solutions were diluted by increasing the volume of 1xPBS as desired. To obtain solutions with a higher N^*, the nanoparticle solutions were concentrated using less 1xPBS as desired. We prepared solutions of NETs and F-NETs with N^* ranging

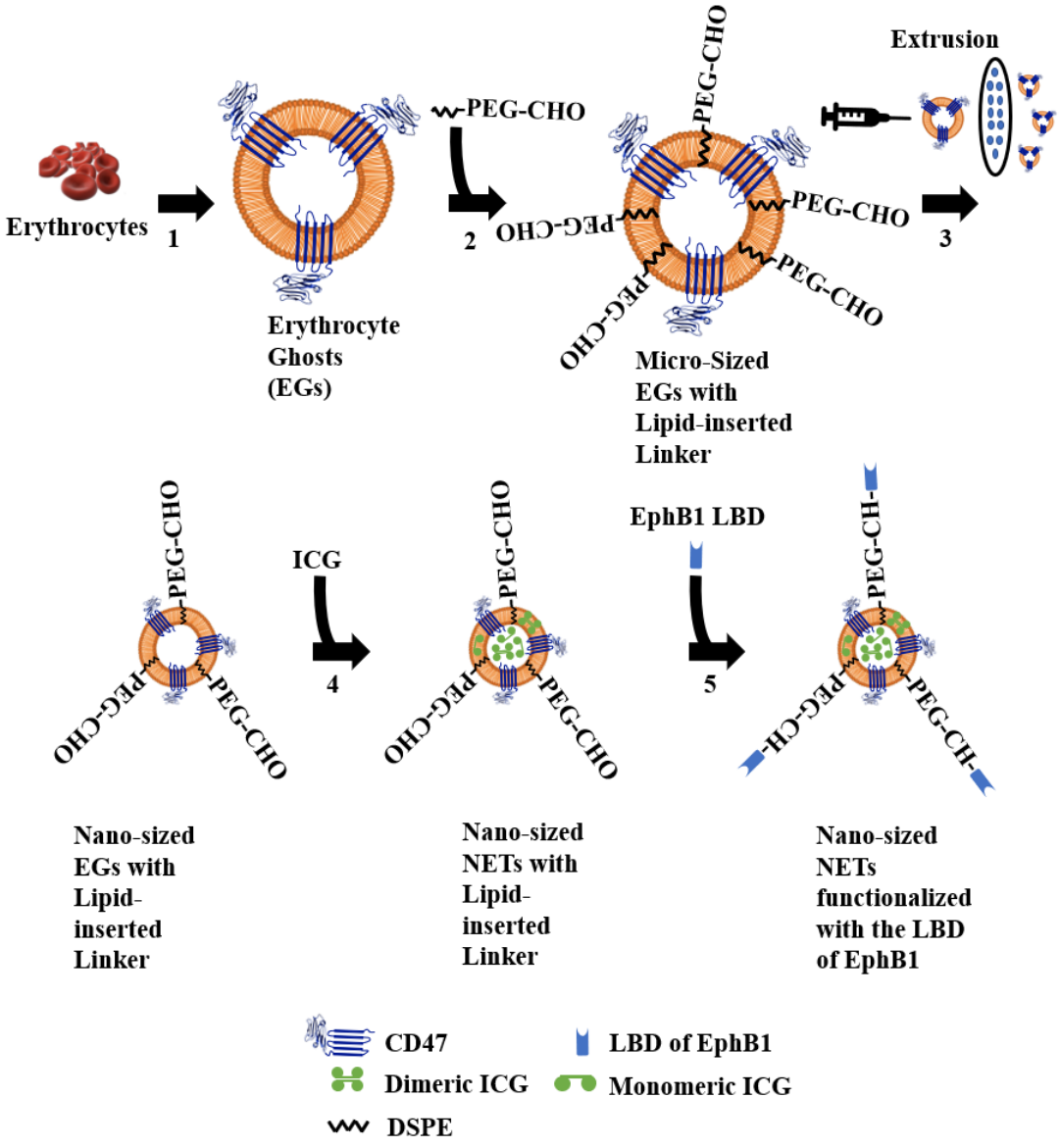

Figure 15. Schematic of steps to fabricate F-NETs. 1. Erythrocyte ghosts (EGs) were formed by depleting the hemoglobin content of erythrocytes. 2. EGs were incubated with a DSPE-PEG-CHO linker for insertion into the lipid phase of EG's shell. 3. Micron-sized EGs (μEGs) with lipid-inserted linkers were extruded to make linker bearing nano-sized EGs (nEGs). A zoomed-in cross-section of the extruder filters with nano-sized pores for extrusion of μEGs into nEGs is shown. 4. nEGs with lipid-inserted linkers were loaded with ICG in a hypotonic solution resulting in formation of nano-sized NETs containing lipid-inserted linkers. 5. The EphB1 LBD was covalently attached to the terminal end of lipid-inserted linkers using a reductive amination reaction to functionalize the NETs. For illustration purposes we also show one of the erythrocyte membrane proteins, CD47.

from 0.25x (lowest relative number density of nanoparticles) to 2x (highest relative number density of nanoparticles) for various experiments.

Fluorescence spectra of NETs and F-Nets suspended in 1xPBS in response to photo-excitation at 720 ± 2.5 nm with a 450W xenon lamp were acquired using a fluorometer (Fluorolog-3 spectrofluorometer, Edison). We normalized the wavelength (λ)-dependent fluorescence emission χ(λ) as follows:

$$\chi(\lambda) = \frac{F(\lambda)}{1 - 10^{-A(\lambda_{ex})}} \qquad (1)$$

where F is the fluorescence emission intensity in response to photo-excitation at a given λ, and $A(\lambda_{ex})$ is the absorbance of the sample at the excitation wavelength. For this characterization, both sets of NETs and F-NETs were fabricated using 33.33 μM ICG in the loading buffer.

4.3.4 *Functionalization validation*

We validated the functionalization of NETs with the LBD of the EphB1 receptor by using immunofluorescent staining. Specifically, NETs (control) and F-NETs were fabricated using 33.33 μM ICG in the loading buffer, and incubated with 10 μl human IgG Fc Phycoerythrin (PE)-conjugated antibodies (R&D Systems, Inc.) per one ml of NETs or F-NETs solution for one hour at room temperature in the dark. These antibodies bind to the human IgG_1 portion of the EphB1 LBD. Nanoparticles were centrifuged and washed in 1xPBS three times and then photo-excited at 488 ± 2.5 nm (450W xenon lamp) to elicit

emission from the PE. The resulting fluorescence emission spectra were recorded and normalized as described above.

4.3.5 *Human dermal microvascular endothelial cell culture and transfection*

Human dermal microvascular endothelial cells (hDMVECs) were cultured in Endothelial Cell Basal Medium (ECBM) with growth supplement (Cell Applications, Inc.) as previously described.[204] In order to establish the EC models with co-expression of EphB1 receptors and ephrin-B2 ligands, which mimic the pathological phenotypes of PWS ECs, we isolated a subset of normal hDMVECs with high expression of surface EphB1 receptors via biotinylated chimera ephrin-B2-Fc, which contains the extracellular portion of ephrin-B2 ligands and is capable of binding to EphB1 receptors, and streptavidin-conjugated magnetic beads. The rationale of this selection is that the ephrin-B2-Fc chimera ligand binds to $EphB1^+/EphB4^+$ expressing venous hDMVEC subpopulation, while the remaining arterial hDMVEC subpopulation ($EphB1^-/EphB4^-$) express ephrin-B2 ligands.

Specifically, 100 μg of the streptavidin-conjugated magnetic beads were incubated with 2 μg of biotinylated chimera ephrin-B2 Fc at room temperature for 15 minutes before the ephrin-B2 Fc-magnetic bead complex was removed from solution via magnetic strands. The bead complex was then incubated with $\approx 5x10^5$ hDMVECs on ice for 30 minutes. The cells that bound to the bead complex were isolated and designated as $EphB1^+$/ephrin-$B2^-$ hDMVECs, which have previously been verified to express the EphB2 receptor, with undetectable ephrin-B2 levels.[204]

Lentiviral vector pLX304-EphrinB2 containing human ephrin-B2 cDNA was obtained from DNASU (Clone ID: HsCD00446022). Control lentiviral vector pLIM1-EGFP (enhanced green fluorescent protein) was obtained from Addgene (Plasmid ID: 19319). The third generation lentiviral packaging plasmids were used to produce pLX304-EphrinB2 and pLIM1-EGFP lentiviruses in Phoenix cells. The ephrin-B2 selected hDMVEC subpopulation showed a higher level of EphB1 mRNA and a much lower level of ephrin-B2 mRNA as compared to non-selected heterogeneous hDMVEC populations.[204] $EphB1^{+}$/ephrin-$B2^{-}$ hDMVECs were infected by either lentiviruses containing EGFP ($EGFP^{+}$/$EphB1^{+}$/ephrin-$B2^{-}$ hDMVECs) (referred to as control cells) or human EphrinB2 cDNA to over-express ephrin-B2 ($EphB1^{+}$/ephrin-$B2^{+}$ hDMVECs) (referred to as ephrin-B2 cells). The cells were continuously cultured for two weeks to allow the expression of transgenes for the F-NETs experiments. The ephrin-B2 expression in the hDMVECs was determined by Western blot assay, as we previously described. Beta-actin was used as the internal loading control.[204]

4.3.6 *Targeting Ephrin-B2 ligands by F-NETs*

To determine the effectiveness of the F-NETs to target the ephrin-B2 ligand, we incubated the control and ephrin-B2 cells with either NETs or F-NETs for 40 minutes at 4°C in the dark. The incubating solution consisted of 50% human ECBM containing 10% fetal bovine serum (FBS) by volume, with the nanoparticles in 1xPBS forming the other 50%. Both NETs and F-NETs were fabricated using 33.33 μM ICG in the loading buffer solution. The

relative number density of the particles (ρ^*) in 1xPBS and ECBM with 10% FBS cell media was defined as:

$$\rho^* = \frac{N^* V_{nanoparticles}}{V_{nanoparticles} + V_{ECMB}} \qquad (2)$$

where $V_{\text{nanoparticle}}$ is the volume of NETs or F-NETs suspension in 1xPBS, and V_{ECBM} is the volume of ECBM and 10% FBS. Cells were incubated with NETs having ρ^* of 0.5x, and F-NETs with ρ^* values ranging from 0.03x to 0.5x.

After incubation, cells were stained with 500 μl of 4',6-diamidino-2-phenylindole (DAPI) (10-11 μM) for subsequent fluorescence microscopy imaging experiments. DAPI fluorescence emission in response to photo-emission at 360 ± 20 nm by a Xenon/Mercury arc lamp (Nikon Eclipse Ti-S microscope with an Osram Sylvania XBO75W/2 bulb, Interlight) was captured by an electron multiplier gained CCD camera (Quant EM-CCD, C9100-14 Hamamatsu) over the spectral band of 435-485 nm. NIR fluorescence emission (>770 nm), emanating from ICG in NETs, was captured in response to photo-excitation at 740 ± 35 nm. We present falsely colored fluorescent images associated with DAPI-stained nuclei (blue channel), and ICG emission (red channel).

4.3.7 *Image analysis*

Acquired NIR fluorescent images of the cells were analyzed using ImageJ software. Regions of interests (ROIs) were selected on a given image. The mean intensity $\bar{I}$ value from a given set of ROIs was calculated as:

$$\bar{I} = \frac{\sum_{l=1}^{m}\left[\sum_{k=1}^{n}\left(\frac{\sum_{j=1}^{p} I_j^{ROI} - I_j^{Background}}{p}\right)\right]}{m*n} \qquad (3)$$

where I_j^{ROI} is the fluorescence emission intensity at the j^{th} pixel in the ROI of a given image, $I_j^{background}$ is the fluorescence emission intensity corresponding to the background region of the same image, p is the total number of pixels in a given ROI, n is the number of ROIs, and m is the number of images obtained from the cell population. Multiple ROIs were selected from a given image, and multiple images from a cell population were used to calculate $\bar{I}$ for each population of cells.

4.4 Results and Discussion

4.4.1 *Hydrodynamic diameter distribution of NETs and F-NETs*

As determined by fitting Lognormal distributions to dynamic light scattering (DLS)-based measurements, the average hydrodynamic diameters ± standard deviation (SD) of non-functionalized NETs and F-NETs were 127.96 ± 1.58 nm and 156.76 ± 2.52 nm, respectively (Figure 16). Our previously published transmission electron and scanning electron microscopic images of NETs have shown that DLS-based measurements of NETs diameter are consistent with those obtained by electron microscopy.[33,150] The increase in the mean diameter of F-NETs by ≈ 28.8 nm suggests that the thickness of the linker and the LBD coated onto the F-NETs was ≈ 14.4 nm. Minelli and Shard measured the thickness

of 2 kDa thiol terminated methoxy PEG coatings on gold nanoparticles to range from ≈ 3-16 nm.[222] The DPSE-PEG-CHO linker used in our functionalization of NETs has a similar structure to the linker used by Minelli and Shard. Therefore, our estimate of the coating thickness is reasonable and consistent with this previous literature.

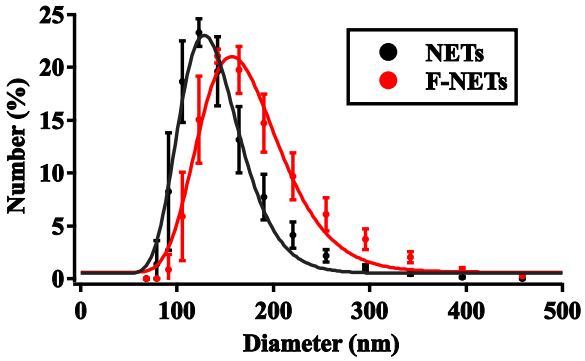

Figure 16. Hydrodynamic diameters of NETs and F-NETs suspensions. Suspensions were in phosphate buffered saline and the hydrodynamic diameters were measured by dynamic light scattering. We present the average (circles) with SD values (error bars) associated with three measurements of a sample. Lognormal distributions are fitted to the measured data (solid traces). Black data points and traces correspond to the NETs population, while the red data points and traces correspond to the F-NETs population.

4.4.2 *Absorption and fluorescence spectra of NETs and F-NETs*

Absorption spectra of NETs and F-NETs suspensions in 1xPBS as a function of the relative number density (N^*) of the particles are presented in Figure 17a and 17b, respectively. Absorption at ≈ 795 nm and ≈ 735 nm correspond to the monomeric and H-like aggregate forms of ICG, respectively.[150,223,224] There was a near linear relationship between the absorbance values at 795 nm and N^*. For example, when N^* was increased to 2x, the absorbance value at 795 nm increased from ≈ 1.0 to ≈ 1.8 for both sets of nanoparticles.

The similar absorbance values at 795 nm for NETs and F-NETs for all N^* values suggests that the loading efficiency of ICG was the same for both sets of nanoparticles.

There was a similar near linear relationship between the absorbance values at 280 nm, the wavelength associated with the protein absorption[225] of NETs, and N^*. For example, when N^* was increased to 2x, the absorbance value at 280 nm increased from ≈ 0.8 to ≈ 1.4 for both sets of nanoparticles. For the same N^*, there were minimal differences between the absorbance values at 280 nm for NETs and F-NETs. This result suggests that for a given N^*, the population of F-NETs and NETs had the same amount of proteins, and the EphB1 LBD did not contribute to the absorbance of F-NETs at 280 nm.

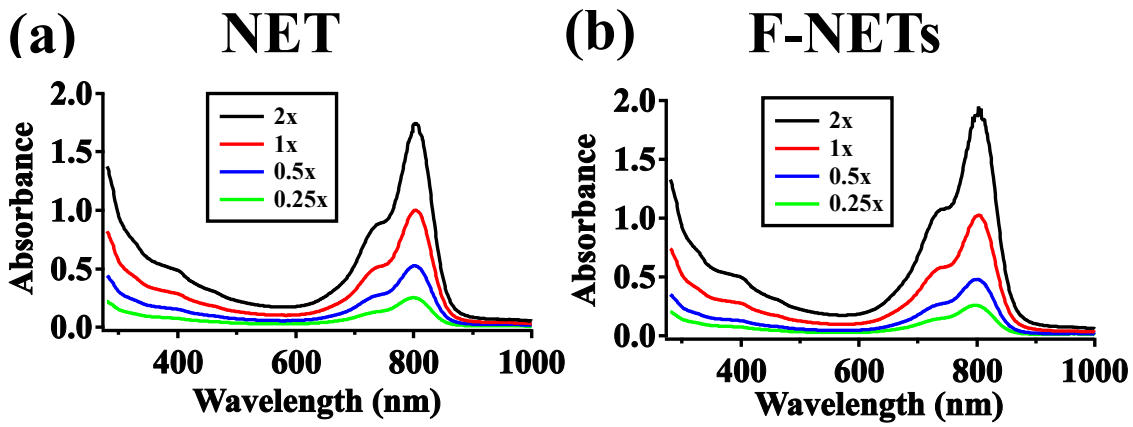

Figure 17. Absorption spectra of NETs and F-NETs. Absorption spectra of: (a) NETs, and (b) F-NETs recorded in 1xPBS for various values of N^* ranging between 0.25-2x. Both NETs and F-NETs were fabricated using 25 μM ICG in the loading buffer.

In response to photo-excitation at 720 ± 2.5 nm, NETs and F-NETs produced nearly identical fluorescence emission spectra in the 735-900 nm band (Figure 18a), associated with the monomer form of ICG.[224] Successful functionalization of NETs with the EphB1 LBD was evidenced by the drastically different fluorescence emission spectrum of F-NETs

over the 550-630 nm spectral band, in response to 488 ± 2.5 nm photo-excitation, as compared to that of the NETs (Figure 18b). This band is associated with the fluorescence emission of the Phycoerythrin (PE) dye[226,227] that was conjugated to the antibodies that bind to the human IgG_1 part of the EphB1 LBD. The emission spectra provide evidence towards successful functionalization of the F-NETs with the EphB1 LBD (Figure 18b), while at the same time demonstrating that the NIR emission characteristics of F-NETs remained unaltered as compared to that of NETs (Figure 18a).

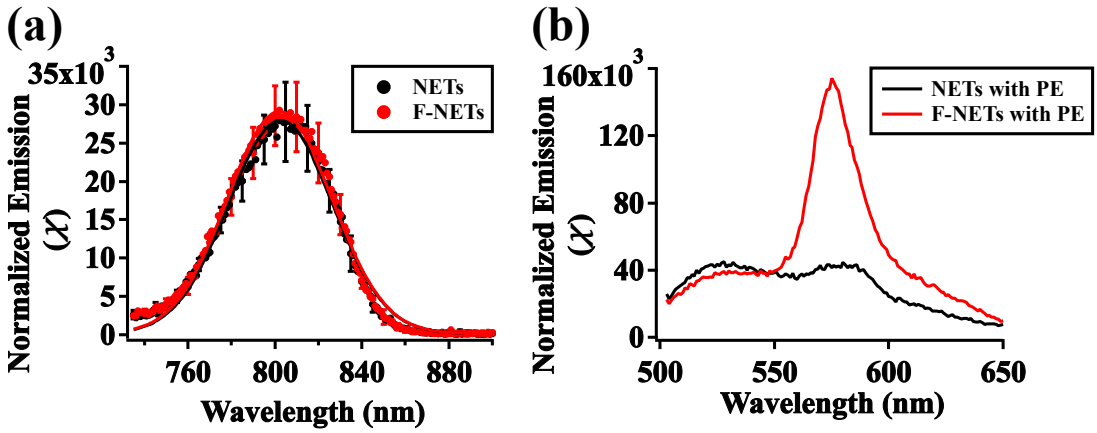

Figure 18. Normalized fluorescence emission spectra of NETs and F-NETs. (a) Normalized fluorescence emission spectra of NETs and F-NETs in response to photo-excitation at 720 ± 2.5 nm. We present the average (circles) with SD values (error bars) associated with four samples. Gaussian functions fit the data (solid traces). (b) Normalized fluorescence emission spectra of non-functionalized NETs and F-NETs after incubation with human PE-labeled IgG Fc antibodies in response to photo-excitation at 488 ± 2.5 nm. All spectral recordings were made with the particles suspended in 1xPBS and $N^* = 1x$. Both NETs and F-NETs were fabricated with 33.33 μM ICG in the loading buffer.

4.4.3 *Targeting Ephrin-B2 ligands by F-NETs*

We verified the expression of ephrin-B2 on hDMVECs using a Western blot (Figure 19). Even when incubated with NETs at the highest ρ^* value (0.5x), there was minimal NIR

fluorescence emission from the control and ephrin-B2 hDMVECs (image not shown), suggesting that non-functionalized NETs were not effectively uptaken by either cell type. We quantified the average NIR emission ($\bar{I}$) using equation 3. There were no statistically significant differences among $\bar{I}$ values for control hDMVECs whether incubated with NETs or F-NETs with a ρ^* value of 0.5x (data not shown), suggesting that both particles were uptaken at about the same levels by the control hDMVECs. These results further suggest that the interaction of control hDMVECs with either NETs or F-NETs is likely due to non-specific binding, with uptake of the particles by clathrin-mediated endocytosis or caveolae-dependent endocytosis.[228]

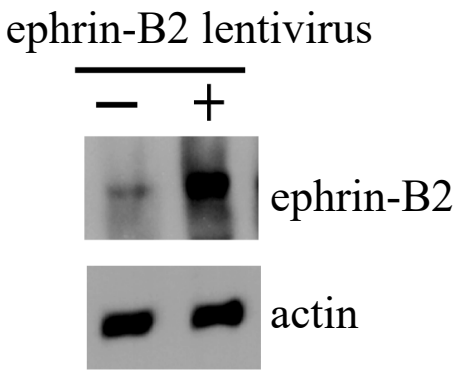

Figure 19. Ephrin-B2 Western blot expression. Western blot showing the expression of ephrin-B2 in hDMVECs infected with an ephrin-B2 lentivirus compared to the ephrin-B2 expression level of hDMVECs not infected with the ephrin-B2 lentivirus. Beta-actin levels are shown as the internal loading control.

There was also minimal NIR fluorescence emission from control hDMVECs after incubation with F-NETs, regardless of the ρ^* value investigated (images not shown). This result suggests that F-NETs were not effective in targeting hDMVECs that lacked the

ephrin-B2 ligand. NIR emission from the ephrin-B2 hDMVECs emerged when the ρ^* value for F-NETs exceeded 0.12x, suggesting that there was a threshold number density of F-NETs for effective targeted imaging of ephrin-B2 hDMVECs (Figure 20a).

As the ρ^* value of F-NETs increased from 0.03x to 0.5x there was no clear trend in $\bar{I}$ values for control hDMVECs (Figure 20b). There were also no statistically significant differences in $\bar{I}$ values associated with control and ephrin-B2 hDMVECs when the ρ^* value of F-NETs was 0.03x or 0.06x. However, for $\rho^* \geq 0.12$x there were statistically significant differences ($p < 0.001$) between the $\bar{I}$ values associated with the control and ephrin-B2 hDMVECs. Specifically, for ephrin-B2 cells, there was a sigmoidal relationship between the $\bar{I}$ values and ρ^* value of F-NETs (Figure 20c). This result suggests that a threshold number density of F-NETs ($\rho^* = 0.12$x) was needed to overcome non-specific binding between F-NETs and ephrin-B2 hDMVECs. Once this threshold value was exceeded, F-NETs occupied almost all the available binding positions on the ephrin-B2 hDMVECs.

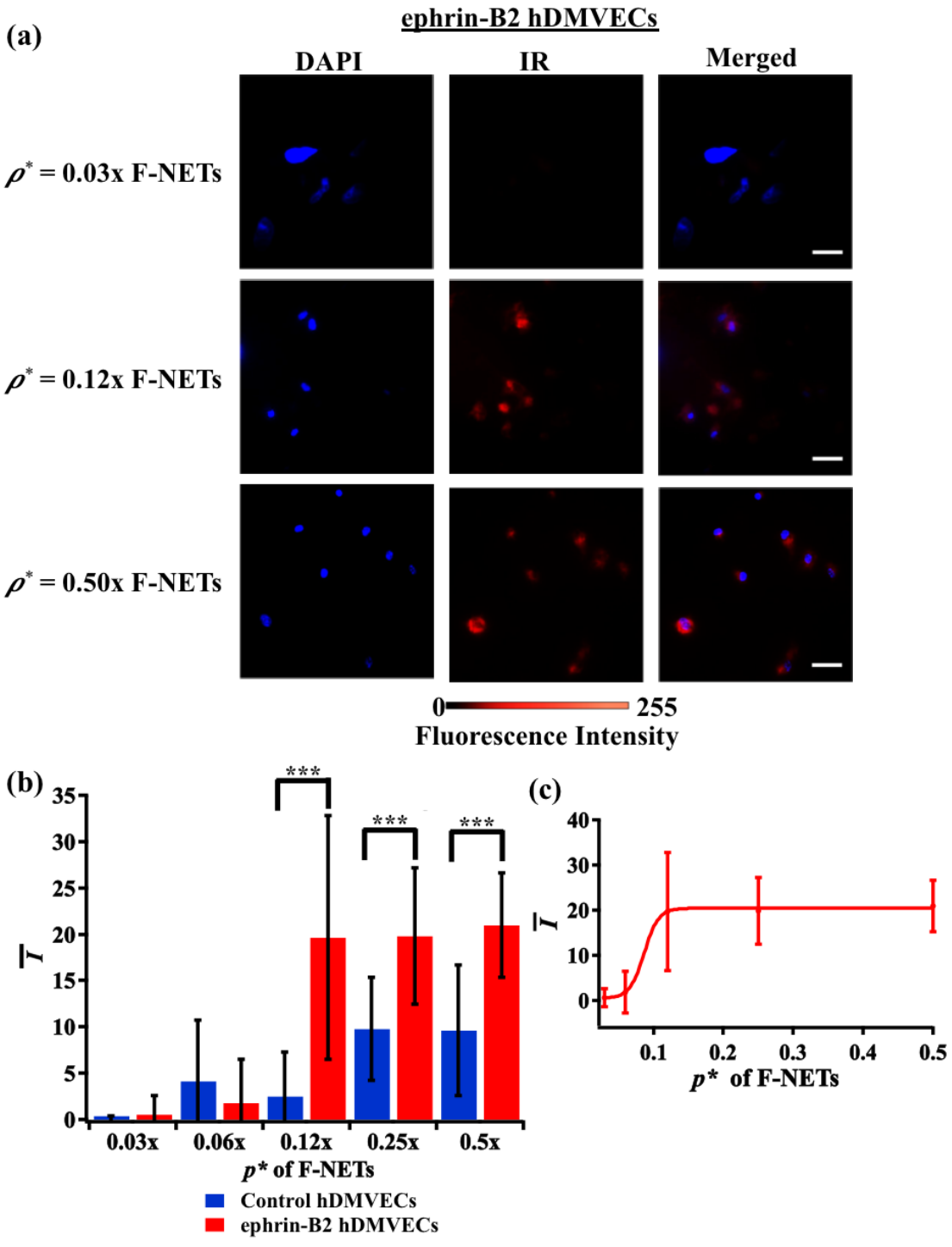
(a)
ephrin-B2 hDMVECs
DAPI
IR
Merged
ρ* = 0.03x F-NETs
ρ* = 0.12x F-NETs
ρ* = 0.50x F-NETs
0
255
Fluorescence Intensity
(b)
***
***
***
35
30
25
20
15
10
5
0
Ī
0.03x
0.06x
0.12x
0.25x
0.5x
p* of F-NETs
Control hDMVECs
ephrin-B2 hDMVECs
(c)
40
30
20
10
0
Ī
0.1
0.2
0.3
0.4
0.5
p* of F-NETs

Figure 20. Cellular fluorescence of control and ephrin-B2 hDMVECs incubated with F-NETs at various ρ^* values. (a) Fluorescent images of control and ephbin-B2 hDMVECs after 40 minutes of incubation at 4°C with F-NETs solutions. All images are falsely colored with the blue and red corresponding to DAPI and ICG NIR emission from the NETs, respectively. Scale bars are 30 μm. (b) Averaged fluorescence intensity ($\bar{I}$) (see equation 3) as a function of ρ^*. Cells from 3-4 images were analyzed, resulting in 16-41 measurements for each combination of nanoparticles and cells. Statistical significance of $p < 0.001$ is denoted by ***. Only statistically significant populations with the same ρ^* value of F-NETs are indicated. (c) Sigmoidal fit to the $\bar{I}$ values of the ephrin-B2 hDMVECs versus the ρ^* value of F-NETs. Error bars in panels (b) and (c) represent standard deviations.

A particular application of F-NETs relates to laser treatment of cutaneous capillary malformations, PWSs. PWSs are currently treated by laser irradiation using visible wavelengths in the range of 585-595 nm. These wavelengths target the endogenous hemoglobin to induce photothermal destruction of the PWS vasculatures.[229] However, the melanin pigment within the melanocytes, located in the basal epidermal layer of skin and residing over the abnormal plexus of dermal blood vessels, has relatively strong optical absorption over the current laser treatment band. For example, at treatment wavelength of 585 nm, the absorption coefficient of a melanosome is comparable to that of oxy-hemoglobin.[230] As such, the photons intended to reach the dermal vasculature would be partially absorbed within the epidermis. The outcome is non-specific thermal injury to the epidermis and insufficient heat generation within the vasculature, leading to an inadequate treatment.

An alternative phototherapeutic approach can potentially be developed by using NIR wavelengths in conjunction with intravascular administration of F-NETs. For example, by changing the treatment wavelength from 585 to 755 nm, nearly threefold reduction in the absorption coefficient of a single melanosome can be achieved.[230] This approach offers several advantages: (1) reduced risk of non-specific thermal injury to the epidermis to potentially allow treatment of individuals with moderate to heavy pigmentation;[31] (2) increased depth of optical penetration to reach deeply-seated blood vessels (e.g., > 500 μm below the skin surface);[31] (3) targeted delivery of F-NETs to the endothelial cells within the PWS vasculature where there is over-expression of ephrin-B2 ligands;[204] and (4) heat generation within the blood vessels resulting from the absorption

of ICG within the F-NETs to induce photothermal destruction of the abnormal vasculature plexus.

4.5 Conclusions

To the best of our knowledge, we have demonstrated for the first time the fabrication of erythrocyte-derived nanoparticles containing ICG, and functionalized with the EphB1 LBD to target cells that express ephrin-B2. Optical absorption and fluorescence characteristics of NETs remain unaltered upon functionalization with EphB1 LBD. Our quantitative imaging fluorescence imaging results suggest that the uptake of such functionalized NETs by ephrin-B2 expressing cells follows a sigmoidal function that depends on the relative number density of F-NETs in the incubating medium.

Chapter 5: EphA2 Receptor Targeting Erythrocyte-Derived Nanoparticles

5.1 Abstract

The over- or under-expression of Erythropoietin-production human hepatocellular receptors (Eph) and their ligands, ephrins, are associated with a number of diseases, including various cancers. We have developed a peptide, referred to as 147B5, capable of selectively targeting and degrading EphA2 receptors. We have demonstrated the successful functionalization of nanoparticles derived from red blood cells (RBCs) with these peptides. As representative payloads the nanoparticles are loaded with the near infrared (NIR) FDA-approved dye indocyanine green and the chemotherapeutic Taxol. We refer to these nanoparticles as 147B5-NIR erythrocyte-derived transducers (147B5-NETs). Spectral measurements confirm the 147B5-NETs are loaded with ICG. In addition, the 147B5-NETs are capable of degrading EphA2 receptors on cancer cells and are uptaken more by EphA2 expressing cancer cells compared to controls. These nanoparticles represent a potential imaging and drug delivery platform for diseases characterized by an over-expression of EphA2 receptors.

5.2 Introduction

Eph receptors are a large subgroup of receptor tyrosine kinases, and together with their ligands, ephrins, they play a large role in cell signaling.[212] Eph receptors and ephrins are highly expressed in the developing nervous system and also play a role in the development of the cardiovascular system.[212] The Eph/ephrin system is involved in a number of developmental processes, and is important for establishing borders between cells of different tissues.[231] In adults Eph receptors and ephrins are important for synaptic plasticity, bone homeostasis, and even insulin secretion.[231] However, the over- or under-expression of Eph receptors and ephrins has been implicated in a number of diseases. They have been linked to neurodegenerative diseases such as Alzheimer's disease,[203] bone remodeling diseases such as osteoporosis,[202] as well as vascular malformations such as Port Wine Stains.[204]

Eph receptors and ephrins have also been shown to play a role in cancer, and have been a number of studies aimed at targeting them as a potential cancer therapy.[232] One Eph receptor of particular interest is EphA2. EphA2 receptors have been shown to be overexpressed in most solid tumors.[233] A number of small peptides and antibodies are being investigated for their ability to target and stimulate EphA2 receptors, leading to their phosphorylation, cell internalization, and subsequent degradation.[234] This EphA2 activation is thought to require receptor dimerization or clustering, therefore more effective targeting agents may be those that are dimers.[205] However, YSA, an apparently monomeric peptide that selectively binds to EphA2, has been shown to induce EphA2 receptor phosphorylation.[235] In addition, when YSA was conjugated to the

chemotherapeutic paclitaxel, it was shown to be more effective at inhibiting prostate cancer tumor growth in a xenograft model compared to paclitaxel alone.[233] Therefore, combining peptides capable of dimerization with chemotherapeutics is a promising platform for more efficacious cancer therapy.

As another potential cancer treatment we have developed the first nano-sized red blood cell (RBC) (erythrocyte)-derived constructs loaded with the FDA-approved near infrared (NIR) dye indocyanine green (ICG).[29] We refer to these nanoparticles as NIR erythrocyte-derived transducers (NETs) since after NIR light excitation ICG is capable of fluorescence emission, heat generation, and the production of reactive oxygen species.[30] We have previously demonstrated that NETs can be functionalized in order to target a variety of cell types including cancer cells that express HER2 receptors,[33] and cells that over-express ephrin-B2 ligands.[152]

Herein we fabricate NETs co-loaded with ICG and Taxol as a representative chemotherapeutic. We demonstrate the successful functionalization of these NETs with a peptide (147B5) that is capable to binding to EphA2 receptors (147B5-NETs). Here the 147B5 will coat the surface of the NETs, resulting in multiple peptides being in the same vicinity when binding to EphA2 receptors and potentially leading to the efficient degradation of the receptors. We show that functionalization does not adversely affect the optical characteristics of the NETs. In addition, we investigate the effect of 147B5-NETs on MDA-MB-231 breast cancer cells, which have been shown to express high levels of EphA2.[236] The 147B5 peptide is still able to bind to EphA2 receptors, resulting in their degradation, after being functionalized to the NETs. Finally, these 147B5-NETs are able

to be selectively uptaken by EphA2 expressing breast cancer cells. Therefore, 147B5-NETs represent a potential cancer treatment modality that targets EphA2 receptors while also delivery payloads for imaging, phototherapy, and chemotherapy.

5.3 Materials and Methods

5.3.1 *Preparation of Peptide-Conjugated Streptavidin*

A solution of 500 nM Streptavidin, Alexa Fluor™ 594 conjugate (ThermoFisher Scientific) was incubated with 1500 nM of either the 147B5 peptide or the scrambled 147B5 peptide in 1xPBS for 2 hours at 37°C. The peptides were provided by the lab of Dr. Maurizio Pellecchia. The tubes were inverted every 20-30 minutes to facilitate solution mixing. Research has shown that biotin binds to streptavidin noncooperatively,[237,238] so since the incubating solution had a 3:1 molar ratio of biotin to streptavidin, on average each streptavidin will bind to 3 biotinylated peptides. The solution was kept at room temperature in the dark for 1 hour before being used to functionalize the NETs.

5.3.2 *Fabrication of Peptide-Functionalized NETs*

Whole mouse blood was drawn from female Swiss Webster mice via cardiac puncture. The syringes were coated in ≈150 μL of a 2 mg/mL of heparin lithium in milli-Q water. The collecting tube had 1 mL of the heparin lithium solution added for every 5 mL of mouse blood collected. The whole blood was washed in ≈ 320 mOsm phosphate buffered saline (PBS) (defined as 1xPBS) and erythrocytes were separated via centrifugation

(≈2800xg for 10 minutes at 4°C). The supernatant containing the plasma and buffy coat was removed, and the 1xPBS wash was repeated.

Intracellular hemoglobin was depleted from the erythrocytes via hypotonic treatment in 0.25xPBS. The erythrocytes were suspended in 0.25xPBS and incubated for ≈5 minutes at 4°C before being centrifuged (≈31,000xg for 20 minutes at 4°C). The supernatant containing depleted hemoglobin was removed, and the erythrocytes were resuspended in 0.25xPBS. The hemoglobin depletion step was repeated until the erythrocyte pellet was a pale pink and the supernatant was clear, resulting in erythrocyte ghosts (EGs). EGs were resuspended in 1xPBS.

To ensure that the relative number of EGs from one batch of particles to the next was consistent, the EGs solution was diluted to have an optical density of 1 at 280 nm, which corresponds to the proteins on the EGs. These diluted EGs were concentrated ≈59.5x, and were resuspended in a solution that was 98% 1xPBS and 2% 5 mg/mL solution of 1,2-distearoyl-*sn*-glycero-3-phosphoethanolamine-*N*-[biotin-(polyethylene glycol)] (DSPE-PEG-Biotin) (2 kDa PEG, Nanocs Inc.) in milli-Q water. The EGs were incubated with the DSPE-PEG-Biotin for at least 30 minutes at room temperature, allowing the insertion of the DSPE component into the membrane of the EGs, resulting in Biotin-EGs. This lipid-insertion method has been previously demonstrated for the use in functionalizing erythrocyte-derived particles.[88] We have previously validated this method for functionalizing NETs with a variety of functional groups.[33,35,141,152]

In order to scale the Biotin-EGs from the micro- to the nano-scale, the solution was diluted ≈30x in 1xPBS. The solution was then extruded through 2000 nm

polycarbonate porous filters (Whatman) using a 10 mL automatic extruder (LIPEX Extruder, Evonik Canada Inc.) two times, followed by three extrusions through 800 nm polycarbonate porous filters (Whatman). The resulting nano-Biotin-EGs were spun down (≈70,000xg for 1 hour at 4°C), the supernatant was removed, and the nano-Biotin-EGs were concentrated ≈6x in 1xPBS.

To load ICG and Taxol into the nano-Biotin-EGs, a 1:1:1 ratio solution of nano-Biotin EGs, 0.1 M Sorenson's buffer (Na_2HPO_4/NaH_2PO_4, 140 mOsm, pH ≈8), and a 50 nM Taxol and 75 μM ICG in milli-Q water solution were mixed together. The final concentrations of Taxol and ICG in the loading solution were ≈16.67 nM and 25 μM, respectively. The solution was centrifuged (≈70,000xg for 1 hour at 4°C) and the supernatant containing unloaded ICG and Taxol was removed. The resulting nano-Biotin-NETs were concentrated ≈12x in 1xPBS.

The nano-Biotin-NETs were incubated with either the 147B5 peptide conjugated streptavidin solution, or the scrambled 147B5 peptide conjugated streptavidin solution, at a 1:1 ratio for 2 hours at 37°C. The tubes were inverted every 20-30 minutes to facilitate solution mixing. The solutions were centrifuged (≈56,000xg for 1 hour at 4°C) and the supernatant containing unbound peptide-conjugated streptavidin was removed. The resulting 147B5-NETs and Scrambled-NETs were concentrated 4x to get the stock solutions of each nanoparticle.

5.3.3 *Characterization of NETs*

To determine the amount of streptavidin conjugated to the NETs, 1:10 dilutions of the NETs in 1xPBS were prepared. The raw fluorescence emission spectra in response to photoexcitation at 590 ± 2.5 nm filtered from a 450 W xenon lamp using a fluorometer (Fluorolog-3 spectrofluorometer, Edison) was collected from 605-750 nm. The raw fluorescence emission spectra were also collected for solutions of 100 nM, 50 nM, 25 nM, 12.5 nM, and 6.25 nM Streptavidin, Alexa Fluor™ 594 conjugate to create a standard curve relating the streptavidin concentration to the peak emission at 617 nm. The standard curve was then used to estimate the amount of streptavidin conjugated to each of the NETs solutions. The streptavidin concentration was multiplied by 3 to get the concentration of either the 147B5 peptide or the scrambled 147B5 peptide on the NETs. Concentrations of NETs refer to this calculated peptide concentration.

To characterize the NETs, 1:100 dilutions of the NETs stock solutions in 1xPBS were prepared. We used dynamic light scattering (DLS) (Zetasizer Nanoseries, NanoZS90, Malvern Instruments) to estimate the hydrodynamic diameters of all particles suspended in 1xPBS. We collected 9 measurements of each sample and present the average with the standard error of the mean. Optical density spectra of the NETs suspended in 1xPBS were recorded in the 280 to 1000 nm spectral ranges using a UV visible spectrophotometer (V670, JASCO) with an optical path length of 1 cm. Fluorescence emission spectra of the NETs suspended in 1xPBS in response to photoexcitation at 780 ± 2.5 nm was collected from 795-900 nm using a fluorometer as

described above. The fluorescence emission spectra of the NETs was normalized using the optical density of the excitation wavelength as follows:

$$\chi = \frac{F(\lambda)}{1-10^{-A(\lambda_{ex})}} \quad (1)$$

where F is the fluorescence emission intensity at a given wavelength (λ), and $A(\lambda_{ex})$ is the optical density of the sample at the excitation wavelength.

5.3.4 *Immunoblotting Analysis*

MDA-MD-231 breast cancer cells (American Type Culture Collection) and cultured in Dulbecco's Modified Eagle Medium (DMEM) supplemented with 10% fetal bovine serum (FBS) and 1% PenStrep (100U/mL penicillin and 100μg/mL streptomycin). Cells were plated overnight in 6-well plates. Cells were serum-starved for 1 hour prior to being treated with DMEM (negative control), 1 μg/mL ephrinA1-Fc (positive control), 50 nM 147B5-NETs, 200 nM 147B5-NETs, 50 nM Scrambled-NETs, or 200 nM Scrambled-NETs. Cells were incubated for 1 hour at 37°C in the dark. Cells were then harvested and lysed with a lysis buffer (20 mM Tris, pH 7.4, 120 mM NaCl, 1% Triton X-100, 0.5% sodium deoxycholate, 0.1% SDS, 1% IGEPAL, 5 mM EDTA) supplemented with EDTA-free protease inhibitor cocktail and PhosSTOP (Sigma-Aldrich). Lysates were subsequently centrifuged and the supernatants were collected. Supernatants were subjected to SDS-PAGE and transferred to PVDF membranes. The blots were blocked with 5% nonfat milk in TBS-T and probed with primary antibodies raised against EphA2 (ThermoFisher Scientific, 374400) or β-tubulin (Santa Cruz Biotechnology, sc-58884) at

4°C overnight. Blots were then incubated with HRP-conjugated goat anti-mouse secondary antibody (ThermoFisher Scientific) for 1 hour and protein bands were visualized using Clarity Western ECL kit (BIO-RAD) and imaged on a FluorChem (ProteinSimple) imaging system. Scans were processed and analyzed with AlphaView. For a relative comparison of EphA2 receptor degradation we calculated the ratio between the pixel intensity of the EphA2 band and the pixel intensity of the corresponding β-tubulin band.

5.3.5 *Fluorescence Cell Imaging*

MDA-MB-231 cells were plated on glass coverslips in 12-well plates overnight at 37°C. The cells were serum-starved for 1 hour before treatment with DMEM, 200 nM 147B5-NETs, or 200 nM Scrambled-NETs. The cells were incubated for 1 hour at 37°C in the dark. Cells were fixed with 4% paraformaldehyde for 20 min on ice and permeabilized with 0.2% Triton X-100 in PBS for 5 min. VectaShield antifade mounting medium with DAPI was added to the coverslips to stain the nuclei and the coverslips were transferred to glass slides. Images were acquired using an inverted ZEISS LSM 880 confocal microscope.

5.4 Results and Discussion

5.4.1 *Characterization of NETs*

The peak hydrodynamic diameters as measured by DLS were 103.82 ± 1.01 nm and 112.04 ± 2.65 nm for the 147B5-NETs and the Scrambled-NETs, respectively,

confirming the nano-size of the NETs (Figure 21). We have previously shown that DLS measurements are consistent with the sizes obtained by electron microscopy using TEM[29] and SEM[33] images.

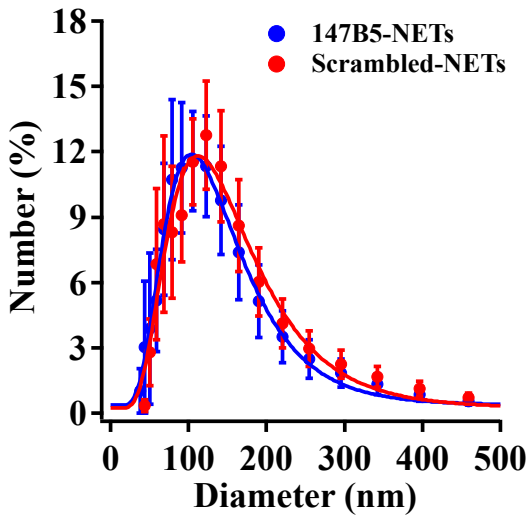

Figure 21. Hydrodynamic diameter distributions of 147B5-NETs and Scrambled-NETs. We present the average (circles) with standard error of the mean (error bars). Lognormal distributions are fitted to the measured data (solid traces). Blue data points and traces correspond to the 147B5-NETs. Red data points and traces correspond to the Scrambled-NETs.

Optical density spectra of the 147B5-NETs and Scrambled-NETs clearly show successful ICG loading with the characteristic peaks at ≈795 nm and ≈735 nm (Figure 22), corresponding to the monomeric and H-like aggregate forms of ICG, respectively, as we have previously reported.[29,157,223] The two sets of NETs have similar optical density at 280 nm (about 0.2-0.22) and at 795 nm (about 0.25), which corresponds to their protein and ICG concentrations, respectively.[157] These similar protein:ICG concentration ratios show that the final NETs formulations had similar ICG concentrations. The similar ICG

concentrations are also evident in the normalized emission spectra of the NETs after excitation at 780 nm (Figure 23). Both NETs show a strong emission peak near 800 nm, which gradually decreases until about 860 nm before leveling off. Again, this is consistent with our previous results.[152,157] Both the optical density and emission spectra demonstrate that the peptide functionalization process does not affect the ICG loading capabilities of the NETs.

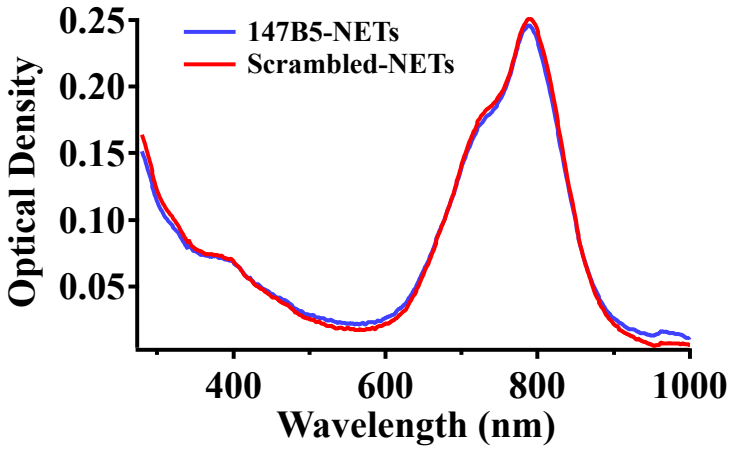

Figure 22. Optical density of 147B5-NETs (blue trace) and Scrambled-NETs (red trace) in 1xPBS over the spectral range of 280-1000 nm. The NETs stock solutions were diluted 1:100 in 1xPBS.

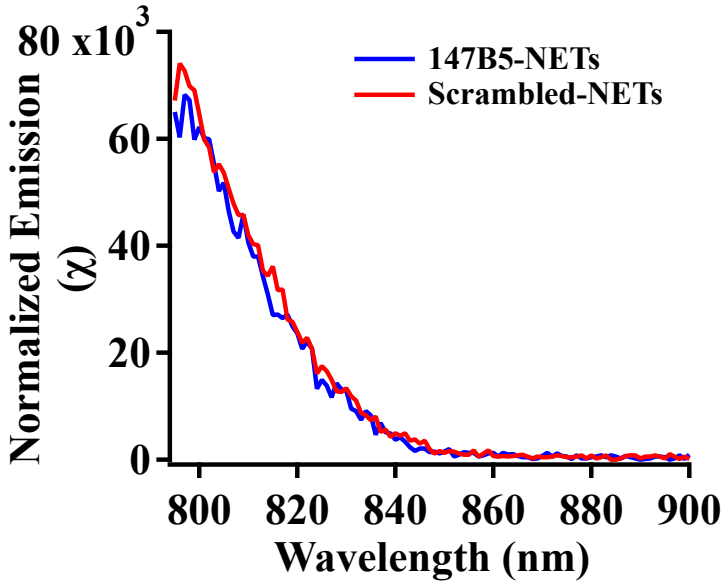

Figure 23. Normalized emission spectra of 147B5-NETs (blue trace) and Scrambled-NETs (red trace) in 1xPBS after excitation at 780 nm. The NETs stock solutions were diluted 1:100 in 1xPBS.

Raw emission spectra were also collected for solutions with known streptavidin, Alexa-Fluor™ 594 conjugate concentrations in 1xPBS. The emission of these solutions at 617 nm were used to generate a standard curve (data not shown), allowing us to estimate the streptavidin concentration of our NETs. The 1:10 dilutions of the 147B5-NETs and Scrambled-NETs were 40.96 nM and 43.43 nM, respectively. The stock solutions therefore had streptavidin concentrations of 409.6 nM for the 147B5-NETs and 434.3 nM for the Scrambled-NETs. Each streptavidin molecule is functionalized with three molecules of the biotinylated 147B5 or scrambled peptides, so the theoretical peptide concentrations are 1228.8 nM for the 147B5-NETs and 1302.9 nM for the Scrambled-NETs. In addition, the strong emission at 617 nm for both sets of NETs demonstrates their successful functionalization with their respective peptides (Figure 24).

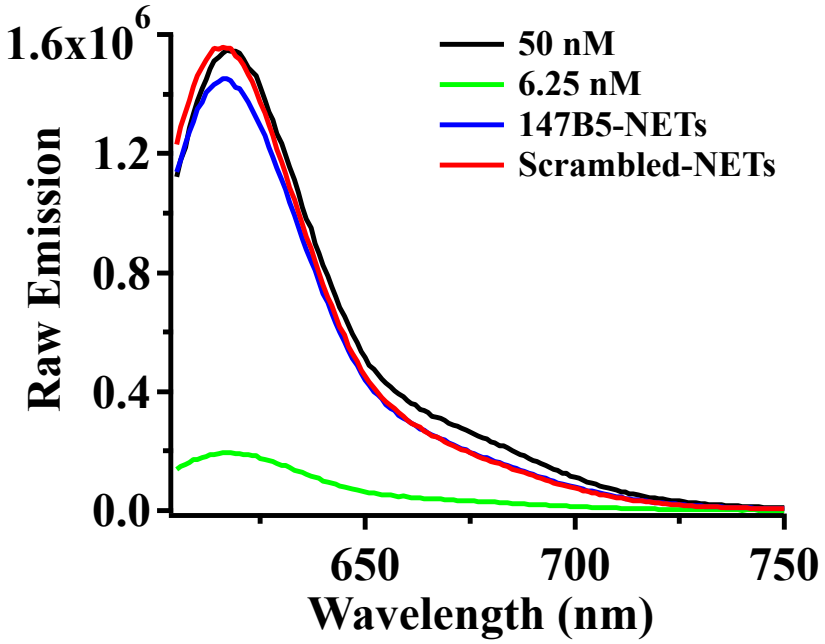

Figure 24. Raw emission of 147B5-NETs (blue trace) and Scrambled-NETs (red trace) in 1xPBS after excitation at 590 nm. For comparison the raw emission of streptavidin, Alexa-Fluor™ 594 conjugate at concentrations of 50 nM (black trace) and 6.25 nM (green trace) in 1xPBS are also shown. The NETs stock solutions were diluted 1:10 in 1xPBS.

5.4.2 *In vitro EphA2 Receptor Targeting and Degradation*

To determine if the peptides were able to induce EphA2 degradation MDA-MB-231 cells were incubated with 147B5-NETs and Scrambled-NETs and then analyzed using a Western blot. At a peptide concentration of 200 nM the 147B5-NETs showed a diminished band at 97 kDA, indicating EphA2 degradation (Figure 25a). When normalized to the expression of β-tubulin (band at 51 kDA), the 147B5-NETs at 200 nM showed receptor degradation that was slightly stronger than that of cells incubated with a positive control of ephrinA1 (Figure 25b). 147B5-NETs at a concentration of 50 nM and

Scrambled-NETs at 50 nM and 200 nM did not induce the degradation of the receptor. These results show that the 147B5 peptide is still able to induce EphA2 receptor degradation after being functionalized to NETs.

The 147B5-NETs were incubated with MDA-MB-231 cells for 1 hour at 37°C and then fixed to determine if the NETs were uptaken by the cells. Confocal imaging clearly shows increased streptavidin levels near the cell nucleus after incubation with the 147B5-NETs, as indicated by the increase in the red signal (Figure 26). There was minimal fluorescence in the red channel for cells that were incubated with just media or the Scrambled-NETs. This demonstrates that the 147B5-NETs were able to target and be selectively uptaken by the EphA2 expressing cells.

These results all demonstrate the successful functionalization of NETs with the 147B5 peptide. Furthermore, they show that the 147B5 peptides are still capable of stimulating EphA2 receptor degradation after being functionalized to the NETs, which not only has the potential to decrease EphA2 receptor levels on breast cancer cells, but also facilitates the targeted uptake of the NETs by cells expressing EphA2 receptors. This site-specific targeting also has the potential to allow for the targeted delivery of various payloads. Here we have demonstrated that the NETs can be loaded with representative payloads such as ICG, which we have shown is capable of being used for imaging, photothermal therapy, and photodynamic therapy for cancer *in vivo*.[30] The NETs were also loaded with Taxol in the loading solution, meaning they have the potential to also facilitate the site-specific delivery of chemotherapeutics. Therefore, 147B5-NETs

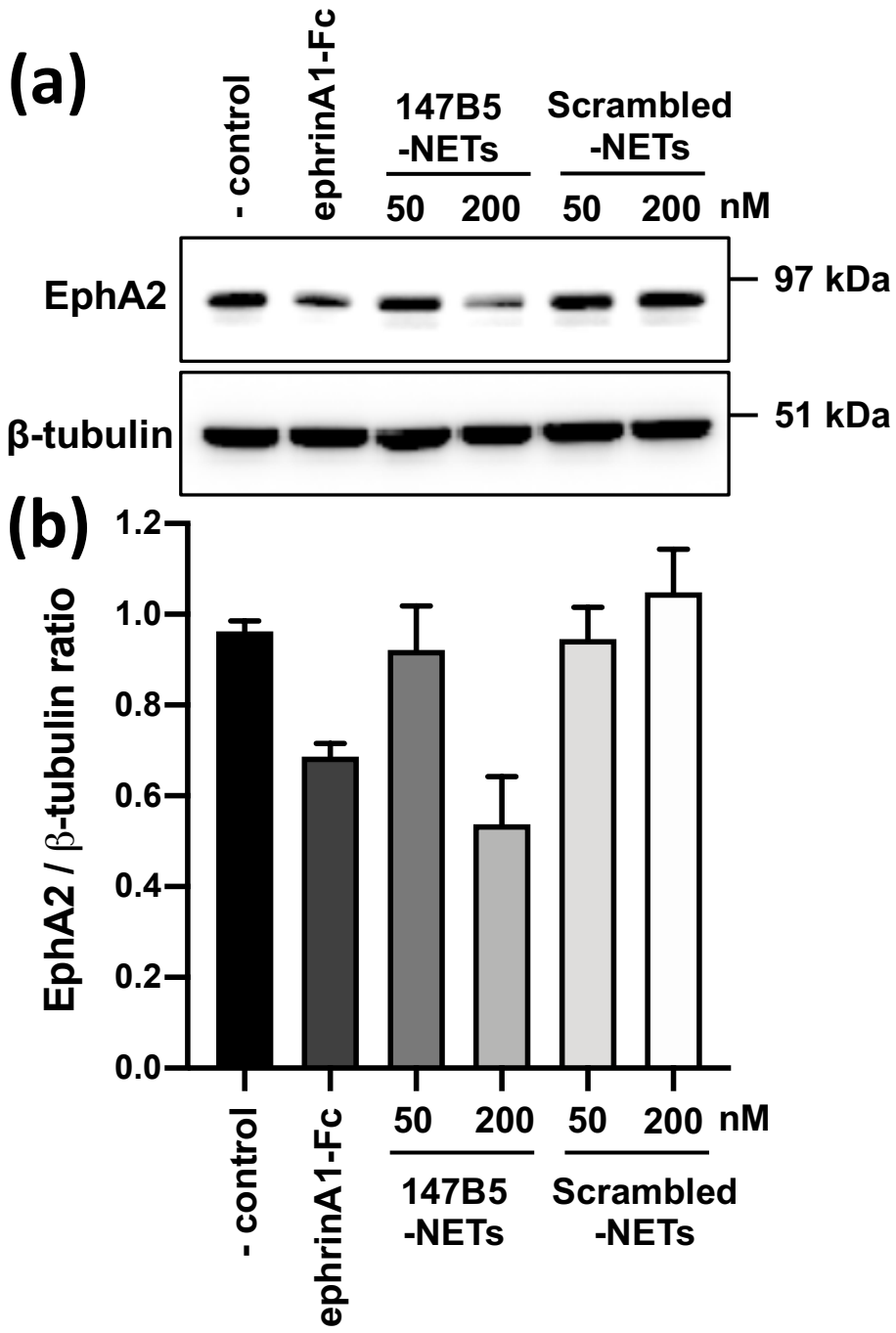

Figure 25. (a) Western blot demonstrating receptor degradation of EphA2 receptors with β-tubulin shown as a control. (b) Comparison of EphA2: β-tubulin ratios for controls, 147B5-NETs, and Scrambled-NETs.

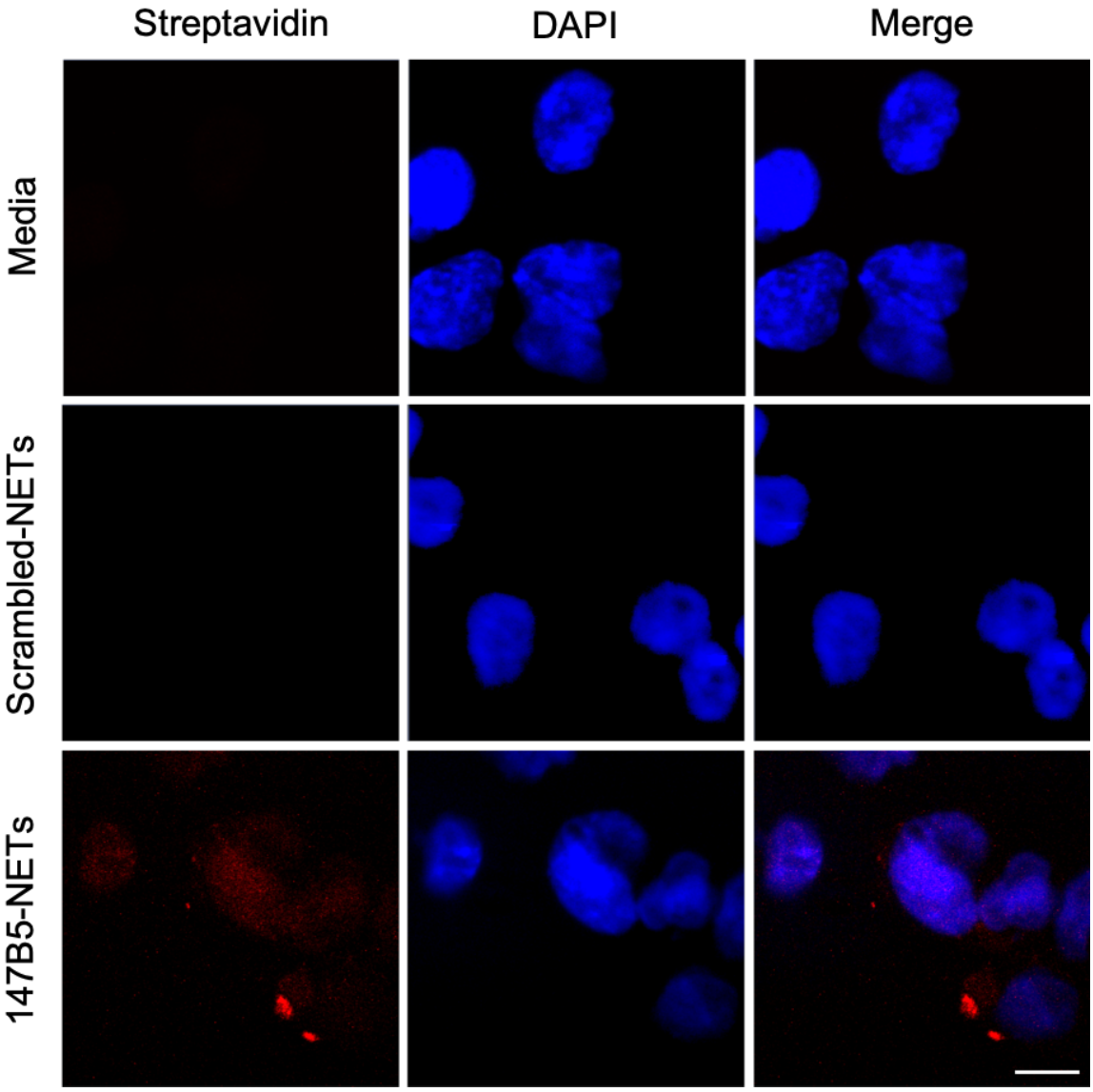

Figure 26. MDA-MB-231 cells incubated with media, Scrambled-NETs, and 147B5-NETs. Shown is the red fluorescence from the Streptavidin, Alexa-Fluor™ 594 conjugate and the blue fluorescence from the DAPI cell nuclei staining. Scale bar corresponds to 10 μm.

represent a promising payload delivery platform with the potential for multimodal cancer therapy.

5.5 Conclusions

We have demonstrated the successful functionalization of NETs with the 147B5 peptide that specifically targets EphA2 receptors. Characterization measurements indicated that the functionalization process does not affect the optical characteristics of the NETs. Fluorescence imaging shows the selective uptake of 147B5-NETs by EphA2 expressing cancer cells. Western blot analysis shows that the 147B5-NETs are also capable of degrading EphA2 receptors. These nano-constructs represent a promising payload delivery system for diseased cell states characterized by an over-expression of EphA2 receptors.

Chapter 6: Conclusions

These studies demonstrate the versatility of erythrocyte-derived particles loaded with ICG. In order to offer some context for the field of RBC-derived constructs in the second chapter we review the current trends for constructs that employ light-based mechanisms for imaging and therapeutics. We focus on the current methods for developing light-based RBC-derived constructs, as well as the different applications for which they are being investigated. While there is still a great deal of research needed before these constructs can be used clinically, we highlight the great potential of RBC-derived constructs for cancer and vascular theranostics.

Shifting our focus to NETs, in the third chapter we have found that while μNETs and nNETs result in significantly higher levels of TNF-α in the blood serum 6 hours post-injection compared to a negative control of PBS, only the nNETs induced significantly higher levels of IL-6 in the liver and spleen; TNF-α in the blood serum, liver, and spleen; and MCP-1 in the liver and spleen 2 hours post-injection compared to the negative control. In addition, functionalizing the nNETs with folate or Herceptin was associated with a reduction in IL-6 and MCP-1 in the blood serum, liver, and spleen; and lower concentrations of TNF-α and IL-10 in the blood serum. A second injection of μNETs did not lead to higher levels of any of the cytokines in the blood serum, liver, and spleen. After a second injection of nNETs only the IL-10 in the spleen was elevated compared to the levels after a single injection. Overall, these results suggest that NETs have the potential to be non-immunogenic and do not activate the adaptive immune system. While we have focused on the acute phase of the innate immune response, more

studies are needed to determine the immune response over longer periods of time and to fully assess the adaptive immune response to these particles.

In addition to probing the acute phase of the innate immune response we have looked at functionalizing nNETs to provide them with targeting capabilities. In the fourth chapter we detail the fabrication of NETs functionalized with the ligand binding domain of EphB1 receptors, resulting in F-NETs. Our optical measurements of the nanoparticles show that the functionalization process was successful, and that the process does not adversely affect the optical properties of the F-NETs. The EphB1 functionalization was also shown to furnish F-NETs with the ability to target ephrin-B2 ligand-expressing cells, as determined by quantifying the NIR fluorescence signal of the cells after incubation with the NETs. The uptake of F-NETs follows a sigmoidal function based on the relative number density of the F-NETs in the incubating solution. These results clearly illustrate the effectiveness of our functionalization method, and emphasize the potential F-NETs have in the targeted imaging of diseased cell states characterized by an over-expression of ephrin-B2 ligands.

Finally, in the fifth chapter we continue to explore the potential for nNETs to target the Eph/ephrin system. We functionalize nNETs with a peptide, 147B5, capable of binding to EphA2 receptors, leading to receptor degradation. We confirm these 147B5-NETs are functionalized using fluorescence emission measurements. In addition, optical density measurements verify the successful loading of ICG, indicating that the functionalization does not affect the optical characteristics of the 147B5-NETs. A solution of 147B5-NETs with a peptide concentration of 200 nM is sufficient to degrade

EphA2 receptors, denoting that the 147B5 peptides are still capable of binding to EphA2 receptors and inducing receptor degradation after being attached to the surface of the nNETs. Furthermore, MDA-MB-231 cancer cells are shown to selectively uptake the 147B5-NETs using confocal microscopy.

Altogether these findings underline the promise of NETs as non-immunogenic carriers of ICG for imaging and therapeutic applications. NETs have additionally been successfully functionalized with various targeting moieties, furnishing them with the capacity for the site-specific delivery of ICG to diseased cell states, particularly those characterized by the over-expression of Eph receptors and their ligands.

References

1. Yoo, J.-W., Irvine, D. J., Discher, D. E. & Mitragotri, S. Bio-inspired, bioengineered and biomimetic drug delivery carriers. *Nat. Rev. Drug Discov.* **10**, 521–535 (2011).

2. Muzykantov, V. R. Drug delivery by red blood cells: vascular carriers designed by Mother Nature. *Expert Opin. Drug Deliv.* **7**, 403–427 (2010).

3. Fang, R. H., Hu, C.-M. J. & Zhang, L. Nanoparticles disguised as red blood cells to evade the immune system. *Expert Opin. Biol. Ther.* **12**, 385–389 (2012).

4. Hu, C.-M. J., Fang, R. H. & Zhang, L. Erythrocyte-Inspired Delivery Systems. *Adv. Healthc. Mater.* **1**, 537–547 (2012).

5. Zarrin, A., Foroozesh, M. & Hamidi, M. Carrier erythrocytes: recent advances, present status, current trends and future horizons. *Expert Opin. Drug Deliv.* **11**, 433–447 (2014).

6. Gao, W. & Zhang, L. Engineering red-blood-cell-membrane–coated nanoparticles for broad biomedical applications. *AIChE J.* **61**, 738–746 (2015).

7. Villa, C. H., Seghatchian, J. & Muzykantov, V. Drug delivery by erythrocytes: "Primum non nocere". *Transfus. Apher. Sci.* **55**, 275–280 (2016).

8. Zhang, H. Erythrocytes in nanomedicine: an optimal blend of natural and synthetic materials. *Biomater. Sci.* **4**, 1024–1031 (2016).

9. Han, X., Wang, C. & Liu, Z. Red Blood Cells as Smart Delivery Systems. *Bioconjug. Chem.* **29**, 852–860 (2018).

10. Koleva, L., Bovt, E., Ataullakhanov, F. & Sinauridze, E. Erythrocytes as Carriers: From Drug Delivery to Biosensors. *Pharmaceutics* **12**, 276 (2020).

11. Antonelli, A. & Magnani, M. Red Blood Cells as Carriers of Iron Oxide-Based Contrast Agents for Diagnostic Applications. *J. Biomed. Nanotechnol.* **10**, 1732–1750.

12. Antonelli, A., Sfara, C. & Magnani, M. Intravascular contrast agents in diagnostic applications: Use of red blood cells to improve the lifespan and efficacy of blood pool contrast agents. *Nano Res.* **10**, 731–766 (2017).

13. Xia, Q., Zhang, Y., Li, Z., Hou, X. & Feng, N. Red blood cell membrane-camouflaged nanoparticles: a novel drug delivery system for antitumor application. *Acta Pharm. Sin. B* **9**, 675–689 (2019).

14. Sun, D. *et al.* Advances in refunctionalization of erythrocyte-based nanomedicine for enhancing cancer-targeted drug delivery. *Theranostics* **9**, 6885–6900 (2019).

15. Yannuzzi, L. A. Indocyanine Green Angiography: A Perspective on Use in the Clinical Setting. *Am. J. Ophthalmol.* **151**, 745-751.e1 (2011).

16. Vos, J. J., Wietasch, J. K. G., Absalom, A. R., Hendriks, H. G. D. & Scheeren, T. W. L. Green light for liver function monitoring using indocyanine green? An overview of current clinical applications. *Anaesthesia* **69**, 1364–1376 (2014).

17. van Manen, L. *et al.* A practical guide for the use of indocyanine green and methylene blue in fluorescence-guided abdominal surgery. *J. Surg. Oncol.* **118**, 283–300 (2018).

18. De Gasperi, A., Mazza, E. & Prosperi, M. Indocyanine green kinetics to assess liver function: Ready for a clinical dynamic assessment in major liver surgery? *World J. Hepatol.* **8**, 355–367 (2016).

19. Sun, X., Wang, C., Gao, M., Hu, A. & Liu, Z. Remotely Controlled Red Blood Cell Carriers for Cancer Targeting and Near-Infrared Light-Triggered Drug Release in Combined Photothermal–Chemotherapy. *Adv. Funct. Mater.* **25**, 2386–2394 (2015).

20. Hui, L., Qin, S. & Yang, L. Upper Critical Solution Temperature Polymer, Photothermal Agent, and Erythrocyte Membrane Coating: An Unexplored Recipe for Making Drug Carriers with Spatiotemporally Controlled Cargo Release. *ACS Biomater. Sci. Eng.* **2**, 2127–2132 (2016).

21. Ren, H. *et al.* Oxygen self-enriched nanoparticles functionalized with erythrocyte membranes for long circulation and enhanced phototherapy. *Acta Biomater.* **59**, 269–282 (2017).

22. Wan, G. *et al.* Nanoscaled red blood cells facilitate breast cancer treatment by combining photothermal/photodynamic therapy and chemotherapy. *Biomaterials* **155**, 25–40 (2018).

23. Liu, W. *et al.* Light-Triggered Biomimetic Nanoerythrocyte for Tumor-Targeted Lung Metastatic Combination Therapy of Malignant Melanoma. *Small* **14**, 1801754 (2018).

24. Ye, S. *et al.* Light/pH-Triggered Biomimetic Red Blood Cell Membranes Camouflaged Small Molecular Drug Assemblies for Imaging-Guided Combinational Chemo-Photothermal Therapy. *ACS Appl. Mater. Interfaces* **11**, 15262–15275 (2019).

25. Wang, P. *et al.* Fabrication of Red Blood Cell-Based Multimodal Theranostic Probes for Second Near-Infrared Window Fluorescence Imaging-Guided Tumor Surgery and Photodynamic Therapy. *Theranostics* **9**, 369–380 (2019).

26. Luo, L. *et al.* A RBC membrane-camouflaged biomimetic nanoplatform for enhanced chemo-photothermal therapy of cervical cancer. *J. Mater. Chem. B* **8**, 4080-4092 (2020).

27. Liu, W. *et al.* Self-activated *in vivo* therapeutic cascade of erythrocyte membrane-cloaked iron-mineralized enzymes. *Theranostics* **10**, 2201–2214 (2020).

28. Wang, P. *et al.* Bioinspired red blood cell membrane-encapsulated biomimetic nanoconstructs for synergistic and efficacious chemo-photothermal therapy. *Colloids Surf. B Biointerfaces* **189**, 110842 (2020).

29. Bahmani, B., Bacon, D. & Anvari, B. Erythrocyte-derived photo-theranostic agents: hybrid nano-vesicles containing indocyanine green for near infrared imaging and therapeutic applications. *Sci. Rep.* **3**, (2013).

30. Burns, J. M., Vankayala, R., Mac, J. T. & Anvari, B. Erythrocyte-Derived Theranostic Nanoplatforms for Near Infrared Fluorescence Imaging and Photodestruction of Tumors. *ACS Appl. Mater. Interfaces* **10**, 27621–27630 (2018).

31. Burns, J., Jia, W., Stuart Nelson, J., Majaron, B. & Anvari, B. Photothermal treatment of port-wine stains using erythrocyte-derived particles doped with indocyanine green: a theoretical study. *J. Biomed. Opt.* **23**, 1 (2018).

32. Peer, D. *et al.* Nanocarriers as an emerging platform for cancer therapy. *Nat. Nanotechnol.* **2**, 751–760 (2007).

33. Mac, J. T. *et al.* Erythrocyte-derived nano-probes functionalized with antibodies for targeted near infrared fluorescence imaging of cancer cells. *Biomed. Opt. Express* **7**, 1311–1322 (2016).

34. Oldenborg, P. A. *et al.* Role of CD47 as a marker of self on red blood cells. *Science* **288**, 2051–2054 (2000).

35. Vankayala, R. *et al.* Erythrocyte-Derived Nanoparticles as a Theranostic Agent for Near-Infrared Fluorescence Imaging and Thrombolysis of Blood Clots. *Macromol. Biosci.* **18**, 1700379 (2018).

36. Pattni, B. S. & Torchilin, V. P. Targeted Drug Delivery Systems: Strategies and Challenges. in *Targeted Drug Delivery : Concepts and Design* (eds. Devarajan, P. V. & Jain, S.) 3–38 (Springer International Publishing, 2015).

37. Sier, V. Q. *et al.* Cell-Based Tracers as Trojan Horses for Image-Guided Surgery. *Int. J. Mol. Sci.* **22**, 755 (2021).

38. Ihler, G. M., Glew, R. H. & Schnure, F. W. Enzyme Loading of Erythrocytes. *Proc. Natl. Acad. Sci. U. S. A.* **70**, 2663–2666 (1973).

39. Villa, C. H., Anselmo, A. C., Mitragotri, S. & Muzykantov, V. Red blood cells: Supercarriers for drugs, biologicals, and nanoparticles and inspiration for advanced delivery systems. *Adv. Drug Deliv. Rev.* **106**, 88–103 (2016).

40. Villa, C. H., Cines, D. B., Siegel, D. L. & Muzykantov, V. Erythrocytes as Carriers for Drug Delivery in Blood Transfusion and Beyond. *Transfus. Med. Rev.* **31**, 26–35 (2017).

41. Wu, Z. *et al.* RBC micromotors carrying multiple cargos towards potential theranostic applications. *Nanoscale* **7**, 13680–13686 (2015).

42. Guo, X. *et al.* Red blood cell membrane-mediated fusion of hydrophobic quantum dots with living cell membranes for cell imaging. *J. Mater. Chem. B* **4**, 4191–4197 (2016).

43. Li, C. *et al.* Red blood cell membrane-enveloped O2 self-supplementing biomimetic nanoparticles for tumor imaging-guided enhanced sonodynamic therapy. *Theranostics* **10**, 867–879 (2020).

44. Delcea, M. *et al.* Nanoplasmonics for Dual-Molecule Release through Nanopores in the Membrane of Red Blood Cells. *ACS Nano* **6**, 4169–4180 (2012).

45. Wang, D. *et al.* Erythrocyte–Cancer Hybrid Membrane Camouflaged Hollow Copper Sulfide Nanoparticles for Prolonged Circulation Life and Homotypic-Targeting Photothermal/Chemotherapy of Melanoma. *ACS Nano* **12**, 5241–5252 (2018).

46. Liu, Z. *et al.* Fabrication of red blood cell membrane-camouflaged Cu2−xSe nanoparticles for phototherapy in the second near-infrared window. *Chem. Commun.* **55**, 6523–6526 (2019).

47. Milanick, M. A., Ritter, S. & Meissner, K. Engineering erythrocytes to be erythrosensors: First steps. *Blood Cells. Mol. Dis.* **47**, 100–106 (2011).

48. Wang, L., Chen, S., Pei, W., Huang, B. & Niu, C. Magnetically targeted erythrocyte membrane coated nanosystem for synergistic photothermal/chemotherapy of cancer. *J. Mater. Chem. B* **8**, 4132-4142 (2020).

49. Ren, X. *et al.* Red blood cell membrane camouflaged magnetic nanoclusters for imaging-guided photothermal therapy. *Biomaterials* **92**, 13–24 (2016).

50. Li, J. *et al.* Seedless synthesis of gold nanorods with (+)-catechin-assisted and red blood cell membranes coating as a biomimetic photothermal agents. *Mater. Technol.* **33**, 825–834 (2018).

51. He, L. *et al.* Designing Bioinspired 2D MoSe2 Nanosheet for Efficient Photothermal-Triggered Cancer Immunotherapy with Reprogramming Tumor-Associated Macrophages. *Adv. Funct. Mater.* **29**, 1901240 (2019).

52. Chen, W. *et al.* Cell Membrane Camouflaged Hollow Prussian Blue Nanoparticles for Synergistic Photothermal-/Chemotherapy of Cancer. *Adv. Funct. Mater.* **27**, 1605795 (2017).

53. Wang, M., Abbineni, G., Clevenger, A., Mao, C. & Xu, S. Upconversion nanoparticles: synthesis, surface modification and biological applications. *Nanomedicine Nanotechnol. Biol. Med.* **7**, 710–729 (2011).

54. Ding, H. *et al.* Erythrocyte membrane-coated NIR-triggered biomimetic nanovectors with programmed delivery for photodynamic therapy of cancer. *Nanoscale* **7**, 9806–9815 (2015).

55. Yang, Q., Xiao, Y., Yin, Y., Li, G. & Peng, J. Erythrocyte Membrane-Camouflaged IR780 and DTX Coloading Polymeric Nanoparticles for Imaging-Guided Cancer Photo–Chemo Combination Therapy. *Mol. Pharm.* **16**, 3208–3220 (2019).

56. Su, J. *et al.* Bioinspired Nanoparticles with NIR-Controlled Drug Release for Synergetic Chemophotothermal Therapy of Metastatic Breast Cancer. *Adv. Funct. Mater.* **26**, 7495–7506 (2016).

57. Guo, P. *et al.* Nanomaterial Preparation by Extrusion through Nanoporous Membranes. *Small* **14**, 1703493 (2018).

58. Borthwick, K. A. J. *et al.* Development of a novel compact sonicator for cell disruption. *J. Microbiol. Methods* **60**, 207–216 (2005).

59. Kuo, Y.-C. *et al.* Colloidal Properties of Nanoerythrosomes Derived from Bovine Red Blood Cells. *Langmuir* **32**, 171–179 (2016).

60. Rao, L. *et al.* Erythrocyte Membrane-Coated Upconversion Nanoparticles with Minimal Protein Adsorption for Enhanced Tumor Imaging. *ACS Appl. Mater. Interfaces* **9**, 2159–2168 (2017).

61. Zhu, D.-M. *et al.* Erythrocyte membrane-coated gold nanocages for targeted photothermal and chemical cancer therapy. *Nanotechnology* **29**, 084002 (2018).

62. Rao, L. *et al.* Photocatalytic Degradation of Cell Membrane Coatings for Controlled Drug Release. *Adv. Healthc. Mater.* **5**, 1420–1427 (2016).

63. Wang, S. *et al.* Red-blood-cell-membrane-enveloped magnetic nanoclusters as a biomimetic theranostic nanoplatform for bimodal imaging-guided cancer photothermal therapy. *J. Mater. Chem. B* **8**, 803–812 (2020).

64. Peng, J. *et al.* Erythrocyte-Membrane-Coated Prussian Blue/Manganese Dioxide Nanoparticles as H2O2-Responsive Oxygen Generators To Enhance Cancer Chemotherapy/Photothermal Therapy. *ACS Appl. Mater. Interfaces* **9**, 44410–44422 (2017).

65. Li, M. *et al.* Red blood cell membrane-coated upconversion nanoparticles for pretargeted multimodality imaging of triple-negative breast cancer. *Biomater. Sci.* **8**, 1802–1814 (2020).

66. Jiang, Q. *et al.* Red blood cell membrane-camouflaged melanin nanoparticles for enhanced photothermal therapy. *Biomaterials* **143**, 29–45 (2017).

67. Gao, C. *et al.* Red Blood Cell-Mimicking Micromotor for Active Photodynamic Cancer Therapy. *ACS Appl. Mater. Interfaces* **11**, 23392–23400 (2019).

68. Flower, R. *et al.* Observation of Erythrocyte Dynamics in the Retinal Capillaries and Choriocapillaris Using ICG-Loaded Erythrocyte Ghost Cells. *Invest. Ophthalmol. Vis. Sci.* **49**, 5510–5516 (2008).

69. Ritter, S. C., Milanick, M. A. & Meissner, K. E. Encapsulation of FITC to monitor extracellular pH: a step towards the development of red blood cells as circulating blood analyte biosensors. *Biomed. Opt. Express* **2**, 2012–2021 (2011).

70. Gao, M. *et al.* Photosensitizer Decorated Red Blood Cells as an Ultrasensitive Light-Responsive Drug Delivery System. *ACS Appl. Mater. Interfaces* **9**, 5855–5863 (2017).

71. Jiang, A. *et al.* Doxorubicin-loaded silicon nanoparticles impregnated into red blood cells featuring bright fluorescence, strong photostability, and lengthened blood residency. *Nano Res.* **11**, 2285–2294 (2018).

72. Chen, Z.-A., Wu, S.-H., Chen, P., Chen, Y.-P. & Mou, C.-Y. Critical Features for Mesoporous Silica Nanoparticles Encapsulated into Erythrocytes. *ACS Appl. Mater. Interfaces* **11**, 4790–4798 (2019).

73. Vankayala, R. *et al.* Biodistribution and toxicological evaluation of micron- and nano-sized erythrocyte-derived optical particles in healthy Swiss Webster mice. *Biomater. Sci.* **7**, 2123–2133 (2019).

74. Gutiérrez Millán, C., Castañeda, A. Z., Sayalero Marinero, Ma. L. & Lanao, J. M. Factors associated with the performance of carrier erythrocytes obtained by hypotonic dialysis. *Blood Cells. Mol. Dis.* **33**, 132–140 (2004).

75. López, S. C. B. & Meissner, K. E. Characterization of carrier erythrocytes for biosensing applications. *J. Biomed. Opt.* **22**, 091510 (2017).

76. Marvin, C. M. *et al.* On Command Drug Delivery via Cell-Conveyed Phototherapeutics. *Small* **15**, 1901442 (2019).

77. An, X., Schulz, V. P., Mohandas, N. & Gallagher, P. G. Human and murine erythropoiesis. *Curr. Opin. Hematol.* **22**, 206–211 (2015).

78. Gordesky, S. E. & Marinetti, G. V. The asymmetric arrangement of phospholipids in the human erythrocyte membrane. *Biochem. Biophys. Res. Commun.* **50**, 1027–1031 (1973).

79. Lang, F., Lang, K. S., Lang, P. A., Huber, S. M. & Wieder, T. Mechanisms and Significance of Eryptosis. *Antioxid. Redox Signal.* **8**, 1183–1192 (2006).

80. Wang, C. *et al.* Multifunctional Theranostic Red Blood Cells For Magnetic-Field-Enhanced in vivo Combination Therapy of Cancer. *Adv. Mater.* **26**, 4794–4802 (2014).

81. Sun, X., Wang, C., Gao, M., Hu, A. & Liu, Z. Remotely Controlled Red Blood Cell Carriers for Cancer Targeting and Near-Infrared Light-Triggered Drug Release in Combined Photothermal–Chemotherapy. *Adv. Funct. Mater.* **25**, 2386–2394 (2015).

82. Weaver, J. C. & Chizmadzhev, Yu. A. Theory of electroporation: A review. *Bioelectrochem. Bioenerg.* **41**, 135–160 (1996).

83. Mac, J. T., Vankayala, R., Patel, D. K., Wueste, S. & Anvari, B. Erythrocyte-Derived Optical Nanoprobes Doped with Indocyanine Green-Bound Albumin: Material Characteristics and Evaluation for Cancer Cell Imaging. *ACS Biomater. Sci. Eng.* **4**, 3055–3062 (2018).

84. Mojzisova, H., Bonneau, S., Vever-Bizet, C. & Brault, D. Cellular uptake and subcellular distribution of chlorin e6 as functions of pH and interactions with membranes and lipoproteins. *Biochim. Biophys. Acta BBA - Biomembr.* **1768**, 2748–2756 (2007).

85. Sun, L. *et al.* Light-activatable Chlorin e6 (Ce6)-imbedded erythrocyte membrane vesicles camouflaged Prussian blue nanoparticles for synergistic photothermal and photodynamic therapies of cancer. *Biomater. Sci.* **6**, 2881–2895 (2018).

86. Kalchenko, V. *et al.* Use of lipophilic near-infrared dye in whole-body optical imaging of hematopoietic cell homing. *J. Biomed. Opt.* **11**, 050507 (2006).

87. Flower, R. W. & Kling, R. Observation and characterization of microvascular vasomotion using erythrocyte mediated ICG angiography (EM-ICG-A). *Microvasc. Res.* **113**, 78–87 (2017).

88. Fang, R. H. *et al.* Lipid-insertion enables targeting functionalization of erythrocyte membrane-cloaked nanoparticles. *Nanoscale* **5**, 8884 (2013).

89. Wang, P. *et al.* Orthogonal near-infrared upconversion co-regulated site-specific O2 delivery and photodynamic therapy for hypoxia tumor by using red blood cell microcarriers. *Biomaterials* **125**, 90–100 (2017).

90. Diamandis, E. P. & Christopoulos, T. K. The biotin-(strept)avidin system: principles and applications in biotechnology. *Clin. Chem.* **37**, 625–636 (1991).

91. Tang, W. *et al.* Red Blood Cell-Facilitated Photodynamic Therapy for Cancer Treatment. *Adv. Funct. Mater.* **26**, 1757–1768 (2016).

92. Li, Z. *et al.* Plant Protein-Directed Synthesis of Luminescent Gold Nanocluster Hybrids for Tumor Imaging. *ACS Appl. Mater. Interfaces* **10**, 83–90 (2018).

93. Wang, D., Haytham, A., Mayo, L., Tao, Y. & Saeedi, O. Automated retinal microvascular velocimetry based on erythrocyte mediated angiography. *Biomed. Opt. Express* **10**, 3681–3697 (2019).

94. Zhou, J., Liu, Q., Feng, W., Sun, Y., & Li, F. Upconversion Luminescent Materials: Advances and Applications. *Chem. Rev.* **115**, 395-465 (2015).

95. Singh, N., Varma, A., Verma, A., Maurya, B. N. & Dash, D. Relief from vascular occlusion using photothermal ablation of thrombus with a multimodal perspective. *Nano Res.* **9**, 2327–2337 (2016).

96. Kelkar, S. S. & Reineke, T. M. Theranostics: Combining Imaging and Therapy. *Bioconjug. Chem.* **22**, 1879–1903 (2011).

97. Li, J. *et al.* Seedless preparation of Au nanorods by hydroquinone assistant and red blood cell membrane camouflage. *RSC Adv.* **8**, 21316–21325 (2018).

98. Piao, J.-G. *et al.* Erythrocyte Membrane Is an Alternative Coating to Polyethylene Glycol for Prolonging the Circulation Lifetime of Gold Nanocages for Photothermal Therapy. *ACS Nano* **8**, 10414–10425 (2014).

99. Estelrich, J. & Busquets, M. A. Iron Oxide Nanoparticles in Photothermal Therapy. *Mol. J. Synth. Chem. Nat. Prod. Chem.* **23**, (2018).

100. Rao, L. *et al.* Microfluidic Electroporation-Facilitated Synthesis of Erythrocyte Membrane-Coated Magnetic Nanoparticles for Enhanced Imaging-Guided Cancer Therapy. *ACS Nano* **11**, 3496–3505 (2017).

101. Brightman, L. A., Geronemus, R. G. & Reddy, K. K. Laser treatment of port-wine stains. *Clin. Cosmet. Investig. Dermatol.* **8**, 27–33 (2015).

102. Abrahamse, H. & Hamblin, M. R. New photosensitizers for photodynamic therapy. *Biochem. J.* **473**, 347–364 (2016).

103. Muz, B., de la Puente, P., Azab, F. & Azab, A. K. The role of hypoxia in cancer progression, angiogenesis, metastasis, and resistance to therapy. *Hypoxia* **3**, 83–92 (2015).

104. Li, X., Kwon, N., Guo, T., Liu, Z. & Yoon, J. Innovative Strategies for Hypoxic-Tumor Photodynamic Therapy. *Angew. Chem. Int. Ed.* **57**, 11522–11531 (2018).

105. Liu, W.-L. *et al.* Aggressive Man-Made Red Blood Cells for Hypoxia-Resistant Photodynamic Therapy. *Adv. Mater.* **30**, 1802006 (2018).

106. Tardivo, J. P. *et al.* Methylene blue in photodynamic therapy: From basic mechanisms to clinical applications. *Photodiagnosis Photodyn. Ther.* **2**, 175–191 (2005).

107. López-Lázaro, M. Dual role of hydrogen peroxide in cancer: Possible relevance to cancer chemoprevention and therapy. *Cancer Lett.* **252**, 1–8 (2007).

108. Lisanti, M. P. *et al.* Hydrogen peroxide fuels aging, inflammation, cancer metabolism and metastasis. *Cell Cycle* **10**, 2440–2449 (2011).

109. Oberley, T. D. & Oberley, L. W. Antioxidant enzyme levels in cancer. *Histol. Histopathol.* **12**, 525-535 (1997).

110. Du, B. *et al.* Oxygen Self-Production Red Blood Cell Carrier System for MRI Mediated Cancer Therapy: Ferryl-Hb, Sonodynamic, and Chemical Therapy. *ACS Biomater. Sci. Eng.* **4**, 4132–4143 (2018).

111. Zhao, Y. *et al.* Metal-Organic Frameworks with Enhanced Photodynamic Therapy: Synthesis, Erythrocyte Membrane Camouflage, and Aptamer Targeted aggregation. *ACS Appl. Mater. Interfaces* **12**, 23697-23706 (2020).

112. Li, S. & Zhang, L. Erythrocyte membrane nano-capsules: biomimetic delivery and controlled release of photothermal–photochemical coupling agents for cancer cell therapy. *Dalton Trans.* **49**, 2645–2651 (2020).

113. Hughes, R. M. *et al.* Phototriggered Secretion of Membrane Compartmentalized Bioactive Agents. *Angew. Chem. Int. Ed.* **55**, 16080–16083 (2016).

114. Mroz, P., Yaroslavsky, A., Kharkwal, G. B. & Hamblin, M. R. Cell Death Pathways in Photodynamic Therapy of Cancer. *Cancers* **3**, 2516–2539 (2011).

115. Granville, D. J., Levy, J. G. & Hunt, D. W. Photodynamic therapy induces caspase-3 activation in HL-60 cells. *Cell Death Differ.* **4**, 623–628 (1997).

116. Xue, L.-Y., Chiu, S.-M., & Oleinick, N. L. Photodynamic Therapy-Induced Death of MCF-7 Human Breast Cancer Cells: A Role for Caspase-3 in the Late Steps of Apoptosis but Not for the Critical Lethal Event. *Exp. Cell Res.* **263**, 145-155 (2001).

117. Kessel, D. & Luo, Y. Photodynamic therapy: A mitochondrial inducer of apoptosis. *Cell Death Differ.* **6**, 28–35 (1999).

118. Marvin, C. M. *et al.* On Command Drug Delivery via Cell-Conveyed Phototherapeutics. *Small* **15**, 1901442 (2019).

119. Liu, J.-M., Zhang, D.-D., Fang, G.-Z. & Wang, S. Erythrocyte membrane bioinspired near-infrared persistent luminescence nanocarriers for in vivo long-circulating bioimaging and drug delivery. *Biomaterials* **165**, 39–47 (2018).

120. Pei, Q. *et al.* Light-Activatable Red Blood Cell Membrane-Camouflaged Dimeric Prodrug Nanoparticles for Synergistic Photodynamic/Chemotherapy. *ACS Nano* **12**, 1630–1641 (2018).

121. Zhao, N., Woodle, M. C. & Mixson, A. J. Advances in delivery systems for doxorubicin. *J. Nanomedicine Nanotechnol.* **9**, (2018).

122. Shao, J. *et al.* Erythrocyte Membrane Modified Janus Polymeric Motors for Thrombus Therapy. *ACS Nano* **12**, 4877–4885 (2018).

123. Su, J. *et al.* Enhanced Blood Suspensibility and Laser-Activated Tumor-specific Drug Release of Theranostic Mesoporous Silica Nanoparticles by Functionalizing with Erythrocyte Membranes. *Theranostics* **7**, 523–537 (2017).

124. Liu, B. *et al.* RBC membrane camouflaged prussian blue nanoparticles for gamabutolin loading and combined chemo/photothermal therapy of breast cancer. *Biomaterials* **217**, 119301 (2019).

125. Alander, J. T. *et al.* A Review of Indocyanine Green Fluorescent Imaging in Surgery. *Int. J. Biomed. Imaging* **2012**, 940585 (2012).

126. Yang, Z. *et al.* Advances in nanomaterials for use in photothermal and photodynamic therapeutics. *Mol. Med. Rep.* **20**, 5–15 (2019).

127. Golombek, S. K. *et al.* Tumor Targeting via EPR: Strategies to Enhance Patient Responses. *Adv. Drug Deliv. Rev.* **130**, 17–38 (2018).

128. Siemann, D. W. The Unique Characteristics of Tumor Vasculature and Preclinical Evidence for its Selective Disruption by Tumor-Vascular Disrupting Agents. *Cancer Treat. Rev.* **37**, 63–74 (2011).

129. Danhier, F. To exploit the tumor microenvironment: Since the EPR effect fails in the clinic, what is the future of nanomedicine? *J. Controlled Release* **244**, 108–121 (2016).

130. Leamon, C. P. & Low, P. S. Folate-mediated targeting: from diagnostics to drug and gene delivery. *Drug Discov. Today* **6**, 44–51 (2001).

131. Teng, L., Xie, J., Teng, L. & Lee, R. J. Clinical translation of folate receptor-targeted therapeutics. *Expert Opin. Drug Deliv.* **9**, 901–908 (2012).

132. Garanger, E., Boturyn, D. & Dumy, P. Tumor Targeting with RGD Peptide Ligands-Design of New Molecular Conjugates for Imaging and Therapy of Cancers. *Anticancer Agents Med. Chem.* **7**, 552–558 (2007).

133. Liu, Z., Wang, F. & Chen, X. Integrin αvβ3-Targeted Cancer Therapy. *Drug Dev. Res.* **69**, 329–339 (2008).

134. Ou, W. *et al.* Tailored Black Phosphorus for Erythrocyte Membrane Nanocloaking with Interleukin-1α siRNA and Paclitaxel for Targeted, Durable, and Mild Combination Cancer Therapy. *Theranostics* **9**, 6780–6796 (2019).

135. Xiao, F. *et al.* An erythrocyte membrane coated mimetic nano-platform for chemo-phototherapy and multimodal imaging. *RSC Adv.* **9**, 27911–27926 (2019).

136. Xuan, M. *et al.* Magnetic Mesoporous Silica Nanoparticles Cloaked by Red Blood Cell Membranes: Applications in Cancer Therapy. *Angew. Chem. Int. Ed.* **57**, 6049–6053 (2018).

137. Lin, K. *et al.* Facile phase transfer of hydrophobic Fe3O4@Cu2−xS nanoparticles by red blood cell membrane for MRI and phototherapy in the second near-infrared window. *J. Mater. Chem. B* **8**, 1202–1211 (2020).

138. Liu, Y. *et al.* Erythrocyte–platelet hybrid membranes coating polypyrrol nanoparticles for enhanced delivery and photothermal therapy. *J. Mater. Chem. B* **6**, 7033–7041 (2018).

139. Jiang, Q. *et al.* Erythrocyte-cancer hybrid membrane-camouflaged melanin nanoparticles for enhancing photothermal therapy efficacy in tumors. *Biomaterials* **192**, 292–308 (2019).

140. Rao, L. *et al.* Red Blood Cell Membrane as a Biomimetic Nanocoating for Prolonged Circulation Time and Reduced Accelerated Blood Clearance. *Small* **11**, 6225–6236 (2015).

141. Hanley, T. M., Vankayala, R., Mac, J. T., Lo, D. D. & Anvari, B. Acute Immune Response of Micro- and Nanosized Erythrocyte-Derived Optical Particles in Healthy Mice. *Mol. Pharm.* **17**, 3900-3914 (2020).

142. Singh, D., Dilnawaz, F. & Sahoo, S. K. Challenges of moving theranostic nanomedicine into the clinic. *Nanomed.* **15**, 111–114 (2020).

143. Frangioni, J. V. In vivo near-infrared fluorescence imaging. *Curr. Opin. Chem. Biol.* **7**, 626–634 (2003).

144. Hong, G., Antaris, A. L. & Dai, H. Near-infrared fluorophores for biomedical imaging. *Nat. Biomed. Eng.* **1**, (2017).

145. Weissleder, R. A clearer vision for in vivo imaging. *Nat. Biotechnol.* **19**, 316–317 (2001).

146. Veys, I. *et al.* ICG fluorescence imaging as a new tool for optimization of pathological evaluation in breast cancer tumors after neoadjuvant chemotherapy. *PLoS ONE* **13**, (2018).

147. Nagahara, R. *et al.* Fluorescence tumor imaging by i.v. administered indocyanine green in a mouse model of colitis-associated colon cancer. *Cancer Sci.* **109**, 1638–1647 (2018).

148. Cowan, V. Evaluation of Liver Function. in *Liver anesthesiology and critical care medicine* (ed. Wagener, G.) 79-85 (Springer Berlin Heidelberg, 2018).

149. Hamidi, M., Zarrin, A., Foroozesh, M. & Mohammadi-Samani, S. Applications of carrier erythrocytes in delivery of biopharmaceuticals. *J. Controlled Release* **118**, 145–160.

150. Bahmani, B., Bacon, D. & Anvari, B. Erythrocyte-derived photo-theranostic agents: hybrid nano-vesicles containing indocyanine green for near infrared imaging and therapeutic applications. *Sci. Rep.* **3**, 2180 (2013).

151. Jia, W. *et al.* Intravital Vascular Phototheranostics and Real-Time Circulation Dynamics of Micro- and Nanosized Erythrocyte-Derived Carriers. *ACS Appl. Mater. Interfaces* **12**, 275–287 (2020).

152. Hanley, T., Yin, R., Mac, J. T., Tan, W. & Anvari, B. Functionalized erythrocyte-derived optical nanoparticles to target ephrin-B2 ligands. *J. Biomed. Opt.* **24**, 085002 (2019).

153. Hui, L., Qin, S. & Yang, L. Upper Critical Solution Temperature Polymer, Photothermal Agent, and Erythrocyte Membrane Coating: An Unexplored Recipe for Making Drug Carriers with Spatiotemporally Controlled Cargo Release. *ACS Biomater. Sci. Eng.* **2**, 2127–2132 (2016).

154. Sun, X., Wang, C., Gao, M., Hu, A. & Liu, Z. Remotely Controlled Red Blood Cell Carriers for Cancer Targeting and Near-Infrared Light-Triggered Drug Release in Combined Photothermal–Chemotherapy. *Adv. Funct. Mater.* **25**, 2386–2394 (2015).

155. Ren, H. *et al.* Oxygen self-enriched nanoparticles functionalized with erythrocyte membranes for long circulation and enhanced phototherapy. *Acta Biomater.* **59**, 269–282 (2017).

156. Wang, P. *et al.* Fabrication of Red Blood Cell-Based Multimodal Theranostic Probes for Second Near-Infrared Window Fluorescence Imaging-Guided Tumor Surgery and Photodynamic Therapy. *Theranostics* **9**, 369–380 (2019).

157. Tang, J. C., Partono, A. & Anvari, B. Near-Infrared-Fluorescent Erythrocyte-Mimicking Particles: Physical and Optical Characteristics. *IEEE Trans. Biomed. Eng.* **66**, 1034–1044 (2019).

158. Siegel, B. A. *et al.* Evaluation of 111In-DTPA-Folate as a Receptor-Targeted Diagnostic Agent for Ovarian Cancer: Initial Clinical Results. *J. Nucl. Med.* **44**, 700–707 (2003).

159. Vergote, I. B., Marth, C. & Coleman, R. L. Role of the folate receptor in ovarian cancer treatment: evidence, mechanism, and clinical implications. *Cancer Metastasis Rev.* **34**, 41–52 (2015).

160. Moasser, M. M. Targeting the function of the HER2 oncogene in human cancer therapeutics. *Oncogene* **26**, 6577–6592 (2007).

161. Gutierrez, C. & Schiff, R. HER2: Biology, Detection, and Clinical Implications. *Arch. Pathol. Lab. Med.* **135**, 55–62 (2011).

162. Amsen, D., de Visser, K. E. & Town, T. Approaches to Determine Expression of Inflammatory Cytokines. *Methods Mol. Biol. Clifton NJ* **511**, 107–142 (2009).

163. Deshmane, S. L., Kremlev, S., Amini, S. & Sawaya, B. E. Monocyte Chemoattractant Protein-1 (MCP-1): An Overview. *J. Interferon Cytokine Res.* **29**, 313–326 (2009).

164. Gee, K., Guzzo, C., Mat, N. F. C. & Kumar, W. M. and A. The IL-12 Family of Cytokines in Infection, Inflammation and Autoimmune Disorders. *Inflamm. Allergy Drug Targets* **8**, 40-52 (2009).

165. Chen, L. *et al.* Inflammatory responses and inflammation-associated diseases in organs. *Oncotarget* **9**, 7204–7218 (2017).

166. Berg, D. J. *et al.* Interleukin-10 is a central regulator of the response to LPS in murine models of endotoxic shock and the Shwartzman reaction but not endotoxin tolerance. *J. Clin. Invest.* **96**, 2339–2347 (1995).

167. Ren, J., Ding, Y., Yu, H., Zhou, Y. & Yu, W. Effects on the expression of pro-inflammatory cytokines in the liver and spleen after oral administration of Porphyromonas gingivalis in mice. *Biomed. Res.* **29**, (2018).

168. Moghimi, S. M. *et al.* Material properties in complement activation. *Adv. Drug Deliv. Rev.* **63**, 1000–1007 (2011).

169. Markiewski, M. M. & Lambris, J. D. The role of complement in inflammatory diseases from behind the scenes into the spotlight. *Am. J. Pathol.* **171**, 715–727 (2007).

170. Takabayashi, T. *et al.* A new biologic role for C3a and C3a desArg: regulation of TNF-alpha and IL-1 beta synthesis. *J. Immunol. Baltim. Md 1950* **156**, 3455–3460 (1996).

171. Mäck, C., Jungermann, K., Götze, O. & Schieferdecker, H. L. Anaphylatoxin C5a Actions in Rat Liver: Synergistic Enhancement by C5a of Lipopolysaccharide-Dependent α2-Macroglobulin Gene Expression in Hepatocytes Via IL-6 Release from Kupffer Cells. *J. Immunol.* **167**, 3972–3979 (2001).

172. Gustafson, H. H., Holt-Casper, D., Grainger, D. W. & Ghandehari, H. Nanoparticle Uptake: The Phagocyte Problem. *Nano Today* **10**, 487–510 (2015).

173. Mebius, R. E. & Kraal, G. Structure and function of the spleen. *Nat. Rev. Immunol.* **5**, 606–616 (2005).

174. Elsabahy, M. & Wooley, K. L. Cytokines as biomarkers of nanoparticle immunotoxicity. *Chem. Soc. Rev.* **42**, 5552–5576 (2013).

175. Parkin, J. & Cohen, B. An overview of the immune system. *The Lancet* **357**, 1777–1789 (2001).

176. Opal, S. M., & DePalo, V. A. Anti-Inflammatory Cytokines. *Chest* **117**, 1162–1172 (2000).

177. Dinarello, C. A. Proinflammatory Cytokines. *CHEST* **118**, 503–508 (2000).

178. Seshadri, S., Kannan, Y., Mitra, S., Parker-Barnes, J. & Wewers, M. D. MAIL Regulates Human Monocyte IL-6 Production. *J. Immunol.* **183**, 5358–5368 (2009).

179. Tanaka, T., Narazaki, M. & Kishimoto, T. IL-6 in Inflammation, Immunity, and Disease. *Cold Spring Harb. Perspect. Biol.* **6**, (2014).

180. Wang, X. & Lin, Y. Tumor necrosis factor and cancer, buddies or foes? *Acta Pharmacol. Sin.* **29**, 1275–1288 (2008).

181. Couper, K. N., Blount, D. G. & Riley, E. M. IL-10: The Master Regulator of Immunity to Infection. *J. Immunol.* **180**, 5771–5777 (2008).

182. Brandtzaeg, P., Osnes, L., Øvstebø, R., Joø, G. B., Westvik, Å.-B., & Kierulf, P. Net inflammatory capacity of human septic shock plasma evaluated by a monocyte-based target cell assay: identification of interleukin-10 as a major functional deactivator of human monocytes. *J. Exp. Med.* **184**, 51–60 (1996).

183. Clarke, C. J. P., Hales, A., Hunt, A. & Foxwell, B. M. J. IL-10-mediated suppression of TNF-α production is independent of its ability to inhibit NFκB activity. *Eur. J. Immunol.* **28**, 1719–1726 (1998).

184. Luster, A. D. The role of chemokines in linking innate and adaptive immunity. *Curr. Opin. Immunol.* **14**, 129–135 (2002).

185. Matsukawa, A., Hogaboam, C. M., Lukacs, N. W. & Kunkel, S. L. Chemokines and innate immunity. *Rev. Immunogenet.* **2**, 339–358 (2000).

186. Charo, I. F. & Ransohoff, R. M. The Many Roles of Chemokines and Chemokine Receptors in Inflammation. *N. Engl. J. Med.* **354**, 610–621 (2006).

187. Nel, A., Xia, T., Mädler, L. & Li, N. Toxic Potential of Materials at the Nanolevel. *Science* **311**, 622–627 (2006).

188. Oldenborg, P.-A., Gresham, H. D. & Lindberg, F. P. Cd47-Signal Regulatory Protein α (Sirpα) Regulates Fcγ and Complement Receptor–Mediated Phagocytosis. *J. Exp. Med.* **193**, 855–862 (2001).

189. Burger, P., Hilarius-Stokman, P., Korte, D. de, Berg, T. K. van den & Bruggen, R. van. CD47 functions as a molecular switch for erythrocyte phagocytosis. *Blood* **119**, 5512–5521 (2012).

190. Abrams, M. T. *et al.* Evaluation of Efficacy, Biodistribution, and Inflammation for a Potent siRNA Nanoparticle: Effect of Dexamethasone Co-treatment. *Mol. Ther.* **18**, 171–180 (2010).

191. Luk, B. T. *et al.* Safe and Immunocompatible Nanocarriers Cloaked in RBC Membranes for Drug Delivery to Treat Solid Tumors. *Theranostics* **6**, 1004–1011 (2016).

192. Dobrovolskaia, M. A. & McNeil, S. E. Immunological properties of engineered nanomaterials. *Nat. Nanotechnol.* **2**, 469–478 (2007).

193. Nikolov, D. B., Xu, K. & Himanen, J. P. Homotypic receptor-receptor interactions regulating Eph signaling. *Cell Adhes. Migr.* **8**, 360–365 (2014).

194. Lisabeth, E. M., Falivelli, G. & Pasquale, E. B. Eph Receptor Signaling and Ephrins. *Cold Spring Harb. Perspect. Biol.* **5**, (2013).

195. Blits-Huizinga, C. T., Nelersa, C. M., Malhotra, A. & Liebl, D. J. Ephrins and their Receptors: Binding versus Biology. *IUBMB Life* **56**, 257–265 (2004).

196. Pasquale, E. B. The Eph family of receptors. *Curr. Opin. Cell Biol.* **9**, 608–615 (1997).

197. Eph Nomenclature Committee. Unified Nomenclature for Eph Family Receptors and Their Ligands, the Ephrins. *Cell* **90**, 403–404 (1997).

198. Frisén, J., Holmberg, J. & Barbacid, M. Ephrins and their Eph receptors: multitalented directors of embryonic development. *EMBO J.* **18**, 5159–5165 (1999).

199. Kullander, K. & Klein, R. Mechanisms and functions of eph and ephrin signalling. *Nat. Rev. Mol. Cell Biol.* **3**, 475 (2002).

200. Surawska, H., Ma, P. C. & Salgia, R. The role of ephrins and Eph receptors in cancer. *Cytokine Growth Factor Rev.* **15**, 419–433 (2004).

201. Edwards, C. M. & Mundy, G. R. Eph Receptors and Ephrin Signaling Pathways: A Role in Bone Homeostasis. *Int. J. Med. Sci.* **5**, 263–272 (2008).

202. Pasquale, E. B. Eph-Ephrin Bidirectional Signaling in Physiology and Disease. *Cell* **133**, 38–52 (2008).

203. Chen, Y., Fu, A. K. Y. & Ip, N. Y. Eph receptors at synapses: Implications in neurodegenerative diseases. *Cell. Signal.* **24**, 606–611 (2012).

204. Tan, W. *et al.* Coexistence of Eph receptor B1 and ephrin B2 in port-wine stain endothelial progenitor cells contributes to clinicopathological vasculature dilatation. *Br. J. Dermatol.* **177**, 1601-1611 (2017).

205. Riedl, S. J. & Pasquale, E. B. Targeting the Eph System with Peptides and Peptide Conjugates. *Curr. Drug Targets* **16**, 1031–1047 (2015).

206. Wang, Z. *et al.* Specific photothermal therapy to the tumors with high EphB4 receptor expression. *Biomaterials* **68**, 32–41 (2015).

207. Blevins, K. S., Jeong, J. H., Ou, M., Brumbach, J. H. & Kim, S. W. EphA2 targeting peptide tethered bioreducible poly(cystamine bisacrylamide–diamino hexane) for the delivery of therapeutic pCMV-RAE-1γ to pancreatic islets. *J. Controlled Release* **158**, 115–122 (2012).

208. Gobin, A. M., Moon, J. J. & West, J. L. EphrinAl-targeted nanoshells for photothermal ablation of prostate cancer cells. *Int. J. Nanomedicine* **3**, 351–358 (2008).

209. Obayemi, J. D. *et al.* Adhesion of ligand-conjugated biosynthesized magnetite nanoparticles to triple negative breast cancer cells. *J. Mech. Behav. Biomed. Mater.* **68**, 276–286 (2017).

210. Zhang, K. *et al.* Comprehensive optimization of a single-chain variable domain antibody fragment as a targeting ligand for a cytotoxic nanoparticle. *mAbs* **7**, 42–52 (2014).

211. Alkilany, A. M., Boulos, S. P., Lohse, S. E., Thompson, L. B. & Murphy, C. J. Homing Peptide-Conjugated Gold Nanorods: The Effect of Amino Acid Sequence Display on Nanorod Uptake and Cellular Proliferation. *Bioconjug. Chem.* **25**, 1162–1171 (2014).

212. Barquilla, A. & Pasquale, E. B. Eph Receptors and Ephrins: Therapeutic Opportunities. *Annu. Rev. Pharmacol. Toxicol.* **55**, 465–487 (2015).

213. Hu, C.-M. J. *et al.* Erythrocyte membrane-camouflaged polymeric nanoparticles as a biomimetic delivery platform. *Proc. Natl. Acad. Sci.* **108**, 10980–10985 (2011).

214. Guo, Y. *et al.* Erythrocyte Membrane-Enveloped Polymeric Nanoparticles as Nanovaccine for Induction of Antitumor Immunity against Melanoma. *ACS Nano* **9**, 6918–6933 (2015).

215. Li, R., He, Y., Zhang, S., Qin, J. & Wang, J. Cell membrane-based nanoparticles: a new biomimetic platform for tumor diagnosis and treatment. *Acta Pharm. Sin. B* **8**, 14–22 (2018).

216. Wan, X. *et al.* Red blood cell-derived nanovesicles for safe and efficient macrophage-targeted drug delivery in vivo. *Biomater. Sci.* **7**, 187-195 (2019).

217. Zhang, Q. *et al.* Neutrophil membrane-coated nanoparticles inhibit synovial inflammation and alleviate joint damage in inflammatory arthritis. *Nat. Nanotechnol.* **13**, 1182 (2018).

218. Li, J. *et al.* Cell Membrane Coated Semiconducting Polymer Nanoparticles for Enhanced Multimodal Cancer Phototheranostics. *ACS Nano* **12**, 8520–8530 (2018).

219. Bentley, A. A. & Adams, J. C. The evolution of thrombospondins and their ligand-binding activities. *Mol. Biol. Evol.* **27**, 2187–2197 (2010).

220. Oldenborg, P.-A. CD47: A Cell Surface Glycoprotein Which Regulates Multiple Functions of Hematopoietic Cells in Health and Disease. *ISRN Hematol.* **2013**, 614619 (2013).

221. Rodriguez, P. L. *et al.* Minimal "Self" Peptides That Inhibit Phagocytic Clearance and Enhance Delivery of Nanoparticles. *Science* **339**, 971–975 (2013).

222. Minelli, C. & Shard, A. G. Chemical measurements of polyethylene glycol shells on gold nanoparticles in the presence of aggregation. *Biointerphases* **11**, 04B306 (2016).

223. Burns, J. M., Saager, R., Majaron, B., Jia, W. & Anvari, B. Optical properties of biomimetic probes engineered from erythrocytes. *Nanotechnology* **28**, 035101 (2017).

224. Tang, J. C., Partono, A. & Anvari, B. Near-Infrared-Fluorescent Erythrocyte-Mimicking Particles: Physical and Optical Characteristics. *IEEE Trans. Biomed. Eng.* **66**, 1034-1044 (2018).

225. Noble, J. E. & Bailey, M. J. A. Chapter 8 Quantitation of Protein. in *Methods in Enzymology* (eds. Burgess, R. R. & Deutscher, M. P.) vol. 463 73–95 (Academic Press, 2009).

226. Baumgarth, N. & Roederer, M. A practical approach to multicolor flow cytometry for immunophenotyping. *J. Immunol. Methods* **243**, 77–97 (2000).

227. Bryant, D. A. Phycoerythrocyanin and Phycoerythrin: Properties and Occurrence in Cyanobacteria. *Microbiology* **128**, 835–844 (1982).

228. Behzadi, S. *et al.* Cellular uptake of nanoparticles: journey inside the cell. *Chem. Soc. Rev.* **46**, 4218–4244 (2017).

229. Chen, J. K. *et al.* An overview of clinical and experimental treatment modalities for port wine stains. *J. Am. Acad. Dermatol.* **67**, 289-304.e29 (2012).

230. Jacques, S. L. Optical properties of biological tissues: a review. *Phys. Med. Biol.* **58**, R37 (2013).

231. Kania, A. & Klein, R. Mechanisms of ephrin–Eph signalling in development, physiology and disease. *Nat. Rev. Mol. Cell Biol.* **17**, 240–256 (2016).

232. Lodola, A., Giorgio, C., Incerti, M., Zanotti, I. & Tognolini, M. Targeting Eph/ephrin system in cancer therapy. *Eur. J. Med. Chem.* **142**, 152–162 (2017).

233. Wang, S. *et al.* Novel Targeted System To Deliver Chemotherapeutic Drugs to EphA2-Expressing Cancer Cells. *J. Med. Chem.* **55**, 2427–2436 (2012).

234. Xiao, T. *et al.* Targeting EphA2 in cancer. *J. Hematol. Oncol.J Hematol Oncol* **13**, 114 (2020).

235. Mitra, S. *et al.* Structure-Activity Relationship Analysis of Peptides Targeting the EphA2 Receptor. *Biochemistry* **49**, 6687–6695 (2010).

236. Tandon, M., Vemula, S. V. & Mittal, S. K. Emerging strategies for EphA2 receptor targeting for cancer therapeutics. *Expert Opin. Ther. Targets* **15**, 31–51 (2011).

237. Jones, M. L. & Kurzban, G. P. Noncooperativity of Biotin Binding to Tetrameric Streptavidin. *Biochemistry* **34**, 11750–11756 (1995).

238. González, M. *et al.* Interaction of Biotin with Streptavidin: Thermostability and Conformational Changes Upon Binding. *J. Biol. Chem.* **272**, 11288–11294 (1997).